NANYANG TECHNOLOGICAL UNIVERSITY
SINGAPORE

EVOLUTION OF ROCK BRITTLENESS UNDER MECHANICAL AND THERMAL EFFECTS

WANG LU

SCHOOL OF CIVIL AND ENVIRONMENTAL ENGINEERING

2023

EVOLUTION OF ROCK BRITTLENESS UNDER MECHANICAL AND THERMAL EFFECTS

WANG LU

School of Civil and Environmental Engineering

A thesis submitted to the Nanyang Technological University
in partial fulfilment of the requirements for the degree of
Doctor of Philosophy

2023

Statement of Originality

I hereby certify that the work embodied in this thesis is the result of original research, is free of plagiarised materials, and has not been submitted for a higher degree to any other University or Institution.

25 Feb. 2023

Wang Lu

. . . . . .

Date

. . . . . .

WANG LU

Supervisor Declaration Statement

I have reviewed the content and presentation style of this thesis and declare it is free of plagiarism and of sufficient grammatical clarity to be examined. To the best of my knowledge, the research and writing are those of the candidate except as acknowledged in the Author Attribution Statement. I confirm that the investigations were conducted in accord with the ethics policies and integrity standards of Nanyang Technological University and that the research data are presented honestly and without prejudice.

25 Feb. 2023

. . . . . .

Date

. . . . . .

WU WEI

Authorship Attribution Statement

This thesis contains the material from three papers published/under review/in prep. in peer-reviewed journals in which I am listed as an author.

Chapter 4 is published as Wang, L., Wei, M., and Wu, W. (2022). Control of dynamic failure of brittle rock using expansive mortar. *Acta Geotechnica*, 1-11.

Prof Wu W. provided the project direction and edited the manuscript.

Dr Wei M. performed part of the simulation work and revised the manuscript.

I carried out the experiments, numerical simulations, data analysis, and drafted the manuscript.

Chapter 5 is published as Wang, L., and Wu, W. (2022). Modelling of dynamic tensile failure of inclusion-bearing rocks. *Geomechanics and Geophysics for Geo-Energy and Geo-Resources*, 8(5).

Prof Wu W. provided the project direction and edited the manuscript.

I carried out the numerical simulations, data analysis, and drafted the manuscript.

Chapters 6 is under review as Wang, L., Guo, K., and Wu, W. (2022). Abrasivity measurement of brittle rock after thermal treatment. *Measurement*.

Prof Wu W. provided the project direction and edited the manuscript.

Mr. Guo K revised figures in the manuscript.

I conducted the experiments, data analysis, and prepared the manuscript drafts.

25 Feb. 2023 Wang Lu

. . . .

Date WANG LU

ACKNOWLEDGEMENTS

I would thank Prof. Wu Wei for giving me the chance to pursue my doctorate and the financial support for my research work, and my gratitude to Prof. Zhao Zhiye for holding my hand in the darkest hour.

I would thank Prof Edwin for leaving the RM position for me even at the final year, I could thus enjoy the starry night on my way walking from office to hall.

I would thank my seniors Mei Cheng and Wei Mingdong for helping me addressing the research issues. I truly appreciate their help and cherish our friendship.

I would thank Mr. Heng Hiang Kim, Mr. Tan Hiap Guan, Mr. Choi Siew Pheng, and Mr. Cheng Weng Kong for their timely assistance in my research work and colorful life experience sharing.

Finally, I would thank my parents for teaching me to be serious about life, enjoy life, never show inferiority nor superiority, and most importantly, always be kind and grateful.

TABLE OF CONTENTS

ABSTRACT

Understanding rock brittleness plays an essential role in controlling the drilling and cutting efficiency in rock engineering for construction and energy applications. Numerous brittleness indices have been proposed to quantify rock brittleness under static and dynamic loads. However, rock brittleness under complex mechanical and thermal conditions has yet to be explicitly evaluated. In this thesis, a series of split Hopkinson pressure bar (SHPB) and Cerchar abrasivity index (CAI) tests are conducted experimentally and numerically to reveal the evolution of rock brittleness on rock materials under different mechanical and thermal conditions.

The expansion pressure from expansive mortar is an effective and efficient solution to promote the dynamic failure of brittle rock. The experimental and numerical results from the dynamic response of expansive mortar filled rocks reveal that the expansion pressure facilitates rock fracturing surrounding the expansive mortar, accompanied by the generation of tangential and radial cracks and the attenuation of the stress wave generated during the dynamic test. The data also show that the expansion pressure is larger than the radial inertia stress and dominates crack generation in unconfined rock. The change of nominal tensile strength with the strength ratio is consistent with the failure pattern of inclusion-bearing specimens, in which the inclusion part experiences the states of being pulverized, split, and intact. The changes of loading rate and temperature can affect the nominal tensile strength to a different degree with the increasing inclusion strength. The CAI tests show that the CAI value is mainly increased during the first few millimeters of scratching distance and is strongly influenced by the stylus indentation during the subsequent scratching distance. The stylus-rock interaction is examined based on the P-wave velocity and acoustic emission, and it is suggested to evaluate the wear flat by reconstructing the intact stylus profile and limiting the scratching distance.

This study implies that the rock behavior and failure pattern are inherently affected by the rock brittleness to varying degrees. The application of expansive mortar modifies the brittleness of surrounding rock under dynamic loading, resulting in changes in failure mode with more complex crack networks. For inclusion-bearing rocks, when the strength of the inclusion is comparable to or larger than that of its rock counterpart, the brittleness remains nearly constant with the increasing temperature. The brittleness is more sensitive to changes in loading rate and inclusion size than changes in temperature, especially in specimens with strong inclusion. The change in rock brittleness caused by thermal treatment essentially affects the stylus indentation. The CAI results show that a lower brittleness index corresponds to a higher CAI value and a reduced indentation stress.

LIST OF TABLES

LIST OF FIGURES

LIST OF SYMBOLS

Symbol	Definition
P	Peak force in BD test
2α	Loading angle in BD test
B	Thickness of BD disc
D	Diameter of BD disc
σ_t	Tensile strength
F_{nb}	Normal force in DEM
F_{sb}	Shear force in DEM
M_b	Bending moment in DEM
F_{nc}	Normal contact force in DEM
U_n	Normal displacement in DEM
K_n	Normal stiffness in DEM
K_s	Shear stiffness in DEM
E_c	Strain energy in DEM
E_b	Parallel-bond strain energy in DEM
E_k	Kinetic energy in DEM
E_f	Frictional slip energy in DEM
M_{ij}	Moment tensor
M_0	Scalar moment
M_w	Moment magnitude
σ_θ	Tangential stress
σ_γ	Radial stress
ε_θ	Tangential strain
ε_γ	Radial strain

P_e	Expansive pressure
σ_o	External pressure
σ_i	Internal pressure
E	Young's Modulus
ν	Poisson’s ratio
ε_i	Incident wave strain
ε_r	Reflected wave strain
ε_t	Transmitted wave strain
A	Cross-section area of the elastic bars
A_s	Cross-section area of the specimen
L_s	Length of the specimen
c_0	Wave velocity of elastic bar in SHPB test
$\dot{\varepsilon}_s$	Strain rate of the specimen in SHPB test
ε_s	Strain of the specimen in SHPB test
σ_s	Stress of the specimen in SHPB test
$\ddot{\varepsilon}_z(t)$	Axial strain acceleration in SHPB test
F_I	Contact force on incident specimen end in SHPB test
F_T	Contact force on transmitted specimen end in SHPB test
μ	Force equilibrium coefficient in SHPB test
G_f^I	Fracture energy for Model I fracture
σ_t^I	Tensile stress normal to the crack faces
u_n	Crack opening displacement
G	Shear modulus
e_{nn}^{ck}	Crack opening strain

Abbreviation	**Definition**

AE	Acoustic Emission
BI	Brittleness Index
BD	Brazilian Disc
DIC	Digital Image Correlation
DEM	Discrete Element Method
FBD	Flattened Brazilian Disc
FEM	Finite Element Method
PBM	Parallel Bond Method
PFC	Particle Flow Code
SEM	Scanning Electron Microscopy
SHPB	Split Hopkinson Pressure Bar

CHAPTER 1 INTRODUCTION

1.1 Background

To enhance the rock stability during underground excavation as well as the associated construction efficiency, numerous research has been implemented to modify the material properties and excavation techniques under complex geological conditions. Nevertheless, as the most employed rock fragmentation method, the drill-and-blast method is always accompanied by adverse environmental impacts such as ground vibration and rock outbreaks. The attempts to combat such issues including the current wave-screening method and isolation strategies may not be cost-effective (Park et al., 2009; Xia et al., 2014). Expansive mortar, as one of the artificial inclusion materials, is traditionally introduced as an alternative to explosives in concrete structure removal and surface rock breaking with minimum noise, dust, and vibration problems (Hinze and Brown, 1994; Laefer et al., 2010; Tang et al., 2017). The modification of expansive mortar aiming an accelerated pressurization rate and enhanced washout resistance enables its application in deep underground and inundated conditions (De Silva et al., 2017 and 2018b). Apart from the expansive mortar, inclusions are ubiquitous in rocks and created either naturally during rock formations (e.g., sand, clay, and gouge) or synthetically during engineering implementations (e.g., mortar, concrete, and grouts) (Liu et al., 2015; Kılıç et al., 2002; Wu et al., 2017; Sui et al., 2015). In rock engineering, inclusion materials have been extensively utilized in industrial applications such as underground mining support (Wang et al., 2021), in-situ leaching (De Silva et al., 2018b), and grouted rockbolts (Wu et al., 2019a). During the rock excavation, the instability induced from underground openings and fractured rock masses can be stabilized and eliminated by virtue of backfilling and grouting practices (Salimian et al., 2017; Liu et al., 2020; Helinski et al., 2007). Furthermore, the heterogeneity of inclusion-bearing rocks regarding the physical and mechanical differences in the two components may lead to a more complicated mechanical behavior. It is imperative therefore to evaluate the influence of inclusions on the stress state and cracking behavior of inclusion-bearing rocks. In addition to the study

on the role of inclusion materials in modifying the rock excavation performance, a further exploitation of the rock abrasivity that is closely related to the improved drilling technologies (e.g., combined thermo-mechanical drilling method) is of necessity.

Currently, the role of expansive mortar in the long-term and quasi-static conditions for surrounding rock fracturing has been widely investigated considering the influences of borehole number/size/spacing, water content, temperature, humidity, confinement conditions, etc. (Hinze and Nelson, 1996; Arshadnejad et al., 2011; Natanzi et al., 2016). Plenty of research has been done to reveal the mechanical properties and failure features of inclusion-bearing rocks and rock-like materials. Under quasi-static uniaxial compression, for instance, the concrete-encased coal pillar system represents a double-peaked stress-strain behavior (Zhang et al., 2020). The encased rock can strengthen the backfill, and the damage to the composite rock initiates from the central backfill (Wang et al., 2021). The cracking behaviors of gypsum specimens are related to the size, shape, stiffness, and strength of a single inclusion and additionally to the relative position of double inclusions (Janeiro et al., 2010). The dynamic failure of surrounding rock remains little known but important to provide a comprehensive understanding of rock failure associated with the existence of embedded inclusions under static and dynamic loads. When natural rock containing embedded inclusions (e.g., pressurized fluids in pore voids and compacted fillings in rock discontinuities) is subjected to dynamic loading, the embedded materials can modify the dynamic responses and the failure modes of surrounding rocks (Grgic et al., 2005; Huang et al., 2010; Li et al., 2014). The dynamic failure of the rock is also related to the sizes of inclusions and rock particles as well as loading rates (Zhou et al., 2021). Additionally, the rock and inclusion materials may have different mechanical responses to environmental temperature. The dynamic tensile failure of heated granite is strongly affected by thermal shock (Saksala and Ibrahimbegovic, 2020), and bolts and grouts also transfer heat to promote rock failure during tunnel fires (Wasantha et al., 2021).

Understanding the role of inclusions in the static and dynamic failure of surrounding rocks is essential for investigating the overall inclusion-bearing rock performances in rock engineering. But it is difficult to distinguish the role in rock failure based on field and laboratory experiments. Numerical simulations are commonly used to reveal the mechanism of the rock fracturing process, such as the finite element model (Tang, 1997; Dang et al., 2019; Yan and Jiao, 2020; Jia et al., 2021), the discrete element model (Duan et al., 2019a and 2019b; Li et al., 2020; Zhao et al., 2019), and the discontinuous deformation model (Jiao et al., 2012). The FEM-based Abaqus/Explicit software is considered as a simplified model with accurate and efficient analysis of crack initiation and propagation in rock materials (Li and Meng., 2013; Wei et al., 2016; Wu et al., 2020). This method is robust to reveal the rock failure mechanism with complex boundary conditions (Xu and Cai, 2017). In addition, the DEM model can explicitly solve the equations of particle motions instead of applying the complex constitute laws as adopted in the continuum method (Duan et al., 2019c). This method is able to capture the evolutionary fracture propagation with a detailed recording of the timely variation of particle micromechanics (Potyondy and Cundall, 2004; Schöpfer and Childs, 2013).

Since the drilling cost is a large share for the economic viability in the geo-energy extraction, the improvement of the rock cutting efficiency also presents a high priority (Rossi et al., 2020a). The estimation of the cutting-tool wear relies most on Cerchar abrasivity index (CAI) tests, and the determination of rock abrasivity is commonly based on the CAI value (Alber et al., 2014). As one of the characteristic rock properties, rock abrasivity is essential to evaluate the tool wear, energy consumption, and cutting duration in underground excavation (Zhang and Konietzky et al., 2020; Zhang et al., 2020a). Similarly, rock abrasivity is the function of temperature from multi-filed, including the geothermal condition, thermal assist operation, and varying temperature gradient with distance from the rock surface (Rossi et al., 2020b; Rathnaweera et al., 2018). Therefore, it is worthy to evaluate the rock abrasivity at extreme temperatures followed by different cooling treatments.

Brittleness is a characteristic of rock material properties (e.g., physical, mechanical, and geometrical) and rock behaviors under external conditions (e.g., stress state, temperature, and loading rate) contributing to or constraining the energy release during the rock failing (Meng et al., 2021; Tarasov and Potvin, 2012; Wasantha and Ranjith, 2014). It is strongly associated with rock cuttability and drillability during underground excavation and is also an important indicator of rockburst proneness in deep mining and tunneling (Meng et al., 2015). Brittle rocks are more prone to be bored, resulting in a less energy consumption and a higher drilling efficiency (Peng at al., 2016b). The geohazards during underground excavation such as rockburst and rib spalling are commonly observed in brittle rocks under high geo-stresses (Wang and Park, 2001), while the creep and squeezing deformations which are more moderate compared to the rockburst that often occurs in ductile rocks (Singh, 1986). Brittle shale rocks are favourable in hydraulic fracturing due to the enlarged artificial crack volume and displacement (Guo et al., 2015b). However, previous studies on rock brittleness focus on the quasi-static regime in respect of intact rock mechanical properties or loading conditions, and there is still a knowledge gap in dynamic rock brittleness responses of rocks containing inclusions. Besides, this study also aims to assist in improving the understanding of brittleness evolution for intact rocks and inclusion-bearing rocks subjected to elevated temperatures.

1.2 Research objective and scopes

This research aims to investigate the mechanical properties and failure mechanisms of intact rocks and inclusion-bearing rocks subjected to combined mechanical and thermal conditions. The research scopes are summarized as below:

(1) To experimentally and numerically study the dynamic responses of expansive mortar filled rocks.

(2) To numerically interpret the dynamic tensile failure of inclusion-bearing rocks under different combinations of temperatures and loading rates.
(3) To experimentally explore the rock abrasivity at high temperatures followed by cooling treatments

1.3 Organization of the thesis

This thesis consists of seven chapters (Figure 1-1). First, chapter 1 introduces the application of inclusion-bearing rocks in stabilizing and enhancing underground rock excavation, and the cutability of rocks under complex drilling conditions. Then, chapter 2 presents a comprehensive literature review, containing concepts of brittleness, FBD method, DEM model, SHPB test and thermal effect on rock behaviors. Next, chapter 3 elaborates on the numerical and experimental methodologies. Chapter 4 evaluates the control of dynamic failure of rocks using expansive mortar. Chapter 5 simulates the dynamic tensile performance of inclusion-bearing rocks. And finally, chapter 6 discovers abrasivity measurement of rocks after thermal and cooling treatments. All the findings in the current works are concluded in chapter 7 along with proposals for the future research plan.

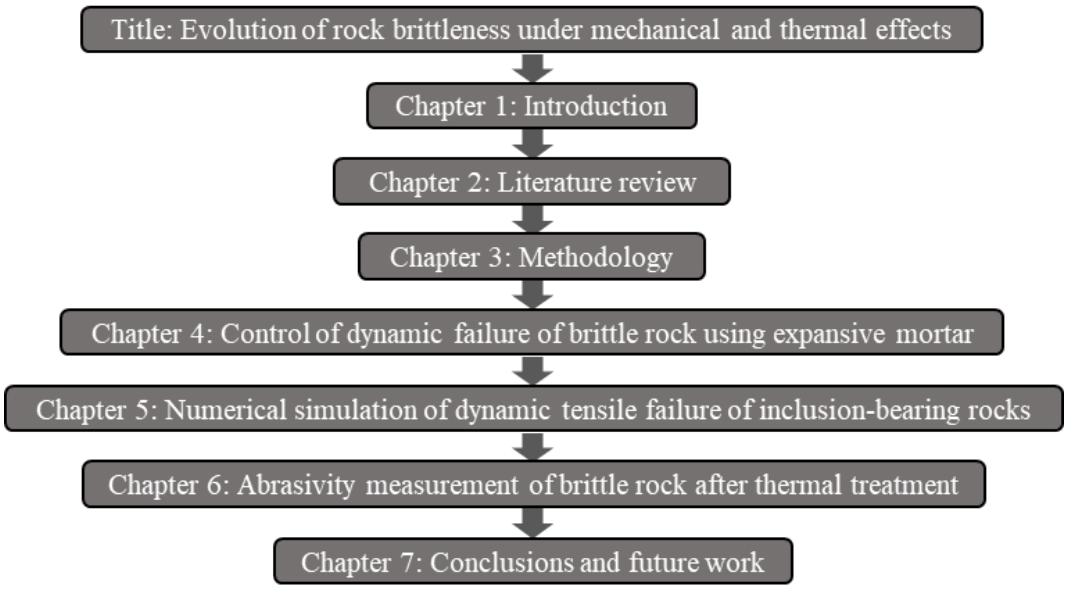

Figure 1-1 Flowchart of the thesis organization.

CHAPTER 2 LITERATURE REVIEW

This chapter reviews the theoretical, experimental, and numerical methods used in this thesis, including the concept of brittleness, thermal and mechanical effects on rocks and the related laboratory (e.g., SHPB, BD, and CAI) and numerical (e.g., FEM, DEM) testing methods, as well as the material (e.g., expansive mortar).

2.1 Brittleness

2.1.1 Briefing of brittleness

Brittleness is one of the most important mechanical properties of rocks that can strongly influence the rock failure process in various rock engineering fields. To date, numerous methods have been proposed to determine the brittleness experimentally through either uniaxial or triaxial compression tests (Hucka and Das, 1974; Gong and Zhao, 2007; Jarvie et al., 2007; Meng et al., 2021). However, the concept of brittleness has yet been precisely defined, and there is no consensus on the standard for brittleness measurement. Difficulties in reaching an agreement can be that there exist two alternative failure mechanisms including tensile and shear failures (Tarasov and Potvin, 2012). Additionally, on one hand, rock brittleness is an intrinsic material property that indicates the composition and structure of different rocks. On the other hand, external variables such as loading condition and temperature can affect the rock behavior, which modifies the brittleness assessment consequently. The common approaches to evaluate brittleness relies on the determination of the physical and mechanical characteristics of rocks, such as mineral composition, strength parameters, elastic parameters, and pre-and post-peak energy balance obtained from a complete stress-strain curve (Guo et al., 2015; Hajiabdolmajid and Kaiser, 2003). Due to the presence of theoretical differences in various methodologies, the brittleness results may turn out to be contradictory. Therefore, the reliability of each brittleness index depends on the adoption of an appropriate method for a particular purpose.

2.1.2 Brittleness indices based on strength parameters

The ratio of uniaxial compressive strength (σ_c) and Brazilian tensile strength (σ_t) is widely used to represent the brittleness of rocks due to their simple form (e.g., B_1 to B_4). In addition, as the primary mechanical properties, σ_c and σ_t can be easily obtained via the compression tests when other data were unavailable. The indices B_1 to B_4 are generally used to investigate the relationships between rock brittleness and rock drillability and rockburst possibility in projects of rock excavation. It shows that a higher B_1 or B_2 value indicates a more brittle rock, and more energy is required to drill a rock with larger a B_3 or B_4 (Singh, 1986; Kahraman, 2002; Altindag, 2002). However, the use of B_1 value may lead to a contradictory result. For example, the B_1 value is negatively correlated with the rock boreability index, indicating that a higher rock brittleness can benefit the rock-breaking efficiency (Gong and Zhao, 2007; Zhao et al., 2007). While the other researchers report an opposite result that the energy consumption for excavation increases with the increasing B_1 value (Kahraman, 2002; Mohammadi et al., 2015) The trend of B_1 to B_4 mainly reflects the change of rock strength instead of brittleness. The two strength parameters are unable to fully demonstrate the rock failure process (Meng et al., 2015). Besides, the external stress condition can highly affect the brittleness, for instance, the ductility of rocks increases with increasing confining pressure (Wasantha and Ranjith, 2014). Therefore, it is not appropriate to assess the rock brittleness purely based on the strength parameters when rocks are subjected to a complex stress state.

$$B_1 = \sigma_c / \sigma_t \tag{2-1}$$

$$B_2 = (\sigma_c - \sigma_t)/(\sigma_c + \sigma_t) \tag{2-2}$$

$$B_3 = \sigma_c \sigma_t / 2 \tag{2-3}$$

$$B_4 = \sqrt{\sigma_c \sigma_t / 2} \tag{2-4}$$

2.1.3 Brittleness indices based on elastic parameters

The mutual effect of Young's modulus (E) and Poisson's ratio (ν) on the rock brittleness can be used to identify the efficiency in exploiting the shale oil and gas resources. Rocks with a greater Young's modulus and a smaller Poisson's ratio favor the brittle failure (Rickman et al., 2014; Jahandideh and Jafarpour, 2016), resulting in the generation of a more complex fracture network in the shale formation (B_5). By introducing Lame constant (λ), the ratio of elastic modulus to the Lame constant (B_6) can represent brittleness as well, and the B_6 index is ultimately found to negatively correlate with Poisson's ratio (Chen et al., 2014). However, the other researcher observes an opposite conclusion that Young's modulus is positively associated with Poisson's ratio. According to Roylance (2001), more hydraulic pressure is needed to fracture the rock with a higher Young's modulus. Overall, it is suggested that the brittleness index applied in one shale formation may not be applicable to other reservoirs.

$$B_5 = \frac{1}{2}\left(\frac{E - E_{\min}}{E_{\max} - E_{\min}} + \frac{\nu_{\max} - \nu}{\nu_{\max} - \nu_{\min}} \right) \tag{2-5}$$

where E_{max} and E_{min} are the maximum and minimum Young's modulus, respectively, and ν_{max} and ν_{min} are the maximum and minimum Poisson's ratio, respectively.

$$B_6 = E/\lambda = E/\left[E\nu/(1+\nu)(1-2\nu)\right] = \frac{1}{\nu} - 1 - 2\nu \tag{2-6}$$

2.1.4 Brittleness indices based on mineral compositions

The brittleness defined according to mineralogy is commonly adopted in selecting the potential fracture candidates in shale reservoirs. It is assumed that a higher content of brittle minerals contributed to a more brittle rock. The techniques such as logging tools

and X-ray diffraction tests facilitate the identification of mineral composition in rocks. The index B_7 is developed as a function of the amounts of brittle minerals (e.g., quartz) and ductile minerals (e.g., carbonate and clay). However, this index neglects the fact that the rocks undergoing different diagenesis and environmental conditions can significantly impact the brittleness even if they have similar mineral compositions. Rock tenacity rating index (B_8) is another brittleness index that considers various influencing parameters such as stiffness, grain size, and foliation for each mineral, whereas the analyses of each rating factor are rather complicated.

$$B_7 = \frac{W_{qtz}}{W_{qtz} + W_{carb} + W_{clay}} \tag{2-7}$$

where W_{qtz}, W_{carb}, and W_{clay} are the weights of quartz, carbonate, and clay minerals, respectively.

$$B_8 = S_F G_F F_F \tag{2-8}$$

where S_F, G_F, and F_F are the stiffness, texture, and foliation rating factors, respectively.

2.1.5 Brittleness indices based on stress-strain curves

The rock properties and failure behaviors can be intuitively reflected by the shape of stress-strain curves during the loading and failure processes. Apart from the stress-based, strain-based, and modulus-based indices, the investigation of energy consumption and dissipation in the rock failure offers another approach to estimate the rock brittleness by quantifying the energy balance at pre- and post-peak stages (Wawersik and Fairhurst, 1970; Zhang et al., 2016; Wang and Wu, 2022). According to Tarasov and Potvin (2013), brittleness represents the rocks' self-sustaining capacity to resist the post-peak instability aroused from the release of energy accumulated inside the rock during the loading period. It shows that the whole brittleness scale from absolute brittleness to ductility can be properly explained by only two criteria (i.e., B_9 and B_{10}) as shown in Figure 2-1, which

also allows for the demonstration of Class I and Class II rock behaviors. The indices B_9 and B_{10} are derived based on the relationships among elastic (dW_e), rupture (dW_r), and additional (dW_a) energies:

$$B_9 = \frac{dW_r}{dW_e} = \frac{M - E}{M} \tag{2-9}$$

$$B_{10} = \frac{dW_a}{dW_e} = \frac{E}{M} \tag{2-10}$$

where E and M are the elastic and post-peak moduli, respectively. Class II failure occurs when the condition $B_9<1$ or $B_{10}>0$ is met, at which the failure is self-sustained, otherwise, Class I mode is observed with unspontaneous failure.

Recently, other indicators such as AE, rock damage, and post-peak behavior are proposed to evaluate the rock brittleness. It shows that the monitoring of AE development during the triaxial compression can accurately distinguish the failure of weak-brittle rock, especially the occurrence of transition stage as confining pressure increases (Shi et al., 2021). A brittleness index established from the rock damage curve exhibited a more reliable and consistent evaluation for the rock under different test conditions (Wang et al., 2022). Two new brittleness indices named brittleness degree and brittleness failure intensity can work jointly to estimate the efficiency in preventing and controlling the rockburst disaster (Meng et al., 2015). The confining stress at the brittle-ductile transition of rocks is predicted by a conceptual framework to serve as an alternative brittleness index (Walton 2021). A super stiff rock mechanics testing machine was developed to capture the complete post-peak deformation for brittle hard rock that is normally failed in a Class II type (Cai et al., 2021).

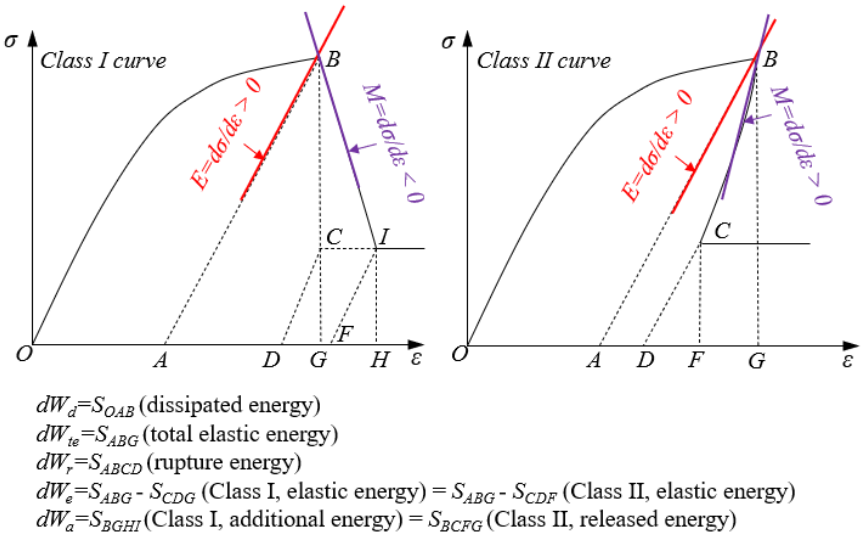

(a)

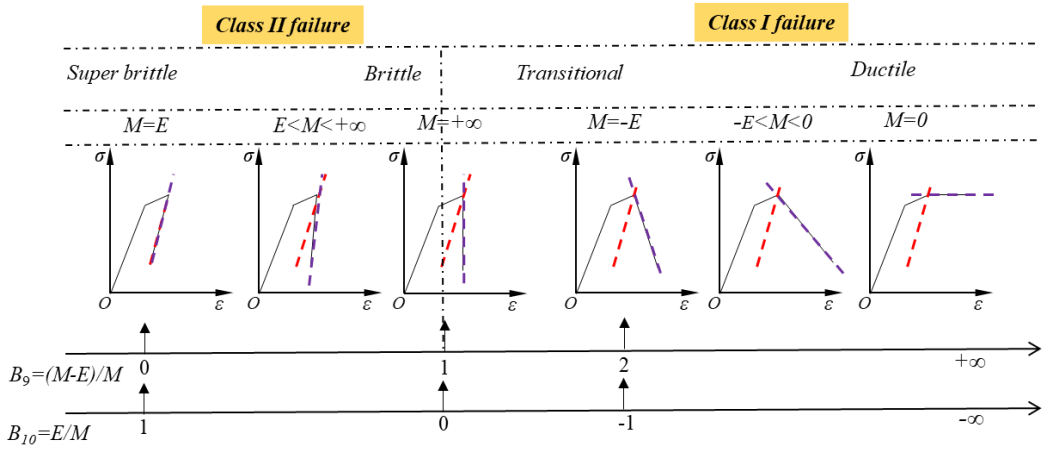

(b)

Figure 2-1 Schematics for Class I and Class II failures on stress–strain curves, (a) post-peak energy balance (modified from Meng et al. (2021)), and (b) scales of brittleness B_9 and B_{10} (modified from Tarasov and Potvin (2013)).

2.2 Thermal effect on rock behaviors

The pressing demands for land usage and energy extraction greatly promote the exploration of underground projects. The rocks in deep geotechnical engineering such as radioactive waste repositories, enhanced geothermal system, and underground coal gasification are generally exposed to high-temperature contexts to a hundred degrees Celsius (Roy and Singh, 2016; Hokmark and Claesson, 2005; Kempka et al., 2011). In addition, the accident outbreak of fire in the underground mining or tunneling can result in catastrophic hazards for those rock structures (Sha et al., 2019). Therefore, the understanding of rock behaviors at an elevated temperature is vital to the successful implementation of rock projects at depth.

Many contributions to the literature concern the mechanical properties of rocks based on laboratory experiments. It is found that the elastic modulus, compressive strength, tensile strength, and fracture toughness are generally correlated negatively with the increasing temperature (Hu et al., 2018). Nonetheless, the evolution of these parameters also shows a fluctuation below a threshold temperature. For instance, the strength may remain constant or tend to drop with temperature in the first 400 °C and turn to increase from that onwards. The change in the strength is due to the corresponding competition between the extent of dehydration and mineral expansion. Below 400 °C, the loss of moisture from the escaped absorption and crystal water destroys the rocks with micro voids and micro defects, resulting in a decrease in rock strength because of the increased rock porosity (Zhang et al., 2016). In contrast, the thermal compression provided by the mineral expansion leads to the closure of pre-existing microcracks, which enhances the rock property to a certain degree (Huang et al., 2016). Overall, it is concluded that the intrinsic properties of the rock (e.g., pore structure grain composition and cementation type) govern its mechanical responses to the temperature change. Particularly, for granites with relatively compacted structure compared to that of sandstones, the strength of which mainly exhibits a monotonical reduction with the increasing temperature since there is a limited buffer space inside the rock for mineral ductile deformation (Sha et al., 2020). When the treatment temperature exceeds 400 °C, the strengths of granite and

sandstone tend to reduce with the temperature as the anisotropic thermal expansion dominates. Additionally, the transition of quartz from α to β phase at 573 °C significantly promotes its volume expansion, which implies a server damage to the whole rock structure (Krancz, 1983).

Apart from the study of macro-mechanical rock behaviors, the auxiliary options including scanning electron microscopy (SEM), optical microscopy (Figure 2-2), acoustic emission (AE), and fluorescent dye impregnation technique can assist in the observation of thermal cracking process microscopically. Based on the SEM observation, the intergranular microcracks are observed to initiate along the boundary of the grains during the period with relatively low temperature (e.g., below 400 °C), and a further increase of the thermal loading induces the formation of the intragranular microcracks that developed within the grains (Zuo et al., 2010). The phase change of quartz is associated with an intensive acquisition of AE activities (Glover et al., 1995). The topographic characteristics of microcracks in respect of length and orientation at the specimen surface are clearly illustrated by the impregnated fluorescent dye (Li et al., 2020). However, the methods mentioned above focus on the local features within a small area, the numerical simulation provides an alternative to visualize the full-filed rock behaviors under coupled thermal-mechanical effect. The DEM has been widely used to evaluate the mechanical property and failure mechanism of various rocks under different test conditions. For example, the dynamic fracture toughness of granite decreases with the increasing temperature in the range of 25 - 400 °C on the premise that the loading rate is higher than 130 GPa $m^{0.5}$/s, and the effect of temperature is negligible when the loading rate ranges from 80-130 GPa $m^{0.5}$/s (Yin et al., 2018). The macrocracks induced from the thermal gradient initiate first in a relatively cool region and propagate gradually to a warmer area (Zhao, 2015). When the temperature rises from 53 °C to 65 °C, the failure mode of rock salt changes from large fragments to small-crushed pieces under the triaxial compression test (Li et al., 2018). The thermally induced cracks provoke an increased creep strain rate with the increasing temperature, which contributes to the

understanding of rock salt creep behaviors in underground gas storage application (Li et al., 2017).

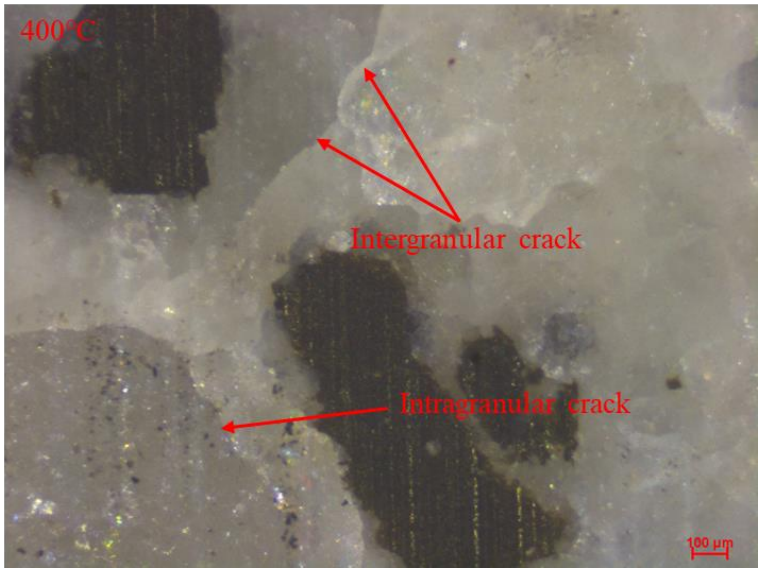

Figure 2-2 Optical microscopic observations of mineral morphology after thermal treatment at 400 °C.

2.3 Split Hopkinson pressure bar method

2.3.1 Historical background and application

John Hopkinson, the pioneer of the Hopkinson bar technique, invented it to measure the material response to the loading effect in 1872. By further studying the technique in 1914, Bertram Hopkinson (1914) improved the system to be able to measure the stress-time relationship during the dynamic loading in a long steel rod. Based on the previous work, Kolsky (1949) came up with the idea of the split bar by adding a second pressure bar to the original design. The specimen is sandwiched in between the bars, and the corresponding strains are measured by using the similar condensers technique introduced by Davies (1948). The strain histories collected from both end surfaces of the specimen

enables the derivation of the specimen stress, strain, and strain rate. Hauser and Simmons (1961) significantly improved the data accuracy by initially adopting the strain gauges in their tests. Harding (1965) and Duffy et al. (1971) extended the split Hopkinson bar technique to tension and torsion experiments in addition to the compression test. With the assistance of computing power as well as the application of the digital oscilloscope and signal analysers, researchers now can obtain more reliable and precise data.

Regarding the complex in-situ geological conditions, the temperature factor that could essentially affect the rock behaviours is of necessity to be considered in evaluating the dynamic response of materials. Deep underground excavation and mining induced explosion may associate with the effect of high temperature. Generally, there are two methods to investigate the heating effect, one is to conduct the test in the post-heated state (Peng et al., 2016a and 2016b; Clark et al., 1981), and another is to proceed in the heating state (Li and Bai, 2012; Chen et al., 2015; Liu and Xu, 2013; Wong et al., 2017). In applications of aeronautical and aerospace where materials might be subjected to the low temperature, Wang and Jiang. (2012) and Gomez-del Rio et al. (2005) manufactured the similar cooling chambers (i.e., liquid nitrogen based) to evaluate the dynamic performances of fibre reinforced composites and aluminium alloys under -60 °C and -150 °C, respectively. Ma et al. (2017) investigated the dynamic properties of frozen soil under the coupled effects of freezing temperature and confining pressure. The failure mode of the rock specimen under dynamic compression is a typical splitting. The specimens are fragmented into pieces of different sizes according to the magnitude of pulse stress (Xia and Yao, 2015; Wong et al., 2017; Bauer et al., 2019). Besides the uniaxial compression, Li et al. (2008) modified the SHPB apparatus to investigate the mechanical properties of rocks subjected to the coupled static and dynamic loads. They found that a higher coupling load could result in a violent rock fragmentation. Adopted as one of the indirect measurements of dynamic tension, the Brazilian Disc (BD) test can avoid bending and pre-mature failure issues occurring in direct tension approaches. Moreover, the dynamic BD method enables an easier operation and is thus more effective.

Tensile and shear failures are the main failure modes generally observed in the BD specimens. The tensile cracks initiate from the centre of the disc and propagate parallelly along the impact direction, featuring a diametrical splitting. The localized shear failure zones emerge near the specimen-bar interfaces (Zhou et al., 2014). The influence of excavation-induced radial stress gradient on dynamic compressive and tensile properties of hollow discs are widely investigated recently. Wang et al. (2019) analysed the failure pattern of hollow sandstone discs under various external confining pressures with cyclical impacts. The radial gradient stress results in the generation of a circumferential crack on the middle ring of the rock surface and several localized shear failures. Most of the hollow discs fragment into four parts under dynamic BD tests (Li et al., 2016).

2.3.2 One-dimensional wave theory analysis

The implementation of the SHPB technique is based on the one-dimensional theory of longitudinal wave propagation along a thin and elastic bar. The basic assumptions to apply this principle are (Kolsky, 1963):

(i) The bars remain linear elastic through the whole test, which allows the repeatedly measuring of the strains in the incident and transmitted bars as well as the accurate estimation of the dynamic response of the specimen.

(ii) The dispersion effect in the bars is negligibly small during the propagation of the stress wave. The uniformly distributed pulse over the bar cross-sections enables the records of the strain-gauges that represent the strains at the bar-specimen interfaces.

(iii) The effects of radial inertia and end surface friction are minimal. The stress and strain fields in the specimen are uniform along the axial direction.

A differential element dx extracted from an elastic rod which has been enforced a stress pulse on its longitudinal direction is taken for the study of the one-dimensional wave propagation. Figure 2-3 shows the force balance across the differential element with the cross-section area A, density ρ, and elastic modulus of E. By using the Hook's law, the compressive force F_1 and F_2 can be written in terms of displacement u:

$$F_1 = -A \cdot \sigma = -A \cdot E \cdot \frac{\partial u}{\partial x} \tag{2-11}$$

$$F_2 = -A \cdot \left(\sigma + \frac{\partial \sigma}{\partial x} \cdot dx \right) = -A \cdot E \cdot \frac{\partial u}{\partial x} - A \cdot E \cdot \frac{\partial^2 u}{\partial x^2} \cdot dx \tag{2-12}$$

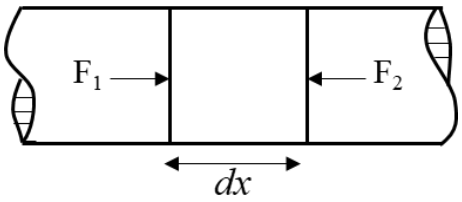

Figure 2-3 A differential element subject to compressive stress wave.

Additional force acting on the element is expressed from Newton's second law of motion:

$$F = m \cdot a = \rho \cdot A \cdot dx \cdot \frac{\partial^2 u}{\partial t^2} \tag{2-13}$$

$$F_1 - F_2 = -A \cdot E \cdot \frac{\partial u}{\partial x} - (-A \cdot E \cdot \frac{\partial u}{\partial x} - A \cdot E \cdot \frac{\partial^2 u}{\partial x^2} \cdot dx) = F = \rho \cdot A \cdot dx \cdot \frac{\partial^2 u}{\partial t^2} \tag{2-14}$$

and simplified as:

$$\frac{E}{\rho} \cdot \frac{\partial^2 u}{\partial x^2} = \frac{\partial^2 u}{\partial t^2} \tag{2-15}$$

Equation (2-15) as the equation of motion describes the elastic wave propagation in the longitudinal direction and can be re-written as:

$$c_0^{\,2} \cdot \frac{\partial^2 u}{\partial x^2} = \frac{\partial^2 u}{\partial t^2} \tag{2-16}$$

where c_0 is the wave velocity travelling in the medium of bar.

The general solution of the above motion equation is:

$$u = f\left(x - c_0 \cdot t\right) + g\left(x + c_0 \cdot t\right) \tag{2-17}$$

where f and g are arbitrary functions, which representing the propagation of the waves either in the positive or the negative directions. Differentiating the solution of displacement with respect to position x and time t, the strain ε, stress σ and particle velocity v are given by:

$$\varepsilon = \frac{\partial u}{\partial x} = f' + g' \tag{2-18}$$

$$\sigma = E \cdot \left(f' + g'\right) \tag{2-19}$$

$$v = \frac{\partial u}{\partial t} = c_0 \cdot \left(-f' + g'\right) \tag{2-20}$$

2.3.3 Derivation of the specimen stress, strain, and stain rate

Figure 2-4 shows the interaction of the stress waves at the bar-specimen interfaces, the particle velocities, and forces:

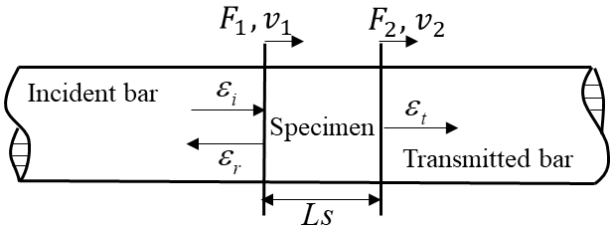

Figure 2-4 Stress wave propagation along bars and specimen.

Particle velocities at the incident bar-specimen and the specimen-transmitted-bar interfaces are:

$$v_1 = \frac{\partial u_1}{\partial t} = c_0 \cdot \left(-\varepsilon_i + \varepsilon_r\right) \tag{2-21}$$

$$v_2 = \frac{\partial u_2}{\partial t} = -c_0 \cdot \varepsilon_t \tag{2-22}$$

$$\dot{\varepsilon}_s = \frac{v_2 - v_1}{L_s} = \frac{-c_0 \cdot \varepsilon_t - c_0 \cdot \left(-\varepsilon_i + \varepsilon_r\right)}{L_s} = \frac{c_0}{L_s} \cdot \left(\varepsilon_i - \varepsilon_r - \varepsilon_t\right) \tag{2-23}$$

where L_s is the length of the specimen.

By integrating Equation (2-23), one can obtain the strain history of the specimen:

$$\varepsilon_s = \int \dot{\varepsilon}_s dt = \frac{c_0}{L_s} \cdot \int_0^t \cdot \left(\varepsilon_i - \varepsilon_r - \varepsilon_t\right) dt \tag{2-24}$$

When the dynamic equilibrium is achieved, the forces F_{1s} and F_{2s} applied at the two sides of specimen are equal with each other and the average force is revealed as:

$$F_{1s} = A \cdot E \cdot \left(\varepsilon_i + \varepsilon_r\right) \tag{2-25}$$

$$F_{2s} = A \cdot E \cdot \varepsilon_t \tag{2-26}$$

$$F_s = \frac{F_{1s} + F_{2s}}{2} = \frac{A \cdot E}{2} \cdot \left(\varepsilon_i + \varepsilon_r + \varepsilon_t \right) \tag{2-27}$$

The average stress in the specimen then simply follows as:

$$\sigma_s = \frac{F_s}{A_s} = \frac{A \cdot E}{2 \cdot A_s} \cdot \left(\varepsilon_i + \varepsilon_r + \varepsilon_t \right) \tag{2-28}$$

where A_s is the cross-section area of the specimen.

Finally, the calculation of stress, strain and strain rate of a specimen subjected to the dynamic loading through SHPB test is summarized as:

$$\begin{cases} \sigma_s = \dfrac{F_s}{A_s} = \dfrac{A \cdot E}{2 \cdot A_s} \cdot \left(\varepsilon_i + \varepsilon_r + \varepsilon_t \right) \\ \varepsilon_s = \int \dot{\varepsilon}_s dt = \dfrac{c_0}{L_s} \cdot \int_0^t \cdot \left(\varepsilon_i - \varepsilon_r - \varepsilon_t \right) dt \\ \dot{\varepsilon}_s = \dfrac{c_0}{L_s} \cdot \left(\varepsilon_i - \varepsilon_r - \varepsilon_t \right) \end{cases} \tag{2-29}$$

2.3.4 Wave dispersion and pulse shaping technique

So far, the dynamic stress, strain, and strain rate on the specimen are derived from the strains recorded at bar-specimen interfaces. Such measurement requires that the propagation of the pulse is uniform over the cross-section of the bar without any shape change. However, the inherent dispersion effect results in a three-dimensional elastic wave propagation fact instead of the one-dimensional analysis. Pochhammer–Chree equation is established to depict the relationships between the wave propagation velocity, Poisson's ratio, and the ratio of bar diameter to the wavelength of harmonic wave (Ilyashenko and Kuznetsov, 2018). Davies (1948) derived the dispersion of the wave travelling along the bar by solving the Pochhammer-Chree equation for the first three vibration modes. Essentially, the superimposed waves with different wavelengths and

amplitudes induce the pulse oscillations. The short pulse travels slowly along the bar with sharper rise time can result in even a greater dispersion because of the increased frequency and widened range. Hence, the reading recorded from the strain gauges mounted on the mid-span of the bars must be modified before being applied to the dynamic mechanical property calculation of the specimen. Alternatively, many efforts have been made to minimize the dispersion effect via the pulse shaping technique, e.g., increasing the rising time by modifying the striker shape (Christensen et al., 1972, Li et al., 2000), using a low pass filter (Verleysen et al., 2008), inserting a deformable pulse shaper in between the striker and the incident bar (Chen, 1999; Ramírez and Rubio-Gonzalez, 2006; Frew et al., 2001 and 2002).

2.4 Cerchar abrasivity index test

With the development of the Cerchar test, the understanding of the relations between CAI and scratching parameters as well as rock properties has been remarkably improved. The CAI value is strongly affected by the rock mineralogy (Yaralı et al., 2008) and internal structure (Alber, 2008) but independent of scratching speed (Rostami et al., 2014). The CAI value is also correlated to the compressive and shear strengths of corresponding rocks (Deliormanlı, 2012; Er and Tuğrul, 2016). The rock-stylus interaction is estimated based on the rock removal volume and the stylus wear volume (Zhang and Konietzky, 2020), and the efficiency of rock scratching is reflected by the stretching specific energy (Zhang et al., 2020a and 2020b). Machine learning approaches can be additionally applied to predict the CAI value according to the rock's mechanical properties, such as P-wave velocity, uniaxial compressive strength, and Young's modulus (Tripathy et al., 2015). As suggested by the test standard of the International Society for Rock Mechanics and Rock Engineering (ISRM) (Alber et al., 2014), the CAI measurement relies on the profile of the worn stylus, which should be relatively flat and symmetrical about the longitudinal axis of the stylus, without serious damage on the sides of the stylus cone. However, the thermal treatment may promote the indentation of the stylus into highly cracked rock. In other words, the amplified interaction between the

worn stylus and the cracked rock possibly causes the side wear and subsequently modifies the profile of wear flat. In this case, the direct measurement of the worn stylus may not be reasonable to represent the rock abrasivity. The contribution of the side wear, which can be even more significant after rapid cooling, should be excluded from the CAI measurement. Therefore, the CAI measurement for the case with notable stylus indentation should be re-examined and improved to ensure the measurement following the requirement of the ISRM test standard.

2.5 Brazilian disc (BD) method

2.5.1 Briefing of BD method

There are two types of methods suggested by ISRM (International Society for Rock Mechanics) and ASTM (American Society for Testing and Materials) to assess the quasi-static tensile strength of rock-like materials, including the direct tension and indirect tension tests (ISRM, 1978; ASTM, 2008a and 2008b). Compared to the direct tension method which has difficulties in operating tests and guaranteeing the data precision, the indirect tension method such as the Brazilian disc (BD) performs more robustly and is widely adopted (Coviello et al., 2005; Zhang and Zhao, 2014). The BD test is initially applied in the static test by diametrically compressing the circular disc to failure. Hondros (1959) solved the complete stress solution for the principal stresses σ_θ and σ_γ in a BD test (Figure 2-5e):

$$\sigma_\theta = +\frac{2P}{\pi DB\alpha}\left\{\frac{\left[1-(rr/R)^2\right]\sin 2\alpha}{1-2(r\,r/R)^2\cos 2\alpha+(rr/R)^4}-\tan^{-1}\left[\frac{1+(rr/R)^2}{1-(rr/R)^2}\tan\alpha\right]\right\}$$
$$\sigma_\gamma = -\frac{2P}{\pi DB\alpha}\left\{\frac{\left[1-(rr/R)^2\right]\sin 2\alpha}{1-2(rr/R)^2\cos 2\alpha+(rr/R)^4}+\tan^{-1}\left[\frac{1+(rr/R)^2}{1-(r\,r/R)^2}\tan\alpha\right]\right\} \quad (2\text{-}30)$$

where P is the peak force during the entire loading history, 2α is the loading angle, rr is the distance from the disc center, and B and D are the thickness and diameter of the disc, respectively. Tensile stress is deemed as positive.

According to the fracture criterion raised by Griffith (1924), the fracture must initiate exactly at the center of the disc, the principal stresses are then expressed as:

$$\begin{aligned}\sigma_\theta &= +\frac{2P}{\pi DB}\left\{\frac{\sin 2\alpha}{\alpha}-1\right\} \approx +\frac{2P}{\pi DB}\\ \sigma_\gamma &= -\frac{2P}{\pi DB}\left\{\frac{\sin 2\alpha}{\alpha}+1\right\} \approx -\frac{6P}{\pi DB}\end{aligned} \tag{2-31}$$

There are several postulates to guarantee a valid BD test, i.e., the central fracture initiation, negligible intermediate principal stress (Fairhurst, 1964), and the homogeneous/isotropic testing material (Mellor and Hawkes, 1971). However, the premature damage found in the disc ends due to inappropriate machine-specimen contact may violate the principle in BD tests.

2.5.2 Briefing of Flattened BD (FBD) method

To overcome such limitations, many solutions are proposed to modify either the experimental setup or the specimen fabrication (Li and Wong., 2013). As for apparatus, the curved anvils, steel rod, and cushion are added to improve the contact condition (Dai et al., 2010, Gomez et al., 2001). While the improvements turn out to be inefficient considering the manufacturing of the extra devices. The flatten Brazilian disc (FBD) method solves the loading issue effectively by truncating two parallel flat ends on the disc with a certain loading angle for the appliance of a uniformly distributed loading (Wang and Xing, 1999). The loading angle is determined to be within the range of 19.5°

to 30° to satisfy the datum assumption of the Brazilian test. The typical loading configurations for the Brazilian tensile test are shown in Figure 2-5. It has been successfully promoted to the dynamic testing regime on a range of materials including ceramic, concrete, and rock (Nojima and Ogawa, 1989; Ross and Tedesco, 1989; Dutta and Kim, 1993; Wang et al., 2006, 2009, and 2011). In this study, the loading angle is selected as 25°, and the modified equation for tensile strength calculation in the FBD specimen is given as (Pei et al., 2020; Liu et al., 2017 and 2018).

$$\sigma_t = 0.9445\frac{2P}{\pi DB} \tag{2-32}$$

Note that Equation (2-32) is derived based on the pure rock material. For an inclusion-bearing specimen, the calculated tensile strength does not solely represent the tensile strength of the rock part and can be affected by the dynamic response of the inclusion part. Hence, the nominal tensile strength is used to describe the tensile strength of the inclusion-bearing specimen.

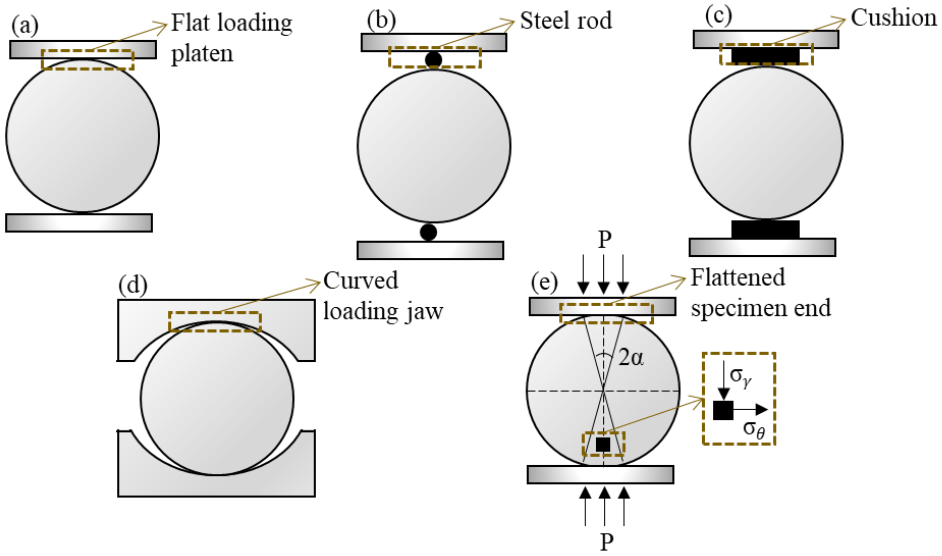

Figure 2-5 Typical Brazilian tensile test loading configurations: (a) flat loading platen, (b) flat loading platen with two thin steel rods, (c) flat loading platen with two cushions, (d) curved loading jaw, and (e) flat loading platen with flattened Brazilian disc (modified from Li and Wong (2013) and Wang et al. (2011)).

2.6 Discrete element method (DEM)

2.6.1 Introduction of DEM

As a supplement to laboratory tests, the discrete element method (DEM) provides an alternative to trace the real-time rock fracturing process, enabling a more comprehensive interpretation of the rock failure behavior and precise prediction of fracture properties (Bennett et al., 2015; Hornby et al., 1994; Kim et al., 2016; Wang et al., 2008; Cho et al., 2008; Wang et al., 2020 and 2021). DEM is capable of capturing the full-filed microscopic properties of rocks. It visualizes the initiation and propagation of microcracks from the micro-scale to coalesced fractures on the macro-scale without employing any complex constitutive law (Cundall, 2001). The micro-parameters are calibrated to reproduce the macro-scale response of rocks based on a number of trail-and-error tests (Itasca, 2010; Duan et al., 2015; Scholtès and Donzé, 2013; Potyondy and Cundall, 2004). The macro deformation properties (i.e., Young's modulus and Poisson's ratio) of rocks are influenced by the micro normal and shear bond stiffnesses and determined via the uniaxial compression tests. By adjusting the micro tensile and shear strength of bonds, the macro rock strengths can be calibrated by virtue of dynamic tests (Yan et al., 2020; Du et al., 2017).

Initially, DEM is applied in discovering the performance of granular materials by Cundall and Strack (1979) It is now extended to geomechanics with respect to diverse applications such as rock engineering, underground mining, petroleum engineering, etc. (Wang and Tonon, 2009; Cook et al., 2004; Ng, 2006; Schöpfer et al., 2009; Meng and

Wu, 2023). Besides, since DEM solves the motion of particles explicitly, it is thus reasonable to use it in dynamic simulations (Li et al., 2013). Two-dimensional DEM models are created in this study, the specimen and bars are represented as an assembly of rigid discs bonded at points of deformable contacts. The motion of particles obeys Newton's second law, and the contact force is deduced from the law of force-displacement in accordance with the selected contact model.

2.6.2 Parallel bond mode (PBM)

The particles are connected through parallel bond mode (PBM) in the DEM models. Figure 2-6 sketches a parallel bonded connecting two adjacent particles and its failure envelope. The breakage of PBM is associated with a reduction in bond stiffness, which benefits the simulation of rock-like materials (Martin, 1997). The failure criterion of PBM is given as (Cundall, 1971):

$$\frac{F_{nb}}{F_{nbMax}}+\frac{F_{sb}}{F_{sbMax}}+\frac{M_b}{M_{bMax}}\geq 1 \tag{2-33}$$

where F_{nb}, F_{sb}, and M_b denote the normal force, shear force, and bending moment, respectively, in which the respective maximum values are represented by F_{nbMax}, F_{sbMax}, and M_{bMax}, respectively.

Once the bond was broken, the contact mechanism between particles became cohesionless frictional, and the contact forces projected in the normal and shear directions were:

$$F_{nc}=K_nU_n, dF_{sc}=K_s dU_s \tag{2-34}$$

where F_{nc} and dF_{sc} are the normal and incremental shear contact forces at the current and previous time steps, respectively; K_n and K_s are the normal and shear stiffness,

respectively; and U_n and dU_s are the normal displacement and incremental tangential displacement between the current and previous time steps, respectively.

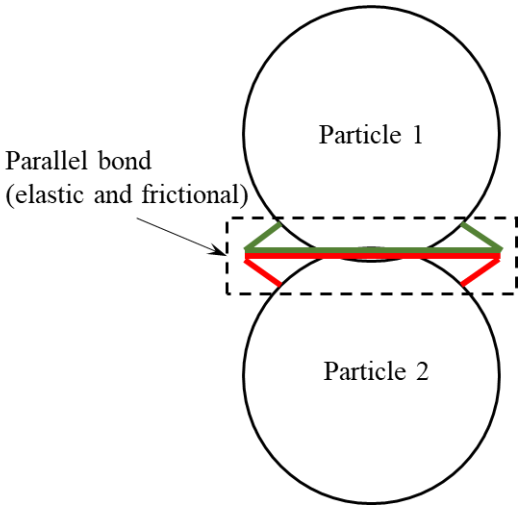

(a)

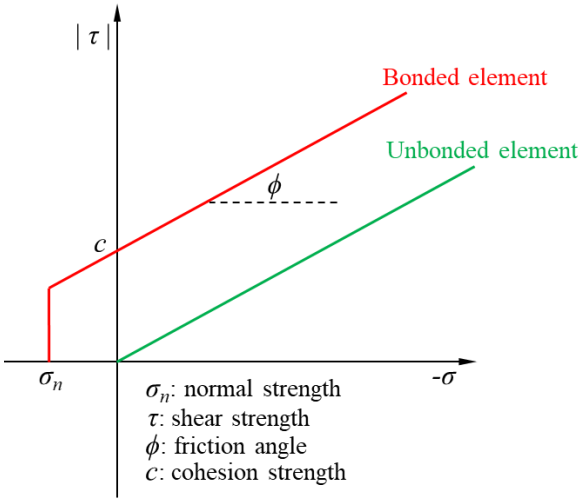

(b)

Figure 2-6 Sketches of the parallel bond: (a) a parallel-bonded contact with two neighboring particles, and (b) failure envelope (modified from Itasca (2010)).

2.6.3 Modelling of Acoustic Emission

As a reliable and non-destructive method for rock damage observation, the AE technique has been widely adopted in monitoring rock fracturing characteristics in laboratory experiments and site excavation (Amitrano, 2003; Lei, 2012; Lockner, 1993; Lockner et al., 1991; Young et al., 2000; Hirata et al., 2007; Ma J et al., 2020; Manthei, 2005; Thompson et al., 2009; Chang and Lee, 2004; Davi et al., 2013; Stierle et al., 2016). DEM models enable the AE monitoring by tracing the generation of microcracks when the applied stress surpasses the tensile or shear strength of the bonds (Imani et al., 2017). Each bond breakage releases the same amount of energy as the particles are approximately the same order of magnitude in bond strength. Taking each of the microcracks as an AE event contradict the power-law distribution (Gutenberg and Richter, 1944). To realistically reproduce the macro-mechanical rock behavior, the microcracks clustering close in space and time are considered to belong to a same AE event (Hazzard and Damjanac, 2013). When a bond breaks, the motions of two source particles on either side of the crack can deform the surrounding contacts. The moment tensor sums the components of force changes at contacts around the event (Bowers and Hudson, 1999):

$$M_{ij} = \sum_{S} \Delta F_i R_j \tag{2-35}$$

where ΔF_i is the *i*th component of the force change in contact, R_j is the *j*th component of the distance between the contact point and the geometrical center of the event, and S is the number of contacts involved in an AE event.

The eigenvalue decomposed from the moment tensor matrix represented the amplitude of the forces acting at an event, and is used for the calculation of scalar moment (Hazzard and Young, 2002):

$$M_0 = \left(\frac{\sum_{j=1}^{3} m_j^2}{2} \right)^{1/2} \tag{2-36}$$

where m_j is the *j*th eigenvalue of the moment tensor matrix.

The magnitude of the AE event is then derived from the scalar moment (Hazzard and Young, 2000 and 2004; Hazzard et al., 2000):

$$M_w = \frac{2}{3} \log M_0 - 6 \tag{2-37}$$

The discrete fracture network (DFN) module in DEM enables the recognition of fracture population, in which the AE source mechanism is classified into two types including tensile and shear failures (Itasca, 2010). However, the detected amount of shear fractures is nearly negligible when compared to that of the tensile fractures in studies of rock dynamics (Zhou et al., 2021; Duan and Kwok, 2015). By decomposing the moment tensor, the ratio between the two deduced components (i.e., isotropic part and deviatoric part) can quantify the failure mechanism of an AE event (Feignier and Young, 1992):

$$R = \frac{tr(M) \times 100}{(|tr(M)| + \sum |m_i^*|)} \tag{2-38}$$

where $tr(M)$ is the trace of the moment tensor, m_i and $m_i^* (i = 1, 2, 3)$ are the eigenvalue and partial eigenvalue, $m_i^* = m_i - tr(M)/3$. The ratio R ranges from -100 (pure explosion) to 100 (pure implosion). For $R < -30$, the event is considered as "compaction", for $R > 30$, the event is identified as "tensile", for $-30 < R < 30$, it is termed a shear failure in nature. Figure 2-7 sketches an AE event fails in a tensile failure mechanism (R = 47.06).

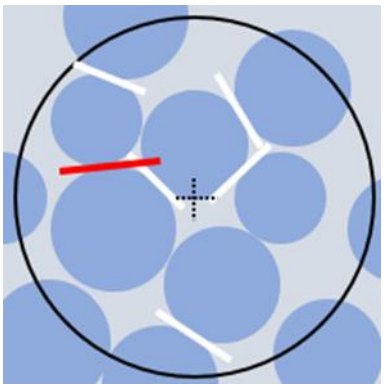

Figure 2-7 A typical tensile failure mechanism of an AE event. Blue circle represents the disc. Red and white segments indicate micro-shear and micro-tensile fractures, respectively. The region bounded by a black circle implies an AE event.

2.6.4 Thermal modelling

Thermal modelling allows the simulation of transient heat conduction and the evolution of thermally induced force changes (Itasca, 2010). This algorithm assumes that the thermal material is discretized into a network of heat reservoirs (i.e., particles) and thermal pipes (i.e., activated contacts between particles). Heat flow occurs via conduction in the active thermal contacts that connect the reservoirs. The parameters associated with each reservoir are temperature (T), mass (m_t), volume (V_b), specific heat (C_v), and coefficient of linear thermal expansion (α_t). Associated with each thermal contact are a power (Q) and thermal resistance (η_t) per unit length, and the updating of Q is based on the temperature difference (ΔT) in the two connecting particles at each end of the thermal pipe.

$$Q = -\frac{\Delta T}{\eta_t L_t} \tag{2-39}$$

where L_t is the length of the thermal pipe. The heat conduction formular for a single reservoir with several pipes (n_t) is given by:

$$-\sum_{1}^{n_t} Q + Q_v = m_t C_v \frac{\partial T}{\partial t} \tag{2-40}$$

where Q_v is the heat-source intensity. The thermal resistance assigned to each pipe for a thermally homogeneous material is expressed as:

$$\eta_t = \frac{1}{2K_t}\left(\frac{1-\phi}{\sum_{N_b} V_b}\right)\sum_{N_p} L_t \tag{2-41}$$

where K_t is thermal conductivity, ϕ is porosity, N_b and N_p are the numbers of particles and pipes in the volume of interest.

The thermal strain resulting from the thermal expansion is accounted for by changing the particle radii and updating the bond forces. Given a certain temperature difference, the change of the particle radius (R_t) is calculated as:

$$\Delta R_t = \alpha_t R_t \Delta T \tag{2-42}$$

The normal force (F^n) carried by the contact bond can be affected by the thermal strain as well, the value of which is related to the change of the contact length:

$$\Delta F^n = -k^n A(\alpha_t L \Delta T) \tag{2-43}$$

where k^n is the normal stiffness of the bond, A is the cross-section area of the bond.

2.7 Expansive mortar

2.7.1 Material property and performance of expansive mortar

In the 1930s, Henri Lossier invented expansive mortar, which is initially introduced in Japan in early 1970s. It is failed to be widely applied in the industry during the past four decades due to the insufficient knowledge of expansive mortar's characteristics as well as the limited research. Expansive mortar is a greyish cementitious powdery substance with free lime (CaO) as its main component. The material properties and chemical composition of a typically commercialized expansive mortar (e.g., Bristar 100 are given in Table 2-1. The hydration process of CaO which takes the majority of the expansive mortar expansion can be explained by the volumetric expansion based on the swelling theory and crystal growth theory (De Silva et al., 2016). Figure 2-8 graphically represents the hydration mechanism of $Ca(OH)_2$ using Shalom's spherical model (De Silva et al., 2017; Ish-Shalom and Bentur, 1975). After mixing expansive mortar with an appropriate amount of water, the formation of $Ca(OH)_2$ crystals envelops the hydrating CaO causing the volume expansion in the crystal structure system. When it proceeds to the critical degree of hydration, the scattered $Ca(OH)_2$ particles grow to contact with their neighbors and will generate further expansive pressure if external confinement is provided. While the expansion of expansive mortar with no constraint results in a highly porous structure and thus lesser expected expansive pressure generation. De Silva et al. (2017) carried out a series of SEM scanning to present the hydration process of expansive mortar under restrained conditions. The hexagonal Portlandite $Ca(OH)_2$ structure is clearly observed after 6 hours' hydration, and the needle-like Ettringite crystalline structure and a gel-like substance Calcium Silicate Hydrate (CSH) are identified subsequently (Figure 2-9). These three main products forming in the hydrating expansive mortar system are expressed by the reactions in Equations (2-44) -(2-46):

$$CaO + H_2O \rightarrow Ca(OH)_2 \quad (2\text{-}44)$$

$$3CaO.Al_2O_3 + 3CaSO_4 .2H_2O + 26H_2O \rightarrow 3CaO.Al_2O_3 .3CaSO_4 .32H_2O \quad (2\text{-}45)$$

$$3CaO.SiO_2 + 3.9H_2O \rightarrow 1.7CaO.SiO_2 .2.6H_2O + 1.3Ca(OH)_2 \quad (2\text{-}46)$$

Table 2-1 Material properties and chemical composition of Bristar 100 (De Silva et al., 2017; Harada et al., 1993; Laefer et al., 2010; Natanzi et al., 2016).

Properties	
Specific gravity	3.14
Bulk density	1050 kg/m3
pH	13
Chemical composition	**Percentage by mass**
SiO_2	8.5
Al_2O_3	2.0
Fe_2O_3	0.9
CaO	82.9
MgO	0.7
SO_3	3.3
Igloss	1.3

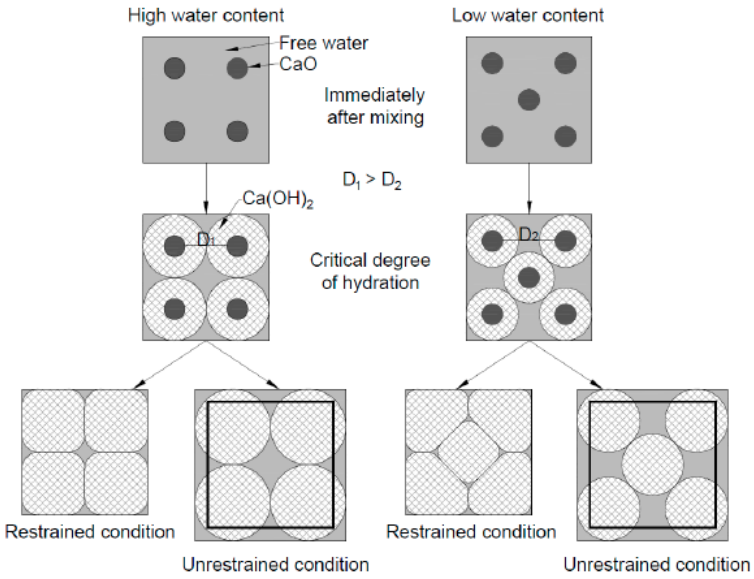

Figure 2-8 Shalom's sphere model for hydration mechanism of $Ca(OH)_2$ (De Silva et al., 2017; Ish-Shalom and Bentur, 1975).

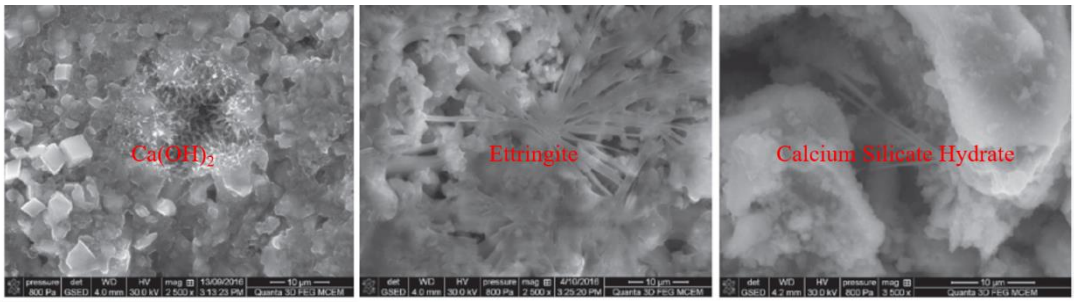

(a) (b) (c)

Figure 2-9 ESEM images of main expansive mortar hydration products, (a) $Ca(OH)_2$, (b) Ettringite, (c) Calcium Silicate Hydrate (De Silva et al., 2017).

2.7.2 Application of expansive mortar

Based on the demands of social development, concrete demolition work becomes quite common for the sake of structural construction, renovation, dismantlement, etc. However, the traditional drilling and blasting methods can easily lead to ground vibration, which may provoke complaints from densely populated cities. Expansive mortar offers an alternative to mitigate these concerns (Walker et al., 1996; Arshadnejad and Niu, 2014). The effectiveness of the demolition process has been studied widely for concrete structures in considering the hole number, spacing and diameter. (Harada et al., 1989; Natanzi and Laefer, 2014; Swanson and Labuz, 1999). Gambatese (2003) revealed that expansive mortar can create a controlled cracking of concrete on a small scale. An empirical equation is established to predict a U-shaped crack path based on the relationship between the hole spacing and concrete strength (Cho et al., 2018).

Due to the effective control of crack generation and less environmental impacts, rock fracturing in quarries by virtue of the expansive mortar is broadly adopted recently. Hanif et al. (2007) studied the crack initiation and propagation of granite by pouring the expansive mortar into a set of holes with various spacings. Musunuri and Mitri (2009) examined the crack path of expansive mortar-filled norite rock under the condition of

uniaxial loading. Tang et al. (2017) considered the effect of rock heterogeneity by simulating the crack growth among the desired hole spacing. By compiling numerous experimental data, Arshadnejad et al. (2011) derived an empirical equation to estimate the evolution of expansive pressure as a function of the rock elastic modulus. The influence of expansive mortar on the coal-seam roof rock fracturing is revealed via acoustic emission monitoring and infrared thermal imagery (Xu et al., 2017; Zhai et al., 2018). It turns out that the greater the fractal dimension, the higher the fracture density and a more complex fracturing morphology.

The resource recovery efficiency in applications of unconventional oil/gas and minerals, hydraulic fracturing, and in-situ leaching relies highly on the permeability of the host rock. Artificial fracture manipulation is then applied to facilitate more channels in the shale reservoirs for oil and gas circulations as well as the flow of leaching solution in the impervious rock mass. Currently, expansive mortar has been proposed to facilitate the in-situ leaching. It is capable to create a complex fracture network rather than a simple planar fracture by conventional hydraulic fracturing method. De Silva et al. (2018a) numerically studied the fracturing performance of expansive mortar under different confining pressures. The results show that the expansive pressure could result in multiple radial fractures, and the complexity of the fracture morphology is positively correlated with the confining pressure. As opposed to inject the expansive mortar continuously at once in the in-situ leaching, De Silva and Ranjith (2019) introduced another two methods (i.e., intermittent charging and multi-stage charging), which exhibits an improved fracturing efficiency and an optimized fracture network. Guo et al. (2015a) investigated the fracture pattern of expansive mortar filled cubic shale block under true triaxial conditions. The data shows that the shale reservoir stimulation is more effective through simultaneous fracturing. By locating AE activities during the coring of expansive mortar filled sandstone and shale specimens, Guo et al. (2015b) explained the relationships between the fracture network and rock hardness and brittleness.

2.8 Summary

The technology acceleration in rock engineering aiming a safer and more efficient underground excavation and energy extraction has been implemented in several fields such as excavation techniques (Wu, 2021). The dynamic disturbance, extreme temperature, and anisotropic rock mass are often associated with complex geological conditions in the context of underground rock excavation. The expansion of expansive mortar by reacting with water offers an alternative to break the rock masses. The modelling of tensile behaviors of incluison-bearing rocks expand the study of a specific inclusion (i.e., expansive mortar). The numerical simulation enables the microscopic observation of rock failure process. However, the research work that is geared toward the dynamic performance of inclusion-bearing rocks is still enigmatic. It is expected that the elucidation of dynamic failure characteristics may provide a promising reference for underground rock excavation. The evaluation of rock abrasivity for rocks undergoing extreme temperature treatment (e.g., high temperature followed by rapid cooling) is significant in assessing the cutting-tool wear and rock-breaking efficiency. Foremost, as a significant indicator for rock cuttability and drillability during underground excavation, the evaluation of rock brittleness with a proper approach under mechanical and thermal effects is thus of the essence.

CHAPTER 3 METHODOLOGY

In this chapter, the SHPB technique, CAI test device, AE system, non-destructive ultrasonic tester, optical microscope, and numerical methods are introduced (Table 3-1). SHPB a is commonly used apparatus to study the dynamic mechanical properties of materials at the strain rate of $10^1 – 10^4$ s^{-1}. The CAI test is widely used to determine rock abrasivity, which can assess the tool wear performance in tunneling and drilling applications. The non-destructive ultrasonic tester is able to measure the P-wave velocity of rocks. The optical microscopic observation enables the wear flat quantification of the stylus. The use of numerical methods can facilitate the understanding of the rock failure process from a microscopic perspective.

Table 3-1 Summary of research objectives in accordance with experimental and numerical methods.

Research objectives	Experimental and numerical methods
Dynamic response of expansive mortar filled rocks	SHPB test, FEM simulation
Dynamic tensile behavior of inclusion-bearing rocks	DEM simulation, FBD method
Coupled thermal and cooling effects on rock abrasivity	CAI test, AE monitoring, P-wave velocity measurement, Microscopic observation

3.1 SHPB test apparatus

A standard SHPB system consists of two main parts: impact apparatus and signal-processing component. As shown in Figure 3-1, a gas gun, a striker bar, an incident bar, a transmitted bar, and a momentum trap constitute the impact part (Duan et al., 2019b). The striker bar is propelled by the gas gun at the desired pressure towards the front end

of the incident bar. The impact-induced compression wave propagating along the incident bar will be partially reflected upon reaching the specimen-incident bar interface due to the mismatch of material impedances, while others go through to the transmitted bar. The wave transmitting back and forth within the sandwiched specimen deforms it plastically. A stopper as the momentum trap mounted at the tail of the system is used to eliminate the multiple dynamic loading. A copper disc is attached to the front surface of the incident bar as a pulse shaper. As for the signal-processing, the electronic signals collected from two strain gauges affixed oppositely in both incident and transmitted bar are initially amplified by the strain meters and transformed later into the digital signals using the oscilloscope. The stress-stain relationship in the specimen is then derived based on the data recorded in the oscilloscope.

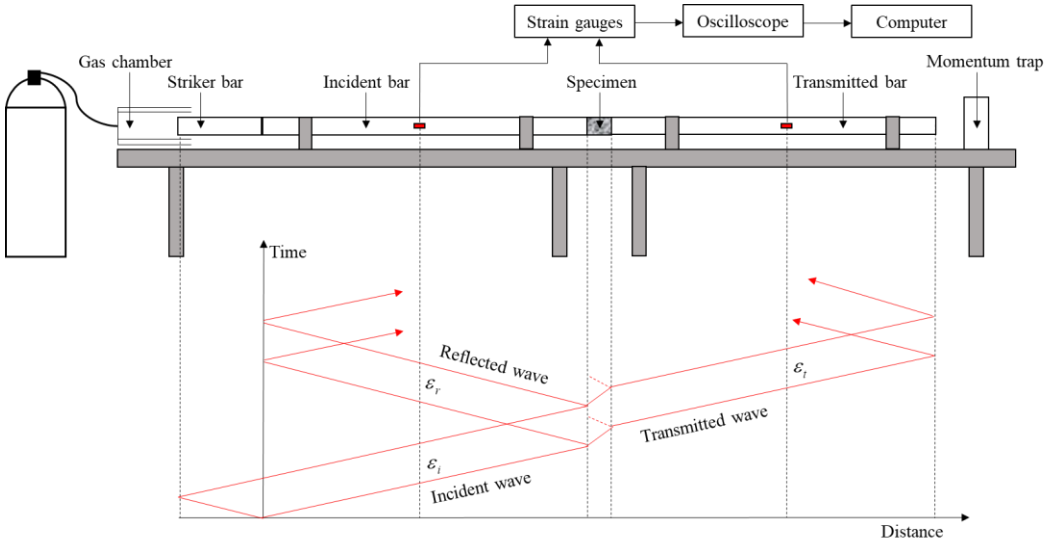

(a)

(b)

Figure 3-1 (a) Schematic, and (b) laboratory SHPB testing facilities.

3.2 CAI test apparatus

The CAI test is intended as an index measurement for classifying the rock abravisity (Alber et al., 2014). The wear of the stylus tip during the scratching process on the rock surface may shed light on tool consumption in drilling and tunnelling practices. There are two stampers of testing including the original Cerchar design (Cerchar, 1986) and the developed West layout (West, 1989), in which the latter prevails in applications. Both devices feature a vice and a steel stylus loaded with a static weight of 70 N, while the difference in equipment actuation results in a faster scratching velocity in the Cerchar apparatus. As shown in Figures 3-2a and 3-2b, the operation of the hand lever in the Cerchar apparatus can directly drive the scratch of the stylus over the rock surface. In contrast, the West design controls the hand crank to move the rock under the stylus. However, the CAI values estimated from the two methods turns out to be similar when ignoring the effect of testing velocity (Plinninger et al., 2003). Side view tip wear flat measurement is recommended, and the correct and invalid worn profiles are shown in Figure 3-3. The CAI value is calculated as 10 times the tip wear flat of the stylus. In this study, the CAI tests are carried out using a modified West apparatus as shown in Figure

3-2c (Ji et al., 2021). This apparatus mainly consists of a dead weight, a pin chuck, a stylus, and a sample stand. The stylus with a conical angle of 90° has a Rockwell Hardness Scale (HRC) of 54. Under a normal load of 70 N, the stylus clamped in the pin chuck can scratch the specimen firmly fixed on the sample stand.

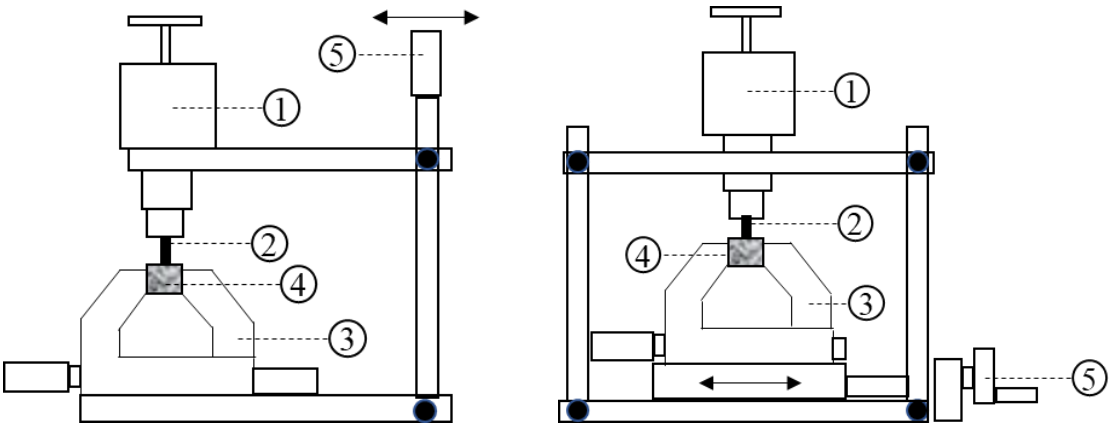

(a) (b)

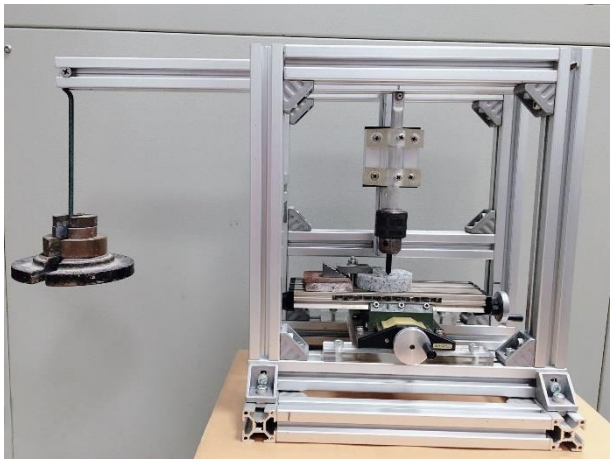

(c)

Figure 3-2 Sketches of CAI testing devices according to (a) Cerchar apparatus (Cerchar, 1986): 1 weight; 2 testing stylus and stylus chunk; 3 sample vice; 4 rock; 5 hand lever (b) West apparatus (West, 1989): 1 weight; 2 testing stylus and stylus guide; 3 vice sled; 4 rock; 5 hand crank, and (c) customized apparatus developed from the West design.

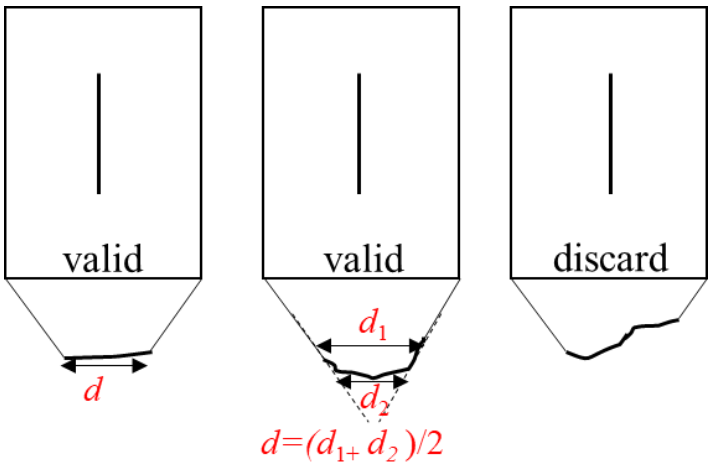

Figure 3-3 Worn profiles of stylus with valid measurement results and the corresponding wear flat (*d)*, and a non-standard example that should be discarded.

3.3 Acoustic emission system

The SAMOS AE system (Figure 3-4) is cooperated with the CAI test apparatus to record the AE energy characteristics during the scratching process. AE can be defined as a transit elastic wave formed from the rapid energy release when the material is deformed under stress (Ji and Wu, 2020). Four channels are used in each test based on one PCI-8 processing board. Each channel contains a 16 bit, 3 MHz A/D converter, four High Pass, and four Low Pass software selectable filters. The AE signal detected by the Pico sensor is amplified by the Pre-amplifier, which allows the selection of either 20, 40, or 60 gain. Figure 3-5 shows a typical AE hit feature, and the related terminologies used in the AE detection are listed below.

(1) Time of hit: The time when the AE hit is detected, where the AE amplitude exceeds the AE threshold.

(2) Rise time: The time between the beginning of the AE hit and its peak amplitude.

(3) AE amplitude: The maximum (positive or negative) AE signal excursion during an AE hit. The amplitude is expressed as dB = 20 log (V_{max}/1μ-*volt*) – (Preamplifier Gain in dB), where V_{max} is the maximum voltage.

(4) AE threshold: It records a threshold value at the time of an AE hit and is adopted only when an adaptive Threshold technique is used.

(5) AE duration: The time interval between the first and the last AE threshold of the AE hit.

(6) AE counts: It counts the number of AE signal excursions over the AE threshold.

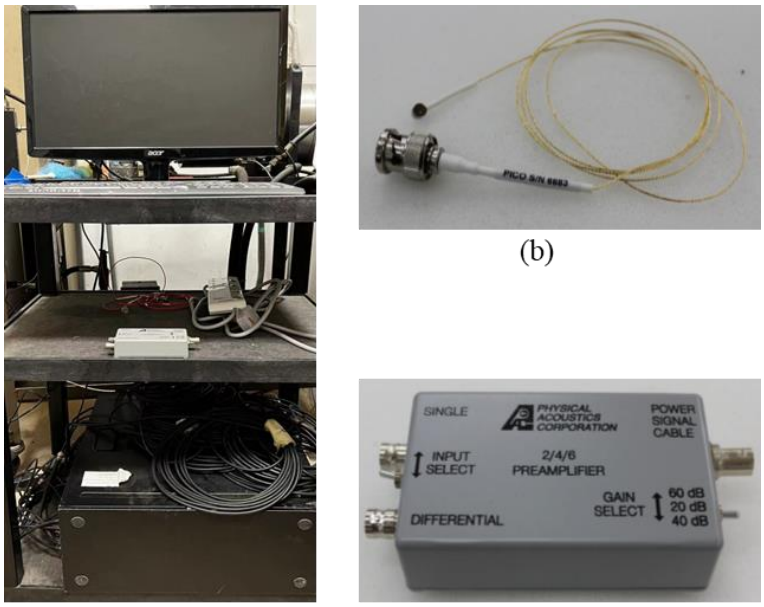

(a) (b) (c)

Figure 3-4 (a) AE system with console and monitor, (b) Pico ultra mini WB sensor, and (c) Pre-amplifier.

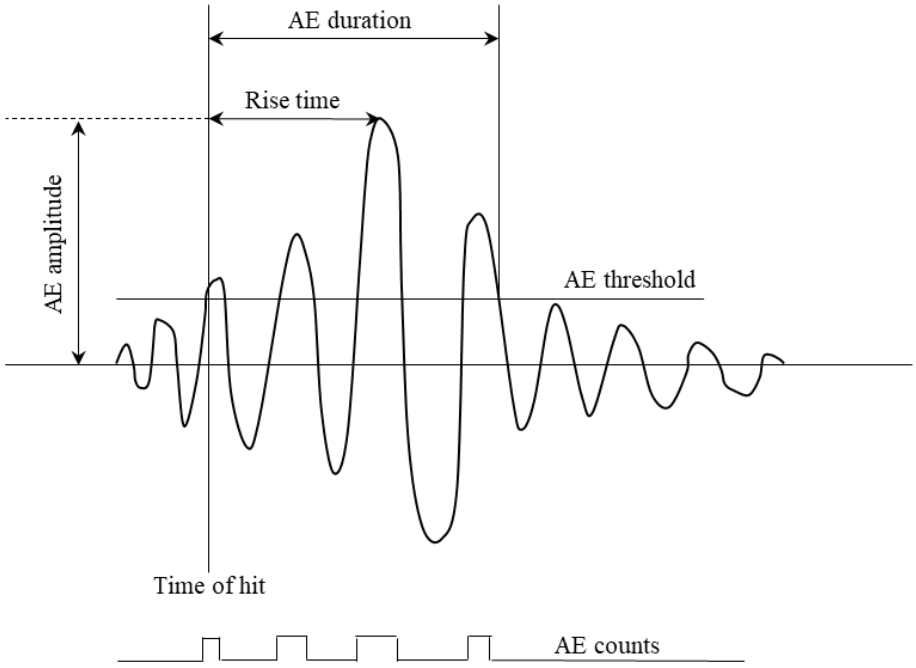

Figure 3-5 An AE hit feature extraction illustration.

3.4 P-wave velocity tester

The PROCEQ Portable Ultrasonic Non-destructive Digital Indicating Tester (PUNDIT) Lab Ultrasonic Velocity Test System is used in this study to measure the P-wave velocity of the thermally treated specimens (Figure 3-6). The change of the P-wave velocity can indirectly reveal the degree of thermal induced damage (i.e., microcracking). The specimens are clamped by a pair of transducers operating at 54 kHz during the measurement. The P-wave velocity is derived based on the known specimen length and detected pulse propagation time.

Figure 3-6 Proceq Pundit lab plus ultrasonic tester.

3.5 Worn stylus measurement using microscope

A Nikon H550L polarizing microscope with a 4x magnification lens (Figure 3-7) is used to measure the wear flat of the worn stylus. The Element Basic Research (NIS) program allows the length measurement on the extracted digital photos via the live mode. A higher magnification lens (e.g., 10x or 20x) is also used to observe the distribution of thermal induced microcracks at different temperatures. It enables the investigation of intragranular microcracks propagated along grain boundaries and the intergranular microcracks initiated from the inside of the grain. The microscopic observation can be regarded as another powerful evidence to explain the thermal effect on rock properties.

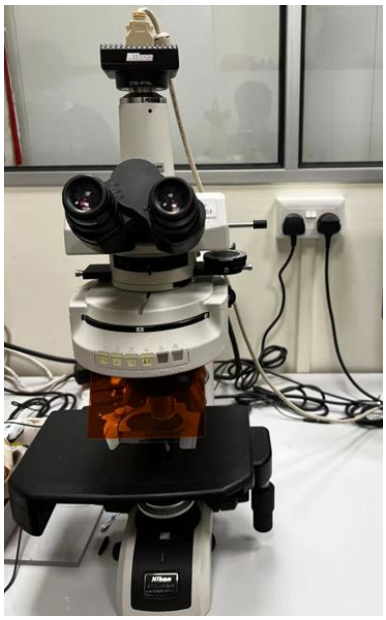

Figure 3-7 Nikon H550L polarizing microscope.

3.6 Numerical methods

The FEM enables an approximation of continuous functions as discrete frameworks for investigations of crack growth process. It offers great freedom in discretization selection by constructing different types of meshes, which involve a bunch of finite elements connected at nodes (Figure 3-8). The function of conventional FEM is limited to the simulation of a complex crack morphology due to the re-meshing during the crack propagation and the refining of meshes at the crack tip (Chen et al., 2022). As a built-in package in Abaqus software, the eXtended FEM (XFEM) combats such issues and allows the digital capture of the multiple crack intersections (Daux et al., 2000). The XFEM has been widely applied in engineering practice to solve problems such as fracture toughness and fatigue fracture (Cruz et al., 2009; Wei et al., 2016). By virtue of the user-defined element subroutine, the phase-field model for brittle fracture is implemented to study the fracture mechanism without tracing the discontinuities in the displacement field (Msekh et al., 2015). In this study, the brittle cracking model in Abaqus is used to simulate the crack propagation by removing the corresponding elements when the

dynamic fracture energy for crack propagation is reached. The brittle cracking model provides the capability for modeling rock behaviors dominated by tensile cracking (Abaqus, 2014). Besides, this method fosters the interpretation of the generation of complex crack networks by omitting the complexity of XFEM formulations or other subroutines. It can reproduce the cracking behavior of plexiglas material when subjected to the indentation loading (Khan et al., 2016). In this study, a three-dimensional FEM model is established by Abaqus to interpret the dynamic failure characteristics of rocks with filled expansive mortar. The geometry and material properties of the mimic SHPB system are the same as those used in the laboratory test. The components of the SHPB system and the specimens are meshed using 3D eight-node continuum (C3D8R) elements (Figure 3-9a). The stress history for each element can be automatically recorded during the testing process and visualized in the post-processing.

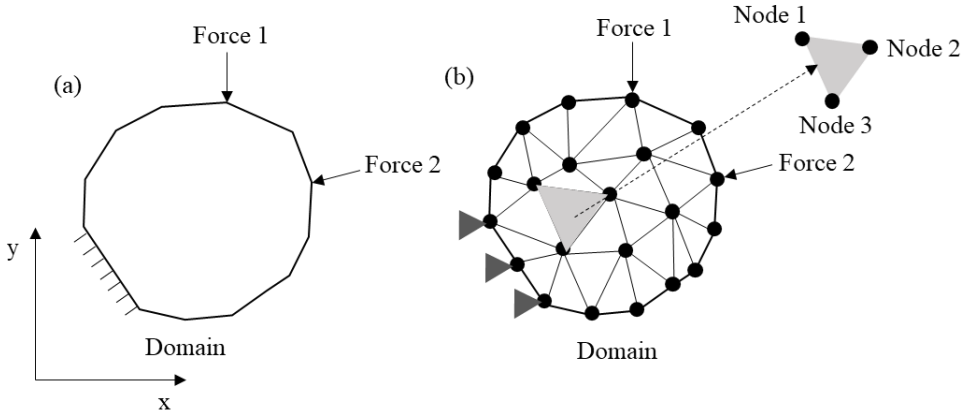

Figure 3-8 Sketches of (a) a 2D FEM domain, and (b) the finite element discretization with boundary conditions (modified from Tekkaya and Soyarslan, (2014)).

The DEM model is assembled by rigid particles and elastic bonds with assigned microscopic properties that are calibrated from the experiments. Compared with laboratory tests, DEM simulation has the following advantages: (i) eliminating the uncertainties caused by the rock heterogeneity and experimental implementation; (ii)

enabling the full-filed acquisition of the fracturing process during the entire loading (Bahaaddini et al., 2013; Patel and Martin, 2020; Zhao et al., 2020). A two-dimensional DEM model is established via the commercial software Particle Flow Code to investigate the coupled mechanical-thermal effect on dynamic tensile behavior of inclusion-bearing specimens (Figure 3-9b). The breakage of each bond indicates the generation of a microcrack. The statistical analysis of microcracks regarding microcrack numbers or energy provides a similar function as AE monitoring.

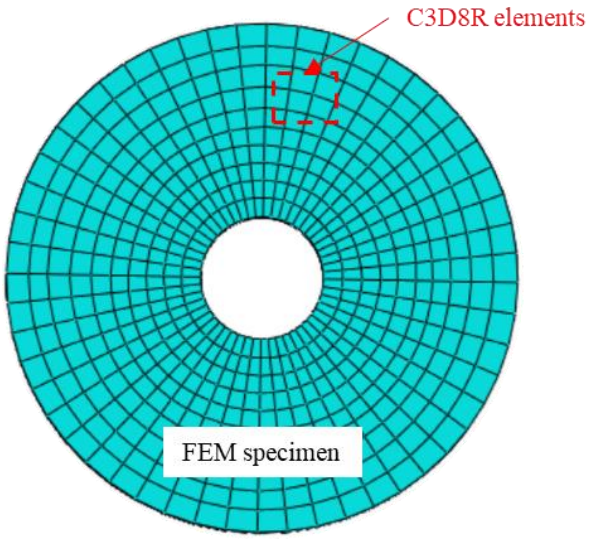

(a)

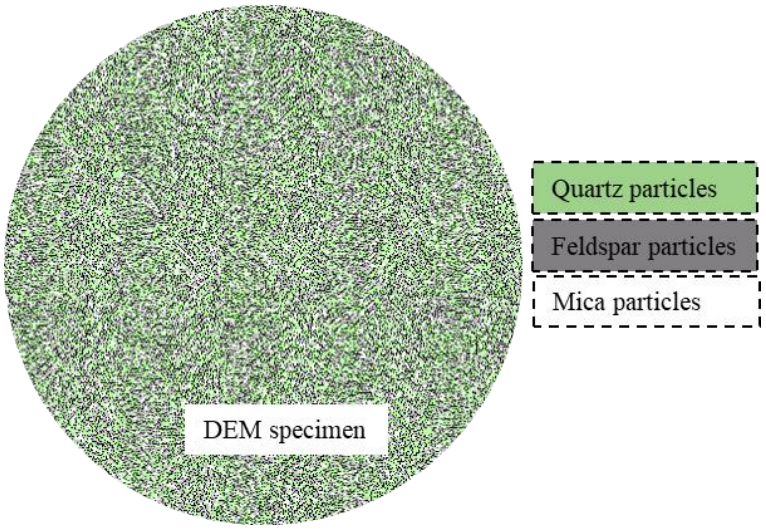

(b)

Figure 3-9 Simulated specimens in (a) FEM model, and (b) DEM model.

CHAPTER 4 CONTROL OF DYNAMIC FAILURE OF BRITTLE ROCK USING EXPANSIVE MORTAR

4.1 Introduction

The drill and blast method remains an efficient and inexpensive method of underground excavation. However, the poorly controlled method may lead to adverse impacts on the environment, such as rock overbreak and ground vibration. For example, if underground openings are developed close to fault zones, maintaining rock integrity in between could reduce the possibility of rock collapse and groundwater inrush (Singh and Xavier, 2005). If the openings are created in densely populated cities, the current wave-screening methods, such as active and passive isolation strategies as well as steps and ditches (Park et al., 2009; Xia et al., 2014), may not be cost-effective and applicable to control ground vibration. Expansive mortar is proposed as an alternative to explosives in concrete structure demolition and surface rock fracturing and is recently developed to assist underground excavation (Gambatese, 2003). Nevertheless, the expansion pressure is inefficiently developed from calcium oxide hydration and much lower than the strength of confined rock, which restricts the application of expansive mortar in underground excavation.

In rock dynamics, laboratory experiments use various techniques, such as ultrasonic waves (Yang et al., 2019; Zhang et al., 2020), pendulum hammer (Leucci and De Giorgi, 2006), spring mass system (Wu and Zhao, 2015, Wu et al., 2013 and 2015), and SHPB (Dai et al., 2016; Du et al., 2020 and 2021; Xia et al., 2008; Xu and Dai, 2018) to produce stress wave loading, which is controllable and measurable to evaluate the dynamic characteristics of brittle rock. The attempts are made in this study to overcome the restriction of expansive mortar in underground applications and to control the effectiveness of expansion pressure for more efficient rock fracturing. It is expected that the initial pressure provided by the expansive mortar could benefit the rock-breaking

efficiency with less wear of cutting tools and consumption of blasting agents by modifying the rock brittleness. The Abaqus/Explicit software is also used to qualitatively interpret the effect of expansive mortar on the failure pattern of surrounding rock under stress wave loading. This method incorporates both the advantages of the continuum- and discontinuum-based algorithms and is robust to solve the rock fracturing problem with complex boundary conditions (Xu and Cai, 2017).

This study aims to provide a laboratory verification for the application of dynamically amplified expansion pressure to achieve more efficient rock fracturing. First, the expansion pressure statically developed from the expansive mortar is evaluated, and an appropriate curing duration is determined. Then, the SHPB tests are conducted to evaluate the effectiveness of expansion pressure dynamically amplified during stress wave loading, in terms of rock failure pattern and stress wave attenuation. Subsequently, the rock fracturing process under combined static and dynamic loading is reproduced using the Abaqus/Explicit software. Finally, the competition between the expansion pressure and the radial inertia stress as well as the evolution of rock brittleness caused by the expansion pressure is discussed.

4.2 Experimental study

4.2.1 Test materials

Bukit Timah granite from central Singapore and Bristar 100 expansive mortar were used as rock and expansive materials, respectively. The medium-grained granite is composed of 62% feldspar, 32% quartz, 5% biotite, and 1% hornblende. The physical and mechanical properties of this granite are listed in Table 4-1. Eighteen specimens with a thickness of 25 mm were cut from 50-mm-diameter granite cores and polished at two ends using P280 sandpaper with a particle size of 52.2 μm. The specimens were equally divided into three groups: intact specimens, hollow specimens with 12-mm-diameter borehole drilled along the core axis, and filled specimens with the expansive mortar in

the borehole (Figure 4-1). The light-gray mortar mainly consists of calcium oxide (81-96%), silicon dioxide (1.5-8.0%), ferric oxide (0.2-3%), aluminum oxide (0.3-5%), sulfur trioxide (0.6-4.0%), and magnesium oxide (0-0.6%) (De Silva et al., 2017; Laefer et al., 2010). The density of expansive mortar is 1100 kg/m3.

Table 4-1 Mechanical and physical properties of Bukit Timah granite.

Parameter	Value
Bulk density (kg/m^3)	2660
Uniaxial compressive strength (MPa)	150
Tensile strength (MPa)	18
Young's modulus (GPa)	74
Poisson's ratio	0.15

(a)

(b)

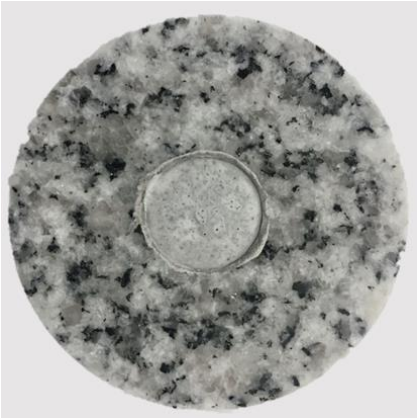

(c)

Figure 4-1 (a) Intact, (b) hollow, and (c) expansive mortar-filled granite specimens.

4.2.2 Expansion pressure evaluation

After the expansive mortar was filled in the borehole, the expansion pressure statically developed until the surrounding granite was broken. To estimate the influence of expansive mortar on the dynamic failure of the granite under stress wave loading, an appropriate curing duration should be determined to ensure that the statically developed expansion pressure was insufficient to induce undesired cracks in the granite. A thick-walled steel tube was to filled with the expansive mortar and the tangential strain (ε_{ts}) of the steel tube was measured using a pair of strain gauges to evaluate the expansion pressure (Figure 4-2 inset). The strain gauges were attached circumferentially at the center of the steel tube and connected to a data acquisition system with a sampling frequency of 1 Hz. The steel tube was 50 mm long, and the inner and outer diameters were 12 and 16 mm, respectively. After filling the expansive mortar with a water to expansive cement ratio of 0.3 in the steel tube at 25ºC ambient temperature, the expansion pressure (P_e) can be estimated as (Gholinejad and Arshadnejad, 2012):

$$P_e = \frac{\varepsilon_{ts} E_s \left(b^2 - a^2\right)}{2a^2} \tag{4-1}$$

where a and b are the inner and outer radii of the steel tube, respectively, and E_s is the elastic modulus of the steel tube (200 GPa).

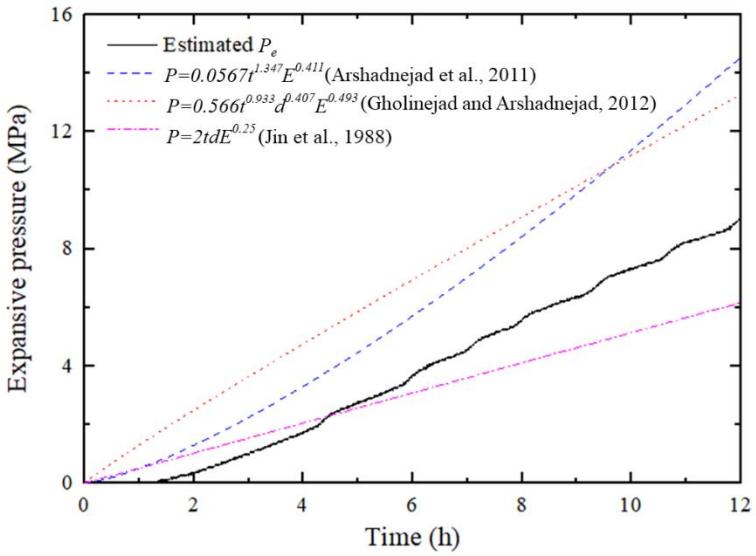

Figure 4-2 Development of expansive stress on a steel tube filled with expansive mortar, in comparison to the stresses estimated from previous studies.

A Charge-Coupled Device (CCD) camera combined with the Digital Image Correlation (DIC) method was used to observe the deformation of the granite around the borehole filled with the expansive mortar and to validate the curing duration before the dynamic tests (Rubino et al., 2019). The CCD camera with a resolution of 854 x 480 pixels was placed 15 cm away from the granite to capture the full-field strain at 60 frames per second, and the pixel size was 0.17 mm/pixel. The granite was coated by randomly spraying black speckles on a white background (Figure 4-3). The tangential strain of the granite was derived by tracking the locations of the speckles from the reference and deformed images captured during the mortar expansion. The DIC algorithm can be referred to Zhang and Zhao (2013) and was implemented in the Matlab code.

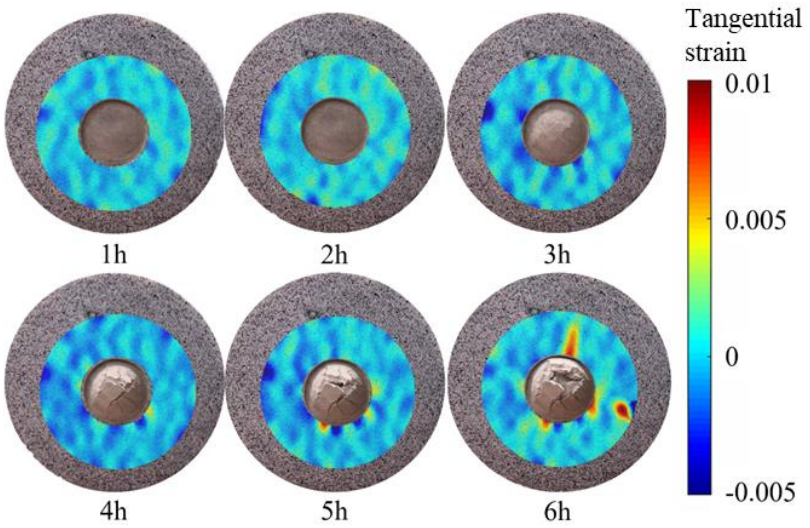

Figure 4-3 Evolution of tangential strain of surrounding granite adjacent to the borehole filled with expansive mortar.

Figure 4-2 shows the development of the expansion pressure due to mortar hydration. The increasing trend is similar to those obtained from previous studies (Arshadnejad et al., 2011; Gholinejad and Arshadnejad, 2012; Gambatese, 2003; Jin et al., 1988), but the slopes are different due to various test conditions and environments. In this case, the expansion pressure linearly rises in the first 4 hours. After that, the pressure increase fluctuates likely owing to the inelastic deformation of expansive mortar. The DIC results demonstrate that the tangential strain of the granite adjacent to the borehole filled with the expansive mortar is negligibly small in the first 4 hours (Figure 4-3). However, the strain concentration in the adjacent granite is observed in the 5th hour and extends subsequently. The filled mortar expands in the first 4 hours and spalls off from the 5th hour, which explains the fluctuation of pressure increase. Hence, a curing duration of 4 hours is determined before the dynamic tests.

4.2.3 SHPB tests

A series of SHPB tests were carried out on the intact, hollow, and filled specimens. The filled specimens were tested after the filled mortar was cured for 4 hours, and the statically developed expansive pressure was thus applied on the borehole wall. The 50-mm-diameter SHPB system comprises a gas gun, a striker bar (300 mm in length), incident and transmitted bars (each 2000 mm in length), and a momentum trap. The steel bars have a bulk density of 7900 kg/m^3, a P-wave velocity of 6000 m/s, and an elastic modulus of 210 GPa. The specimen was sandwiched between the incident and transmitted bars, and a thin layer of grease was filled at the specimen-bar interfaces to reduce undesired friction. The striker bar launched by the gas gun impacted the front end of the incident bar at a constant velocity of 12 m/s, and a sinusoidal P-wave was produced because a copper disc was placed at the front end as a pulse shaper. The momentum trap was fixed near the rear end of the transmitted bar to avoid multiple impacts. The incident (ε_i), reflected (ε_r), and transmitted (ε_t) waves were recorded at a sampling frequency of 1 MHz by two groups of strain gauges attached at the centers of the incident and transmitted bars.

Figure 4-4 summarizes the SHPB test results of the intact, hollow, and filled specimens. The incident, transmitted, and reflected waves recorded during the SHPB test on a filled specimen are shown in Figure 4-4a. The comparison between the superposed incident and reflected waves and the transmitted wave demonstrates that the dynamic stress equilibrium is achieved in the test (Figure 4-4b). The hollow specimen exhibits a lower dynamic strength than the intact specimen, which is consistent with previous results (e.g., Wang et al., 2018). From the stress-strain curves of both the specimens (Figure 4-4c), the strain at failure is very small, indicating the brittle failure occurs. The strength of the filled specimen is lower than that of the intact specimen (Figure 4-4d). However, the dynamic stress on the filled specimen increases in a longer duration than those on the intact and hollow specimens. Also, the strain rate is higher, and the strain at failure is larger. The results reveal that the dynamically amplified expansion pressure makes the

granite in the filled specimen becomes less brittle. Additionally, the filled specimen fails with a large number of tangential and radial cracks, while the orientation of cracks is more consistently radial in the hollow specimen, and a limited number of randomly distributed cracks are induced in the intact specimen (Figure 4-5). Furthermore, the results of transmission coefficient, defined as the ratio of the peak stress of the transmitted wave to that of the incident wave, indicate that the expansive mortar promotes wave attenuation due to an increase in crack number (Figure 4-6). The stress-strain relations and the failure modes of the filled specimen are beyond the understanding of the rock failure in the SHPB tests. As the conventional tests cannot provide insights into the rock failure associated with the dynamically amplified expansion pressure, the numerical simulation is used to interpret the influence of expansive mortar on the dynamic failure of the granite.

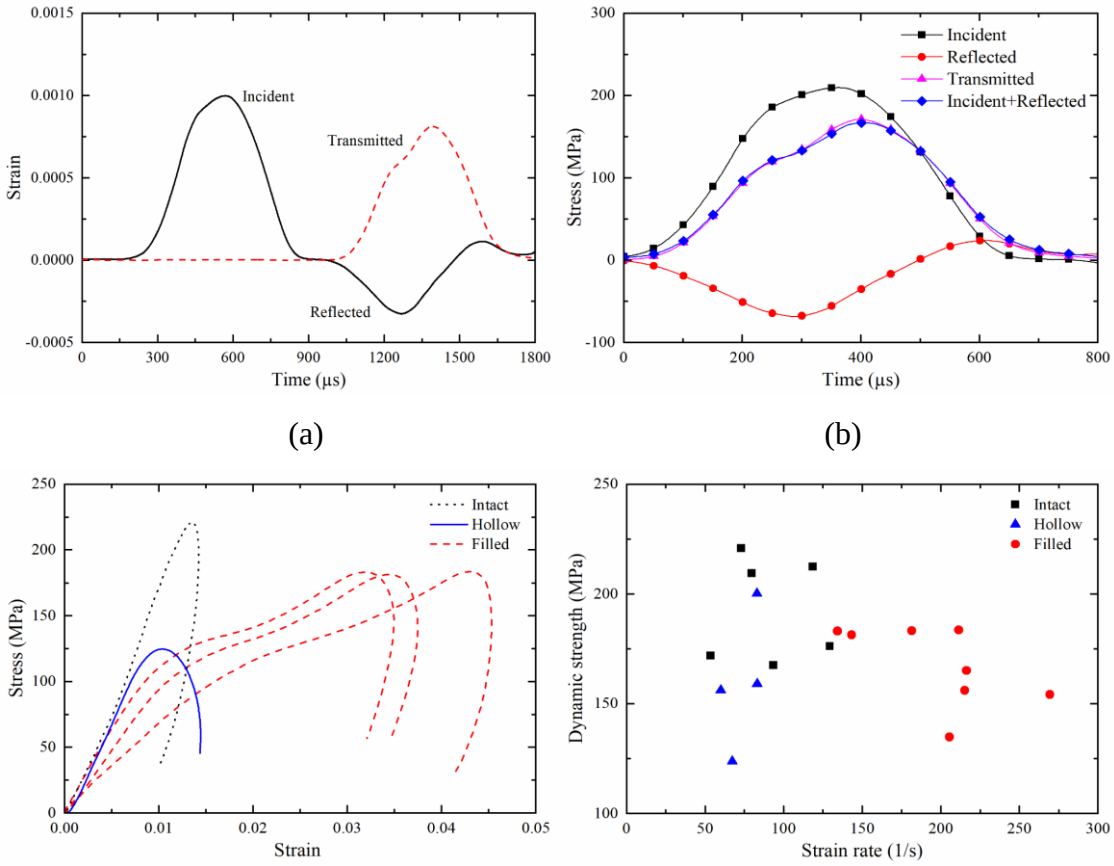

(c) (d)

Figure 4-4 SHPB test results of intact, hollow, and expansive mortar-filled granite specimens, (a) recorded waves from SHPB test on an expansive mortar-filled granite specimen, (b) dynamic stress equilibrium on the specimen, (c) typical stress-strain curves of intact, hollow, and expansive mortar-filled granite specimens, and (d) dynamic strengths of these specimens as a function of strain rate

(a)

(b)

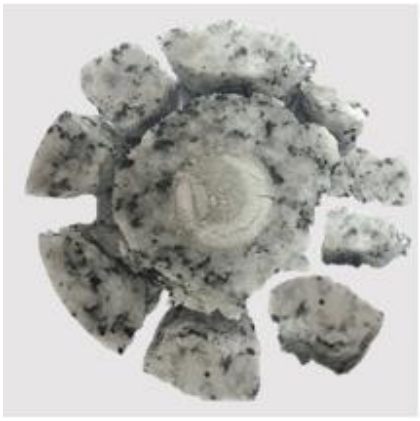

(c)

Figure 4-5 Failure patterns of (a) intact, (b) hollow, and (c) expansive mortar-filled granite specimens.

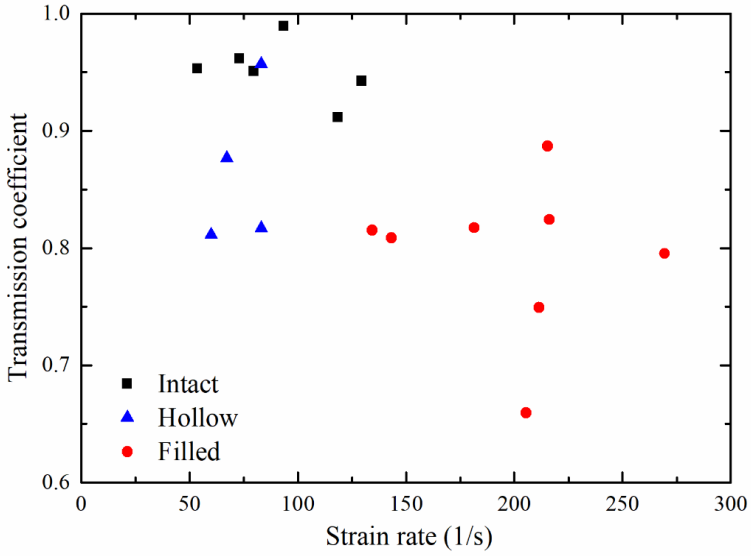

Figure 4-6 Transmission coefficients for intact, hollow, and expansive mortar-filled granite specimens as a function of strain rate

4.3 Numerical simulation

4.3.1 Model setup

The Abaqus/Explicit software is used to simulate the failure process of the surrounding granite in the filled specimen. In the three-dimensional (3D) analysis, the filled specimen, incident, and transmitted bars have the same geometrical, physical, and mechanical properties as those used in the SHPB tests (Table 4-1). Figure 4-7a illustrates the numerical model of the specimen, incident, and transmitted bars, which are composed of 10389, 55600, and 55600 C3D8R elements with reduced integration (Abaqus, 2014), respectively. It is assumed that the interfaces between the filled specimen and two bars are frictionless and controlled by the general contact algorithm, and the bars are constrained to move along the horizontal direction.

In the numerical simulation, a static pressure of 1.4 MPa is applied on the borehole wall, which was obtained after a curing duration of 4 hours (Figure 4-2). In the dynamic

analysis, an incident wave from the experimental study was imposed at the front end of the incident bar. The fracture energy model and the shear retention model were used to mimic Mode I and Mode II fracture behaviors, respectively (Abaqus, 2014). In this model, a crack is detected when the maximum principal tensile stress exceeds the dynamic tensile strength of the rock. When the dynamic fracture energy for crack growth is reached, the integration point of a C3D8R element fails, triggering the removal criterion of the corresponding element. The control parameters for the granite failure used in the model are estimated based on empirical relationships and other rock parameters (Table 4-2) and can be more reasonable if direct measurements are performed. Figure 4-7b compares the dynamic stresses on the filled specimen obtained from the experimental and numerical studies, which validate the numerical model to reproduce the dynamic responses of the filled specimen

Table 4-2 Control parameters for granite failure in numerical simulation.

Parameter	Value
Density (kg/m^3)	2660
Poisson's ratio	0.15
Dynamic Young's modulus (GPa)	92
Dynamic tensile strength (MPa) (Li and Meng, 2003; Wu et al., 2000)	53
Dynamic mode I fracture toughness ($MPa \cdot m^{0.5}$) (Zhang, 2002)	2.54
Dynamic fracture energy (N/m) (Tang, 1997)	180
Maximum allowable strain after failure (Xie et al., 2009) [41]	10^{-4}

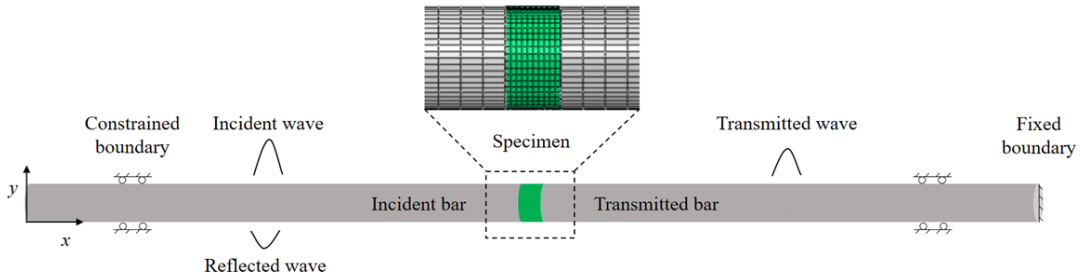

(a)

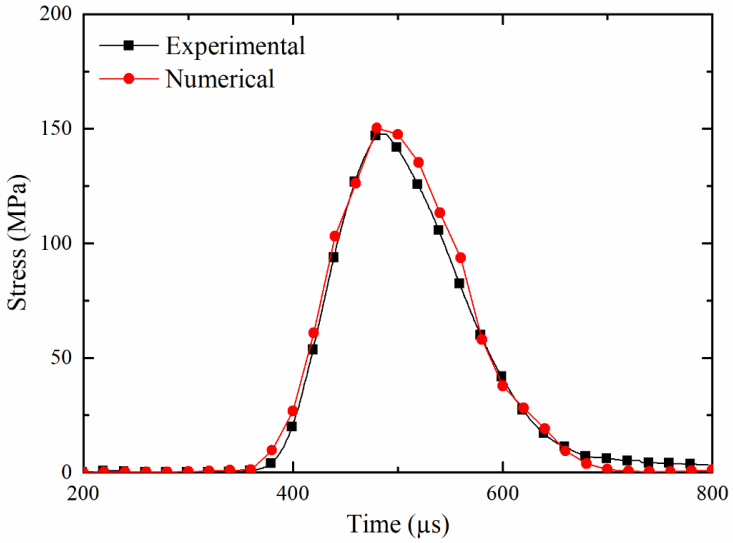

(b)

Figure 4-7 (a) Numerical simulation of SHPB test on rock specimen and zoomed-in mesh view of the specimen and bars, and (b) comparison of time-dependent stresses on filled specimen obtained from experimental and numerical studies.

4.3.2 Numerical results

The progressive failure of the filled specimen under stress wave loading is shown in Figure 4-8. Continuous tangential and scattered radial cracks appear in the granite before the axial stress on the filled specimen reaches the peak value at 480 μs (Figure 4-7b). Subsequently, the radial and randomly distributed cracks occur and coalesce with the tangential cracks. Finally, the granite breaks into many small pieces mainly along the tangential and radial cracks, and the failure pattern is similar to that in Figure 4-5c.

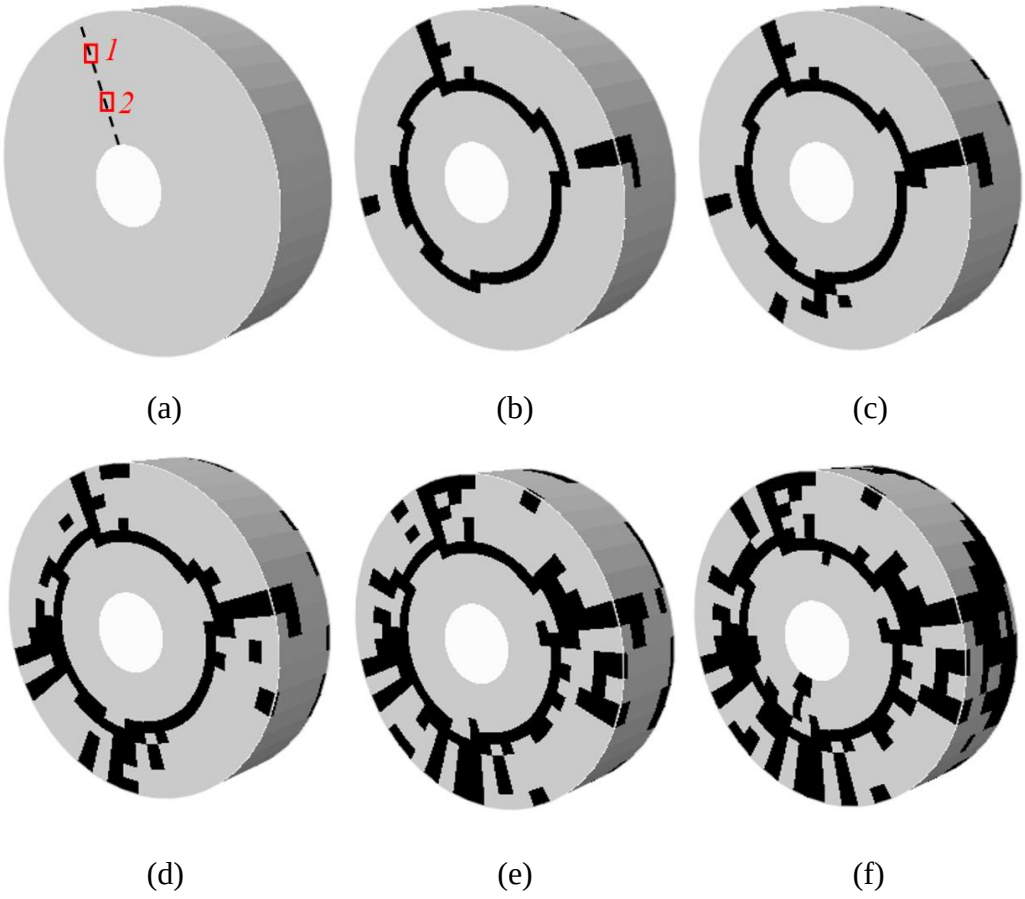

Figure 4-8 Crack development in surrounding granite of expansive mortar-filled specimen at (a) 420 μs, (b) 457 μs, (c) 467 μs, (d) 485 μs, (e) 511 μs, and (f) 579 μs. Elements 1 and 2 are selected as representative elements of radial and tangential cracks.

Elements 1 and 2 were selected as the representative elements in the tangential and radial cracks, respectively, to demonstrate the evolution of tangential and radial stresses in the failure process (Figure 4-8a). The definitions of tangential and radial stresses are given in a polar coordinate system (Figure 4-9a), and the tensile stress is considered as positive. For Element 1, the tangential stress steadily increases and exceeds the dynamic tensile strength of the granite (53 MPa), resulting in the formation of radial cracks (Figure 4-9b). After that, the radial stress dominates the stress field, accompanied by the occurrence

of tangential cracks. The tangential and radial stresses of Element 2 evolve similar to those of Element 1, but the tangential stress does not reach the dynamic tensile strength. Afterwards, the tangential cracks are formed under the dominating radial stress. The shear stresses on the elements are also shown in Figure 4-9, and the magnitudes are smaller than the other stresses and negligible in the failure analysis. The numerical results also indicate that the tangential and radial stresses induced during the stress wave loading are much higher than the statically induced expansion pressure, and the peak values may reach the dynamic tensile strength, resulting in the splitting failure of the granite.

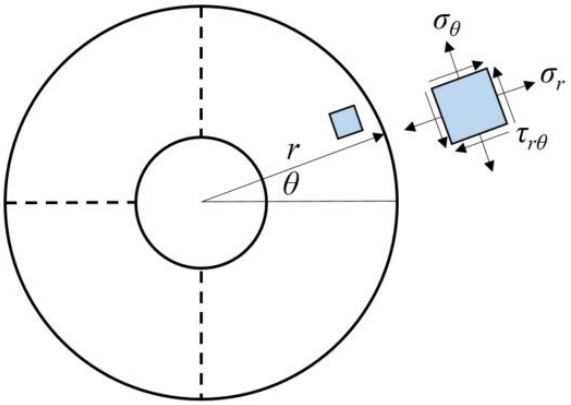

(a)

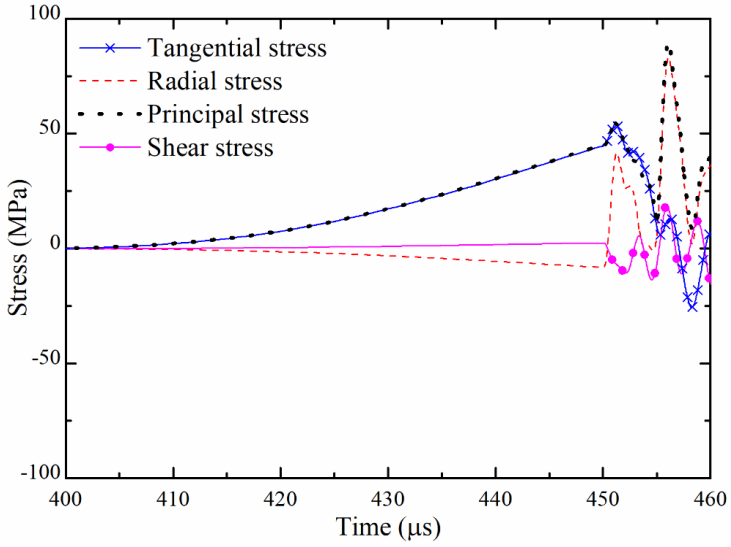

(b)

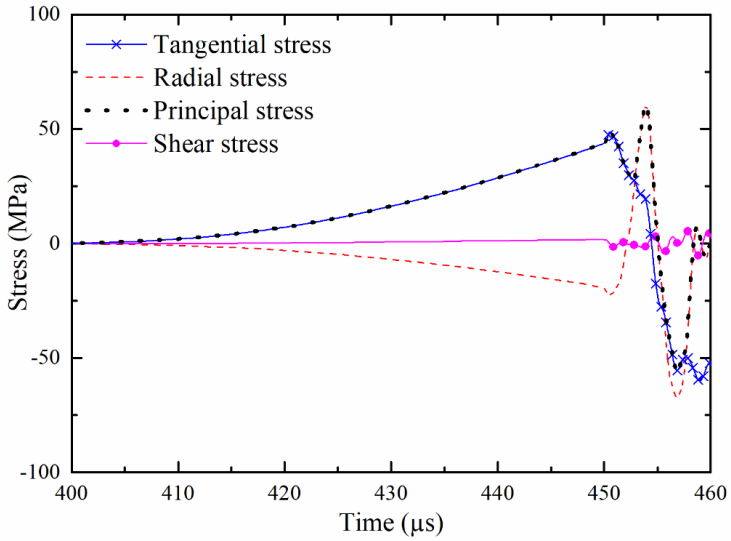

(c)

Figure 4-9 (a) Determination of radial stress (σ_r), tangential stress (σ_θ) and shear stress ($\tau_{r\theta}$), and the stresses on (b) Element 1 and (c) Element 2.

4.4 Discussion

The results demonstrate that the dynamically amplified expansion pressure from the expansive mortar under stress wave loading can be used to control the failure pattern of surrounding rock and reduce the energy release in the nearby environment. The effectiveness of expansive mortar in rock fracturing can be reflected by the competing process between the expansion pressure and the radial inertia stress. During the SHPB tests, the radial inertia stress (σ_{ri}) is induced to confine the specimen, opposite to the direction of the expansion pressure, and estimated as (Forrestal et al., 2007; Li and Meng, 2003):

$$\sigma_{ri} = -\frac{\nu(3-2\nu)}{8(1-\nu)}\left(R^2 - r^2\right)\rho\frac{d^2\varepsilon_z}{dt^2} \tag{4-2}$$

where r is the distance to the specimen centre, R is the specimen radius, ε_z is the axial strain, t is the elapsed time, v and ρ are the Poisson's ratio and density of the rock, respectively.

For three types of granite specimens under stress wave loading, the radial inertia stresses on the granite are less than 0.1 MPa (Figure 4-10). The expansion pressure from the expansive mortar statically applied on the borehole wall is 1.4 MPa, which is significantly amplified during the dynamic tests and become much greater than the radial inertia stress. The expansion pressure thus effectively induces cracks in the unconfined granite in this study. However, for deep underground projects, the expansion pressure should overcome not only the radial inertia stress under stress wave loading but also the high confining stress from crustal rocks. Hence, an expansive mortar with high pressurization capacity is needed for field applications under high stress conditions (De Silva et al., 2018a).

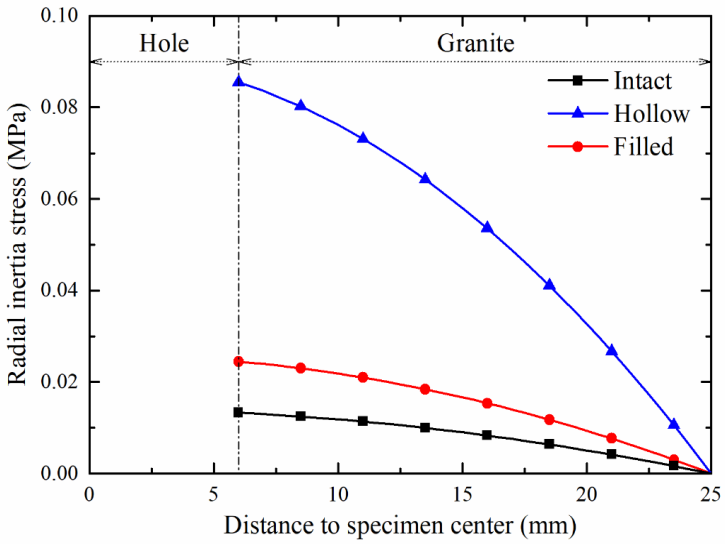

Figure 4-10 Radial inertia stresses of intact, hollow and expansive mortar-filled granite specimens as a function of distance to specimen centre.

The data also show that the filled specimen has larger strain at failure than the intact and hollow specimens, indicating that the expansion pressure from the expansive mortar modifies rock brittleness. Brittleness indices B_9 and B_{10} were used to describe the ratio between the post-peak rupture energy and the withdrawn elastic energy and the ratio between the released elastic energy and the withdrawn elastic energy, respectively (Tarasov and Potvin, 2013).

The unloading elastic and post-peak moduli were measured from the stress-strain curves of the intact, hollow, and filled specimens (Figure 4-4c) to calculate the brittleness indices. The intact specimens fall within the region with $B_9 < 1$ and $B_{10} > 0$ (black dotted box), which indicates that the specimens exhibit the brittle behaviors, while the filled specimens are all within the region with $B_9 > 1$ and $B_{10} < 0$ (red dotted box), showing the ductile behaviors of the specimens (Figure 4-11). The transition from the brittle to ductile behavior can be clearly observed among the three types of specimens along the orange diagonal line, particularly the hollow specimens. The results reveal that the expansive mortar modifies the brittleness of surrounding granite, which is characterized by extensive cracks and remarkable deformability. Therefore, the application of expansive mortar can be a robust tool to fundamentally change rock brittleness and to control the failure pattern of surrounding rock in underground excavation.

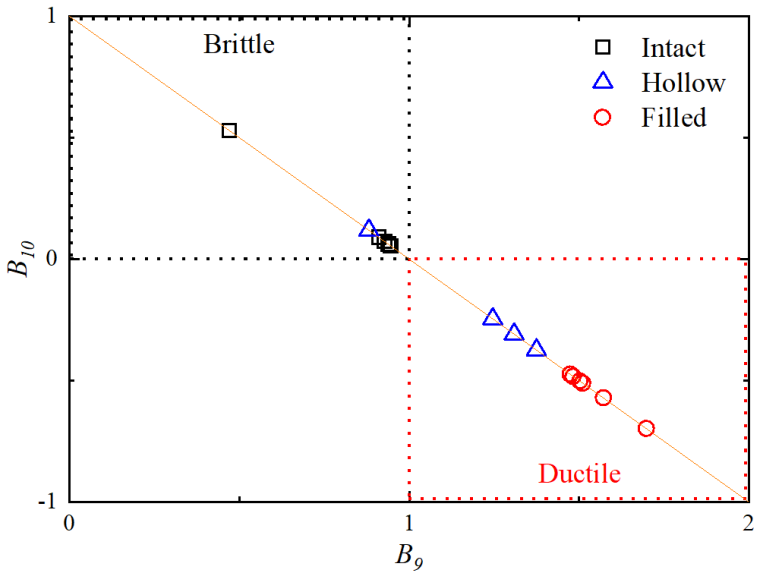

Figure 4-11 Relationship between brittleness indices B_9 and B_{10} for intact, hollow, and expansive mortar-filled granite specimens.

4.5 Summary

The experimental and numerical studies demonstrate an innovative, dynamic application of expansive mortar, other than the traditional use to split rock in a static manner. This study utilizes the dynamically amplified expansion pressure from the expansive mortar to modify the failure pattern of surrounding rock and to attenuate the stress wave from nearby explosions. The results show that tangential, radial, and randomly distributed cracks are induced in the granite, depending on the evolution of induced stresses. The effectiveness of expansion pressure is associated with the radial inertia stress under stress wave loading and possibly with the confining pressure in the field. The brittleness of surrounding rock is essentially reduced by the presence of expansive mortar, which promotes crack formation and rock deformability. This study demonstrates that the new application of expansive mortar is a possible solution to control the dynamic failure of brittle rock and the adverse impacts of underground excavation. This application may be further developed by improving the pressurization rate and capacity of expansive mortar.

Field trials will be planned to realize the implementation of the material and to optimize the utilization of expansion pressure in rock engineering.

CHAPTER 5 NUMERICAL SIMULATION OF DYNAMIC TENSIL FAILURE OF INCLUSION-BEARING ROCKS

5.1 Introduction

Inclusions are ubiquitous in rocks either naturally during rock formations or synthetically during engineering practices. As shown in Figure 5-1a, a piece of carbonatite is trapped within the fast cooling of lava, forming a xenolith (Liu et al., 2015). In rock engineering, a steel bar is installed with cement grout to reinforce fractured rock (Figure 5-1b). Under external loads, these foreign materials may exhibit different mechanical behaviors from country rocks and modify the failure pattern of rocks. The dynamic failure of surrounding granite can be facilitated by the amplified pressure from an expansive inclusion under P-wave loading (Wang et al., 2022). The cracking behaviors of gypsum specimens are related to the size, shape, stiffness, and strength of a single inclusion and additionally to the relative position of double inclusions under static uniaxial compression (Janeiro and Einstein, 2010). The dynamic tensile failure of surrounding granite remains little known but is important to provide a comprehensive understanding of rock failure influenced by the existence of embedded inclusions under static and dynamic loads.

Brazilian tension tests are commonly applied to study the tensile failure of rock discs due to the convenient specimen preparation and simple test setup (ISRM, 1978). For the dynamic tension tests using a split Hopkinson pressure bar (SHPB) system (Xia and Yao, 2015; Zhao and Gary, 1996), the test setup is modified to guarantee crack initiation from the center of the disc, such as adding thin steel rods and using curved loading jaws (Li and Wong, 2013). A flattened Brazilian specimen with a loading angle ranging from 10° to 15° can also ensure rock breakage from the center (Wang et al., 2009). However, these tension tests are not suitable to study the dynamic tensile failure of inclusion-bearing rocks, because it is challenging to control the geometrical and mechanical properties of embedded inclusions in the laboratory. Hence, numerical modelling is adopted to

simulate inclusions with various properties and to examine their influences on the dynamic tensile failure of surrounding rock. Many numerical models have been used to simulate rock failure, such as finite element model to study stress concentration related to the particle size effect (Yu et al., 2018), discrete element model to mimic crack initiation, propagation, and coalescence (Zhao et al., 2018; Li et al., 2022), and discontinuous deformation model to simulate rock fragmentation process under dynamic loading (Jiao et al., 2012). Most of these models focus on the tensile failure of intact and cracked Brazilian specimens. Recent studies on the tensile failure of Brazilian specimens with single and multiple holes demonstrate that the critical area resulted from these holes may promote the tensile failure of surrounding rocks (Bai et al., 2016) and the change of failure patterns from symmetrical under static loading to asymmetrical under dynamic loading (Li et al., 2018). The thermal effect on static and dynamic tensile behaviors of rocks have attracted a wide range of attentions. The temperature-dependent rock tensile strength plays a vital role in assessing the stimulated fracture networks in geothermal energy exploitation (Kumari et al., 2019). The performances of coal gasification and coal-bed methane mining depend highly on the dynamic tensile strength of coal materials (Li et al., 2017). Concern to protect the ancient rock cavern regarding the roof collapse due to vibration and fire accident is closely related to the dynamic tensile strength of rocks (Yao et al., 2016). Additionally, the rock and inclusion materials may have different mechanical responses to temperature change. The dynamic tensile failure of heated granite is strongly affected by thermal shock (Saksala and Ibrahimbegovic, 2020), and bolts and grouts also transfer heat to promote rock failure during tunnel fires (Wasantha et al., 2021). However, there is a still lack of knowledge related to the dynamic tensile response of inclusion-bearing rocks under a high temperature condition. Therefore, building a coupled mechanical-thermal model is essential to understand the dynamic tensile failure of inclusion-bearing rocks.

This study aims to systematically investigate the dynamic tensile failure of inclusion-bearing rock specimens, particularly considering the influences of strength ratio, loading

rate, and treatment temperature. The strength ratio is defined as the inclusion tensile strength divided by the rock tensile strength. A two-dimensional particle flow code (PFC) model is first introduced, including a SHPB system and a rock specimen containing a circular inclusion, and subsequently validated using the static and dynamic tension test results of intact sandstone specimens. The PFC model is then applied to simulate the tensile strengths and failure patterns of inclusion-bearing specimens. This model is also used to study the influences of strength ratio, loading rate, and treatment temperature on the normalized total crack density and the percentages of crack density in the rock and inclusion parts. Finally, the brittleness index as a physical indicator of inclusion-bearing specimens in response to these influences and the size effect on the tensile failure of inclusion-bearing specimens in the dynamic tension tests is discussed.

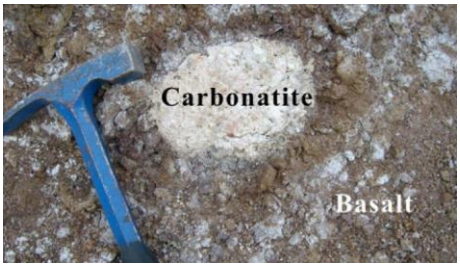

(a)

(b)

Figure 5-1 (a) Carbonatitic xenolith embedded in host basalt (Liu et al., 2015), and (b) grouted bolt for rock mass reinforcement.

5.2 Numerical modelling and validation

5.2.1 Model setup

The PFC model of a SHPB system with a diameter of 50 mm includes a striker bar (300 mm), an incident bar (1800 mm), and a transmitted bar (1500 mm) (Figure 5-2a). These bars are composed of 5248, 26310, and 31572 rigid particles with radii ranging from 0.8 to 1.0 mm. A rock specimen sandwiched between the incident and transmitted bars has a diameter of 87 mm and contains a circular inclusion with a diameter of 32 mm (Figure 5-2b). The rock and inclusion parts have 5628 and 36703 rigid particles, respectively, with radii ranging from 0.18 to 0.23 mm. Two layers of refined particles with 0.25 mm radius are inserted at the interfaces between the bars and the specimen to promote the uniform stress distribution (Duan et al., 2019a). For the strike, incident, and transmitted bars, the parallel bonds between the rigid particles have infinite tensile and shear strengths. The parallel bonds are used to evaluate tensile strength of the inclusion part rock parts (Duan et al., 2019b) and the thermal conduction between these particles (Zhao, 2015). The transient heat conduction in the DEM model is represented as a network of heat reservoirs (i.e., particles) and thermal contacts (i.e., thermal pipes). Thermal expansion coefficients are assigned separately for three types of main minerals, e.g., 24.3 $\times$ 10^{-6} K^{-1}(quartz), 8.7 $\times$ 10^{-6} K^{-1} (feldspar), and 3.0 $\times$ 10^{-6} K^{-1} (mica) (Ahrens, 1995). The specific heat and thermal conductivity are set as 1015 J kg^{-1} °C^{-1} and 3.5 W m^{-1} °C^{-1}. The mimic temperature increment is 2 °C / cycle to avoid thermal shock. Table 5-1 shows the entire numerical program in this study.

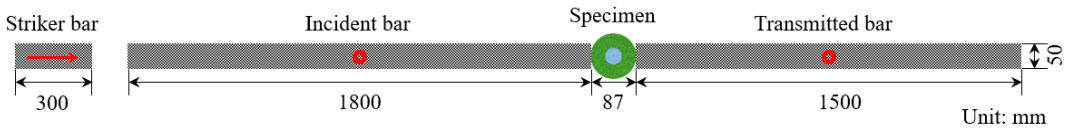

(a)

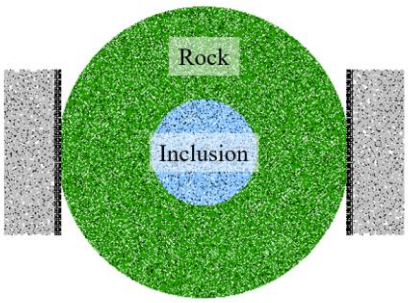

(b)

Figure 5-2 PFC modelling of (a) SHPB system with (b) inclusion-bearing rock specimen.

The static and dynamic tensile tests on flattened Brazilian specimens made of Neijiang sandstone are used to calibrate the numerical model (Pei et al., 2020). The macroscopic and microscopic parameters of the sandstone and steel materials are summarized in Table 5-2. The static tensile tests are performed by moving two loading plates on the flattened sides towards each other at a constant velocity of 0.1 mm/min. During the dynamic tensile test, a half-cycle sinusoidal P-wave with a frequency of 2 kHz is imposed at the front end of the incident bar. Two measurement circles are placed at the centers of the incident and transmitted bars to record the P-wave propagating in the system.

Table 5-1 Numerical program used for PFC model set-up, microscopic parameter calibration, and numerical testing in this study.

Numerical program	Details
Model setup	SHPB and specimens
Static and dynamic mechanical microscopic parameters used in the numerical model	Young's modulus, Poisson's ratio, stiffness ratio
Thermal microscopic parameters used in the numerical model	Thermal conductivity, thermal expansion coefficient

Numerical testing of inclusion-bearing specimens	Temperatures (25, 200, 400, and 600 °C) and loading rates (100, 180, and 240 GPa/s)

Table 5-2 Macroscopic properties of sandstone and steel materials and microscopic parameters used in the numerical model.

	Sandstone	Steel
Macroscopic parameters		
Density (kg/m^3)	2320	7800
Young's modulus (GPa)	8	210
P-wave velocity (m/s)	-	5201
Poisson's ratio	0.23	-
Specific heat (J kg^{-1} °C^{-1})	1015	-
Thermal conductivity (W m^{-1} °C^{-1})	3.5	-
Rigid particles		
Radius (mm)	0.18-0.23	0.8-1.0
Density (kg/m^3)	2564	9235
Young's modulus (GPa)	8.0	128
Normal stiffness / shear stiffness	1.2	2
Friction coefficient	0.5	0.5
Parallel bonds		
Young's modulus (GPa)	8.0	128
Normal stiffness / shear stiffness	1.2	2.0
Tensile strength (MPa)	50	1*10^{100}
Shear strength (MPa)	50	1*10^{100}
Friction angle (°)	0.3	0.3

This study highlights the effects of inclusion strength, loading rate, and treatment temperature on the tensile strength and the failure pattern of an inclusion-bearing

specimen. For soft (e.g., sandy and clayey materials) to hard (e.g., steel bar and cement grout) inclusions, the ratios of inclusion strength to the rock strength are considered as 0.2, 0.8, 1.2, and 2.4. The loading rates, 100, 180, 240 GPa/s, correspond to the P-wave amplitudes, 5, 10, and 15 m/s, respectively. Both the ambient (25 °C) and extreme temperatures (e.g., 200, 400, and 600 °C) may be encountered in rock engineering (e.g., deep mining and fire hazard), and these temperature conditions are considered in this study.

5.2.2 Model validation

The numerical model is validated based on the dynamic stress equilibrium of an intact sandstone specimen as well as the comparisons between the experimental and numerical results under the static and dynamic conditions. The incident, reflected, and transmitted waves recorded by the measurement circles are shifted to the bar-specimen interfaces. The dynamic stress at the interface between the incident bar and the specimen is almost balanced by that at the interface between the specimen and the transmitted bar (Figure 5-3a). The static tensile strength slightly fluctuates at relatively low temperatures (e.g., 200 and 400 °C) and significantly drops at relatively high temperatures (e.g., 600 °C) (Figure 5-3b), which is consistent with the results of four Brazilian tension tests under static loading (Su et al., 2016). The dynamic tensile strength increases with a higher loading rate (Figure 5-3c), which agrees with the results of five Brazilian tension tests under dynamic loading (Pei et al., 2020). The comparisons between the numerical and experimental results confirm that this model is applicable to study the tensile behaviors of a sandstone specimen under different loading and thermal conditions.

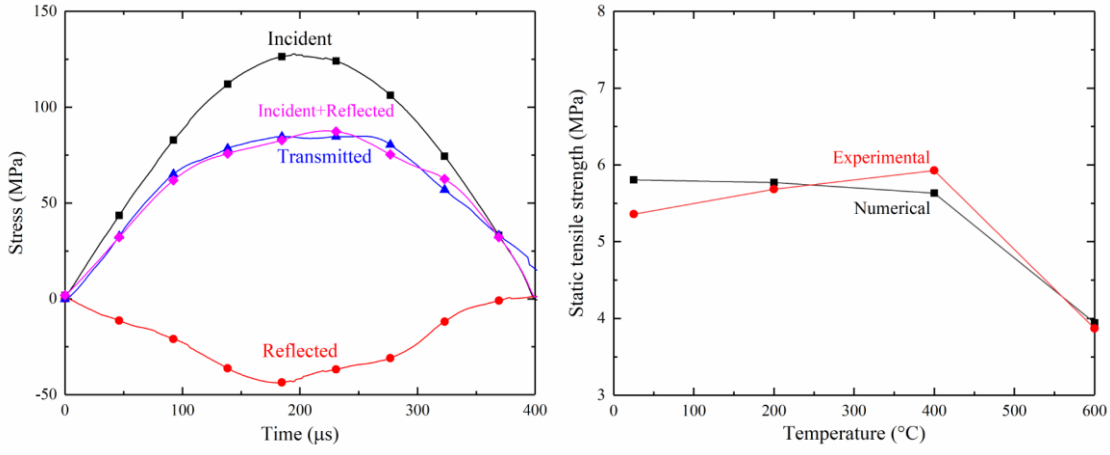

(a) (b)

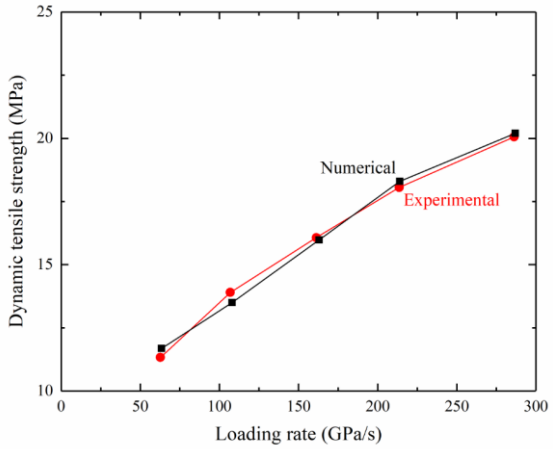

(c)

Figure 5-3 Model validation based on static and dynamic tensile tests on intact rock specimens, (a) dynamic stress equilibrium of the specimen, (b) static tensile strength evolves with varying temperatures, and (c) dynamic tensile strength evolves with varying loading rates.

To simulate the tensile behaviors of an inclusion-bearing specimen, attention should be paid to the interface between the rock and inclusion parts. A particle layer with 0.2 mm thickness is inserted between the rock and inclusion parts as suggested by Qiu et al.

(2020). Because the interface between the rock and inclusion parts should have a lower tensile strength than the rock and inclusion materials, a strength reduction ratio as the layer tensile strength divided by a larger tensile strength is defined between the rock and inclusion parts. For different strength reduction ratios, the nominal tensile strength exhibits nearly no change as the strength ratio increases (Figure 5-4). The results indicate that the tensile strength of the interface has a trivial impact on the tensile strength of an inclusion-bearing specimen. Hence, this numerical model considers a direct contact between the rock and inclusion parts.

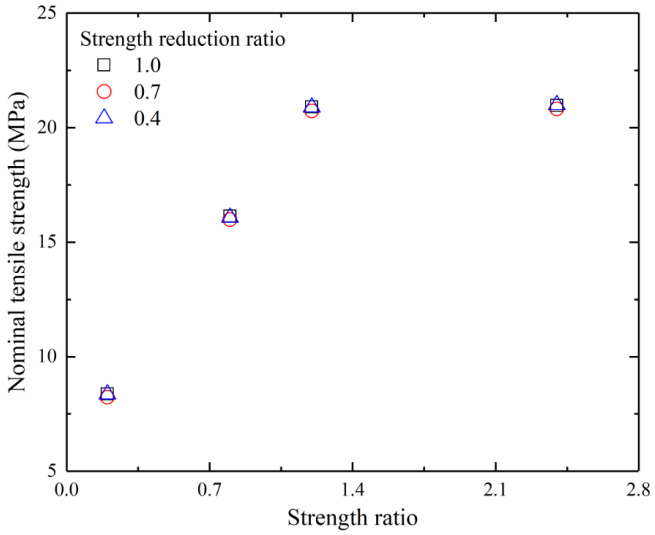

Figure 5-4 Nominal tensile strength of inclusion-bearing specimen as functions of strength reduction ratio of rock-inclusion interface and strength ratio of rock and inclusion parts.

5.3 Numerical results

As shown in Figure 5-5, the nominal tensile strength increases with a larger strength ratio when the ratio is smaller than 1 and varies slightly when the ratio exceeds 1. The nominal tensile strength evolving with the strength ratio can be explained by the failure patterns

of the inclusion-bearing specimen (Figure 5-6). The tensile cracks represented by red dots determine the failure modes of the rock and inclusion parts, while the shear cracks by blue dots exhibit a scattered distribution. For a strength ratio of 0.2, densely distributed cracks appear in the inclusion part are accompanied by well aligned cracks along and perpendicular to the loading direction in the rock part. The failure pattern of the rock part is similar to that of a hollow specimen (Li et al., 2016). The cracks along the loading direction are generated by the induced tensile stress, and the formation of the cracks perpendicular to the loading direction is attributed to the dynamic impact on split halves in the post-peak process. When the strength ratio approaches 1 (e.g., 0.8 and 1.2), the percentage of the crack density in the inclusion part significantly decreases (see red column in Figure 5-7), and the cracks in the rock and inclusion parts mostly align along the loading direction. This is expected as the rock and inclusion parts have similar tensile strengths, and the tensile stresses are induced perpendicular to the loading direction. When the inclusion part is much stronger than the rock part (e.g., 2.4), most of the cracks exist in the rock part. In these cases, the nominal tensile strength is mainly associated with the tensile strength of the rock part and less dependent on the strength ratio. That is why the nominal tensile strength shows a minor variation when the strength ratio is larger than 1.

Many studies show that the tensile strength of rocks increases with a higher loading rate due to the inertia effect (Zhao and Li, 2000; Wu et al., 2015). The positive correlation between the nominal tensile strength and loading rate can also be observed in Figure 5-5. Particularly, for a smaller strength ratio (e.g., 0.2), the nominal tensile strength is dominated by loading rate, and the temperature effect is minor. When the strength ratio approaches and even exceeds 1, the loading rate and the treatment temperature concurrently affect the nominal tensile strength. A higher loading rate and a lower treatment temperature generally result in a larger nominal tensile strength. With increasing strength ratio, the influence of treatment temperature on the nominal tensile strength becomes more important. For the strength ratios of 1.2 and 2.4, the nominal

tensile strengths at 400 and 600 °C treatment temperatures are lower than those at 25 and 200 °C treatment temperatures and less dependent on loading rate.

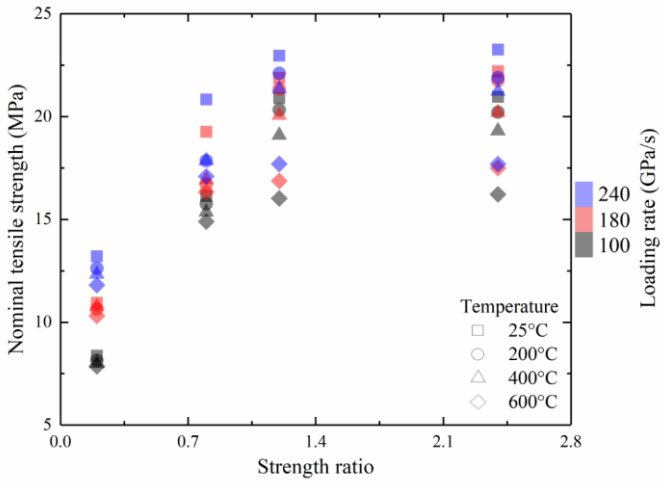

Figure 5-5 Nominal tensile strength of inclusion-bearing rock specimen as a function of strength ratio at different temperatures and loading rates.

The failure modes of inclusion-bearing specimens can also be viewed through normalized total crack density, which quantifies the amount and the distribution of induced cracks shown in Figure 5-6. The blue and red columns represent the percentages of crack density in the rock and inclusion parts, respectively (Figure 5-7). The normalized total crack density is the sum of crack densities in the rock and inclusion parts normalized by that of the case at 25 °C temperature and 100 GPa/s loading rate. For a given loading rate, the normalized total crack density for a larger strength ratio shows an obvious increase at a higher treatment temperature, while that for a smaller strength ratio fluctuates around the initial value (Figure 5-8). The negative correlation between the tensile strength and treatment temperature is well addressed in other studies due to the formation of thermally induced cracks (Zhao et al., 2018; Wang et al., 2022). The results reveal that an embedded inclusion with a higher tensile strength than surrounding rocks promotes the development of mechanically induced cracks in rocks.

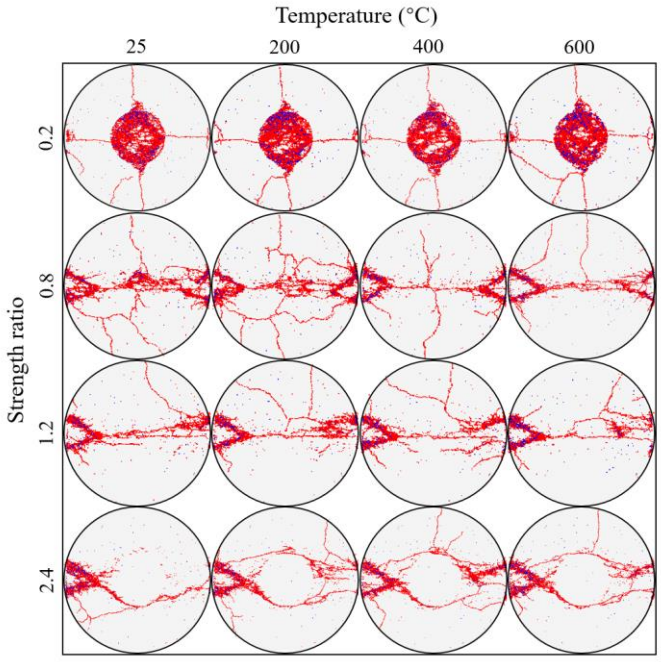

Figure 5-6 Failure patterns of inclusion-bearing rock specimens with various strength ratios at different temperatures. The loading direction is along the horizontal axis of the specimen, and the loading rate is 100 GPa/s. The red and blue dots represent tensile and shear cracks, respectively.

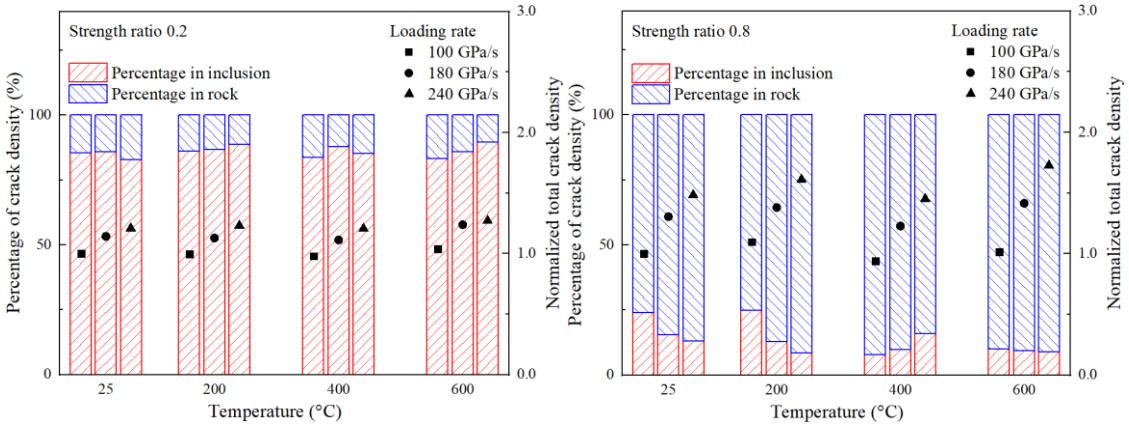

(a) (b)

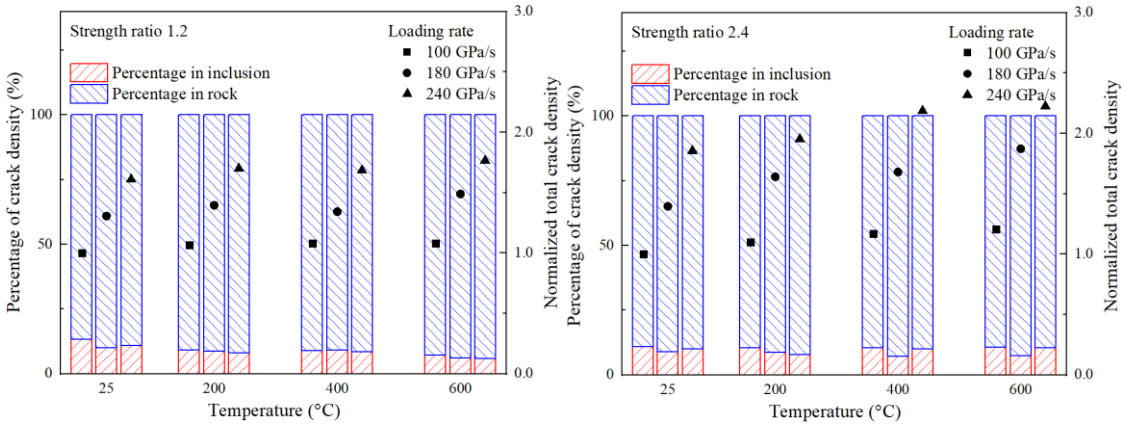

(c) (d)

Figure 5-7 Normalized total crack density and percentages of crack density in rock and inclusion parts under different combinations of strength ratio, treatment temperature, and loading rate.

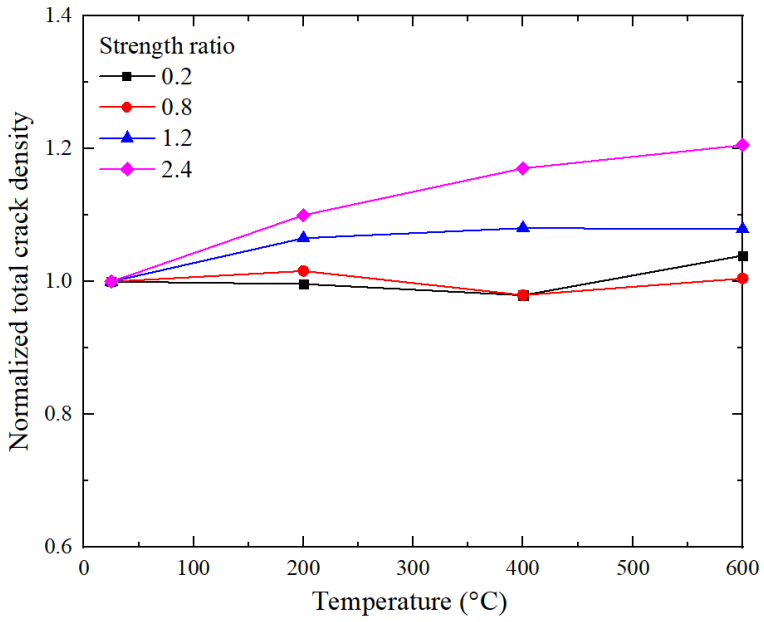

Figure 5-8 Normalized total crack density as functions of strength ratio and treatment temperature at a loading rate of 100 GPa/s.

5.4 Discussion

The results demonstrate that the nominal tensile strength of inclusion-bearing rock specimens evolves with varying strength ratios, loading rates, and treatment temperatures. The changes in specimen strength and failure pattern indicate that the embedded inclusion essentially modifies the brittleness of inclusion-bearing specimens. The brittleness index B_9 is adopted to quantify the evolution of specimen brittleness under dynamic tensile conditions (Tarasov and Stacey, 2017). Elastic modulus (E) and post-peak modulus (M) are obtained from the stress-strain curve as illustrated in Figure 5-9a.

The results of brittleness index exhibit that, when the inclusion tensile strength is smaller than the rock tensile strength, strength ratio is the most influential factor on specimen brittleness (Figures 5-9b and 5-9c). Loading rate is less influential and inversely proportional to a decrease in brittleness index. This is because the number of induced cracks increases with a higher loading rate, as indicated by the normalized total crack density in Figure 5-7, resulting in a less brittle specimen. However, the brittleness index is independent of treatment temperature, as less induced cracks distribute in the rock part and insignificantly affect the stress and strain measurements. When the inclusion tensile strength approaches and even exceeds the rock tensile strength, the loading rate effect remains important, and the temperature effect shows a minor influence. However, the strength ratio effect becomes negligible, because induced cracks mostly appear in the rock part and the brittleness index is mainly related to rock brittleness. The results reveal that the tensile strength of the inclusion part in relative to that of the rock part determines the numbers of induced cracks in different parts, which essentially affects the evolution of specimen brittleness and controls the tensile strength of an inclusion-bearing specimen.

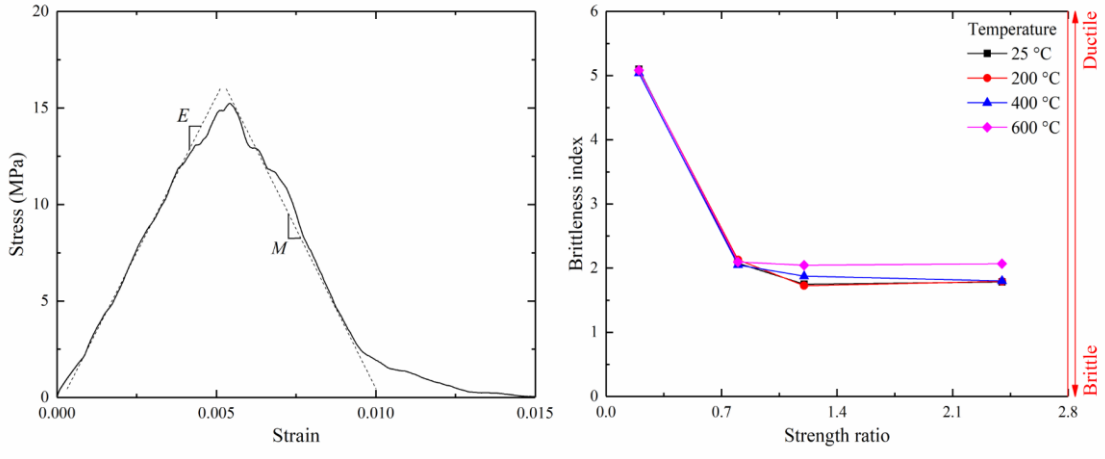

(a) (b)

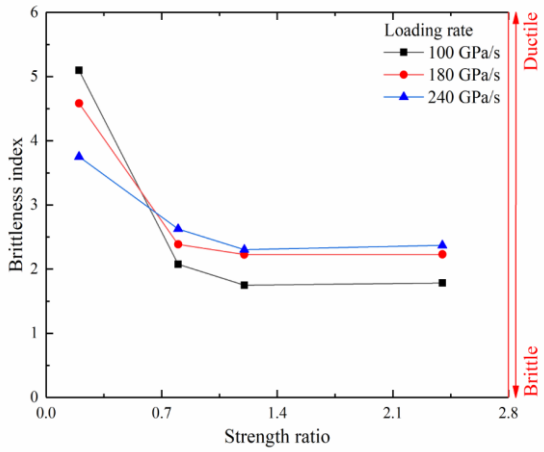

(c)

Figure 5-9 Brittleness index of inclusion-bearing rock specimen, (a) determination of elastic modulus (E) and post-peak modulus (M), (b) brittleness index as functions of strength ratio and treatment temperature at a loading rate of 100 GPa/s, and (c) brittleness index as functions of strength ratio and loading rate at 25 °C treatment temperature.

The brittleness index of rocks is related not only to loading rate but also specimen size (Zou et al., 2021). The size effect on the brittleness index of an inclusion-bearing specimen is thus investigated. As a specimen diameter larger than 88 mm is unfavorable

to achieve dynamic stress equilibrium, a smaller specimen and inclusion diameters were considered. Figure 5-10a shows that reductions in specimen and inclusion diameters mainly influence the brittleness index when the inclusion tensile strength is smaller than the rock tensile strength. A similar trend can be observed when the specimen diameter is fixed, and the inclusion diameter decreases (Figure 5-10b). The results exhibit that the inclusion diameter strongly influences the evolution of brittleness index, while the specimen diameter plays an insignificant role. This is because induced cracks mostly appear in the inclusion part for the case of the strength ratio less than 1. When the inclusion tensile strength is not less than the rock tensile strength, the brittleness index is independently of inclusion diameter as most of the cracks are induced in the rock part. Therefore, the results indicate that low strength, large size inclusions promote a reduction in brittleness index and accelerate the degradation of an inclusion-bearing specimen. However, the size effect analysis is incomplete as the specimen size is limited by the requirement of dynamic stress equilibrium of the specimen in the SHPB setup. Field investigation is thus needed for a comprehensive analysis.

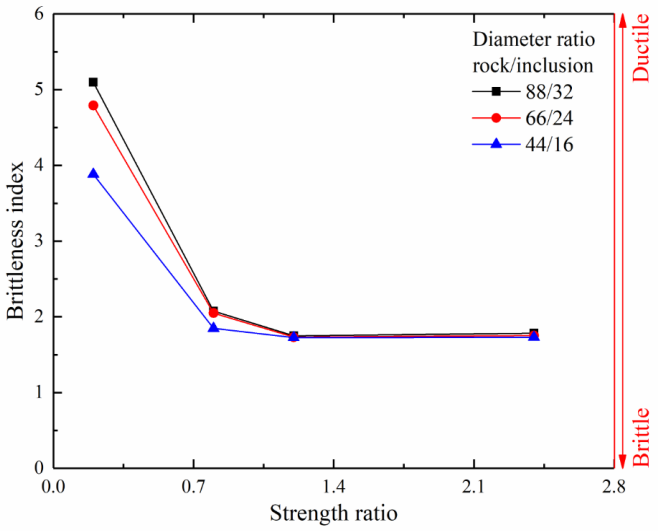

(a)

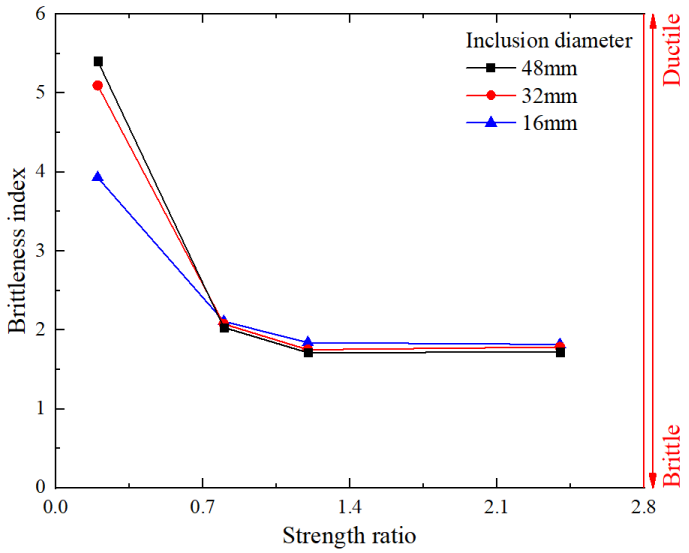

(b)

Figure 5-10 Size effect on brittleness index of inclusion-bearing rock specimen as a function of (a) ratio of rock diameter to inclusion diameter, and (b) inclusion diameter with a specimen diameter of 88 mm. In this case, the temperature and the loading rate are 25 ºC and 100 GPa/s, respectively.

5.5 Summary

This study conducts a series of numerical simulations on the dynamic tensile failure of inclusion-bearing rock specimens. The numerical model is validated using the static and dynamic tensile strengths of intact sandstone specimens. The influences of strength ratio, loading rate, and treatment temperature are examined on the nominal tensile strength of inclusion-bearing specimens. The results show that the nominal tensile strength positively correlates with strength ratio, which plays a more significant role than loading rate and treatment temperature, when the strength ratio is smaller than 1. When the strength ratio approaches and even exceeds 1, loading rate and treatment temperature jointly influence the nominal tensile strength, but the strength ratio effect is negligible. The evolution of nominal tensile strength is associated with the numbers of induced cracks in the rock and inclusion parts and can be explained by a change in brittleness

index. This study provides a fundamental reference for the dynamic tensile responses of rock materials containing natural and synthetic inclusions. Under-standing the dynamic behaviors of inclusion-bearing rocks could help predict rock failure and mitigate induced geohazards.

CHAPTER 6 ABRASIVITY MEASUREMENT OF BRITTLE ROCK AFTER THERMAL TREATMENT

6.1 Introduction

Abrasivity characteristics of brittle rock are essential to evaluate the cutting-tool wear and the rock-breaking efficiency during underground excavation and geo-energy extraction. Besides rock hardness, thermal treatment has been recognized as a key factor influencing rock abrasivity (Ji et al., 2021; Rossi et al., 2020b). For instance, the non-contact flame-jet spallation technique and flame-assisted rotary drilling can improve the drilling performance by thermally weakening the rock prior to the rock removal (Rossi et al., 2018 and 2020a). However, high temperatures may not be continuously maintained during rock breakage operations. Temperature reduction can occur due to fluid circulation during borehole drilling, which results in crack generation in surrounding rock (Zhang et al., 2018; Kant et al., 2017). Particularly, the thermal shock due to rapid cooling further promotes crack growth and rock degradation (Li et al., 2020; Han et al., 2019) and potentially influences the abrasivity measurement of thermally treated rock.

The determination of rock abrasivity is commonly based on Cerchar abrasivity index (CAI) test (Alber et al., 2014) to assess the tool wear and performance in tunnelling and drilling applications. Our understanding of rock abrasivity has been remarkably improved according to various CAI tests. The CAI value is strongly affected by rock minerology (Yaralı et al., 2008) and internal structure (Alber, 2008) but independent of scratching speed (Rostami et al. 2014). The CAI value is also correlated to the compressive and shear strengths of tested rocks (Deliormanlı 2012; Er and Tuğrul, 2016). The stylus and rock interaction is estimated based on the rock removal volume and the stylus wear volume (Zhang and Konietzky, 2020), and the efficiency of rock scratching is reflected by the stretching specific energy (Zhang et al., 2020). Machine learning approaches can be applied to predict the CAI value according to the rock mechanical

properties, such as P-wave velocity, uniaxial compressive strength, and Young's modulus (Tripathy et al., 2015). As suggested by the test standard of the International Society for Rock Mechanics and Rock Engineering (ISRM) (Alber et al., 2014), the CAI measurement relies on the profile of worn stylus, which should be relatively flat and symmetrical about the longitudinal axis of the stylus, without serious damage on the sides of the stylus cone. However, thermal treatment may promote the indentation of the stylus into highly cracked rock. In other words, the amplified interaction between the worn stylus and the cracked rock possibly causes the side wear and subsequently modifies the profile of wear flat. In this case, the influence of thermal treatment on the CAI measurement remains unclear. The contribution of the side wear, which can be even significant after rapid cooling, should be considered in the CAI measurement. Therefore, the CAI measurement for the case with notable stylus indentation should be re-examined to understand the stylus and rock interaction and the measurement error of CAI value under different heating and cooling conditions.

This study performs a series of CAI tests on granite specimens after the thermal treatment, which first heats the specimens to 200, 400, and 600 °C, and then cools them down in air and water to simulate the slow and rapid cooling, respectively. It is expected that the CAI value varies with different combinations of heating temperature and cooling rate, and thus investigate the effect of stylus indentation on the CAI measurement. The physical and mechanical properties of the specimens before and after the thermal treatment are also examined, including P-wave velocity, AE, material hardness, indentation stress, and brittleness index. These properties provide insights to explain the stylus and rock interaction. Finally, it is suggested that the improvement of the CAI measurement for the case with notable stylus indentation and discuss the physical mechanism underlying the stylus indentation in the highly cracked rock.

6.2 Experimental method

Bukit Timah granite core with a diameter of 63 mm in central Singapore was used as the rock material. The medium-grained granite is composed of 62% feldspar, 32% quartz, 5% biotite, and 1% hornblende. Eighteen specimens with a thickness of 12 mm were cut from the granite core. The specimen ends were polished using P280 grit sandpaper with a particle size of 52.2 μm. Figure 6-1 shows the experimental facilities, including the Pundit ultrasonic device, the Nabertherm chamber furnace, the National Instruments data acquisition system, the CAI test setup, and the Nikon polarizing microscope. The ultrasonic device was used to measure the P-wave velocities of each specimen before and after the thermal treatment (Figure 6-1b). The specimen was heated to a target temperature at a rate of 5°C/min in the chamber furnace (Figure 6-1c), and the temperature was maintained for 1 hour. The data acquisition system recorded the temperature variation at a sampling rate of 10 Hz. The measurement of wear flat on the stylus tip was performed using the optical microscope with an accuracy of 0.01 mm (Figure 6-1f)

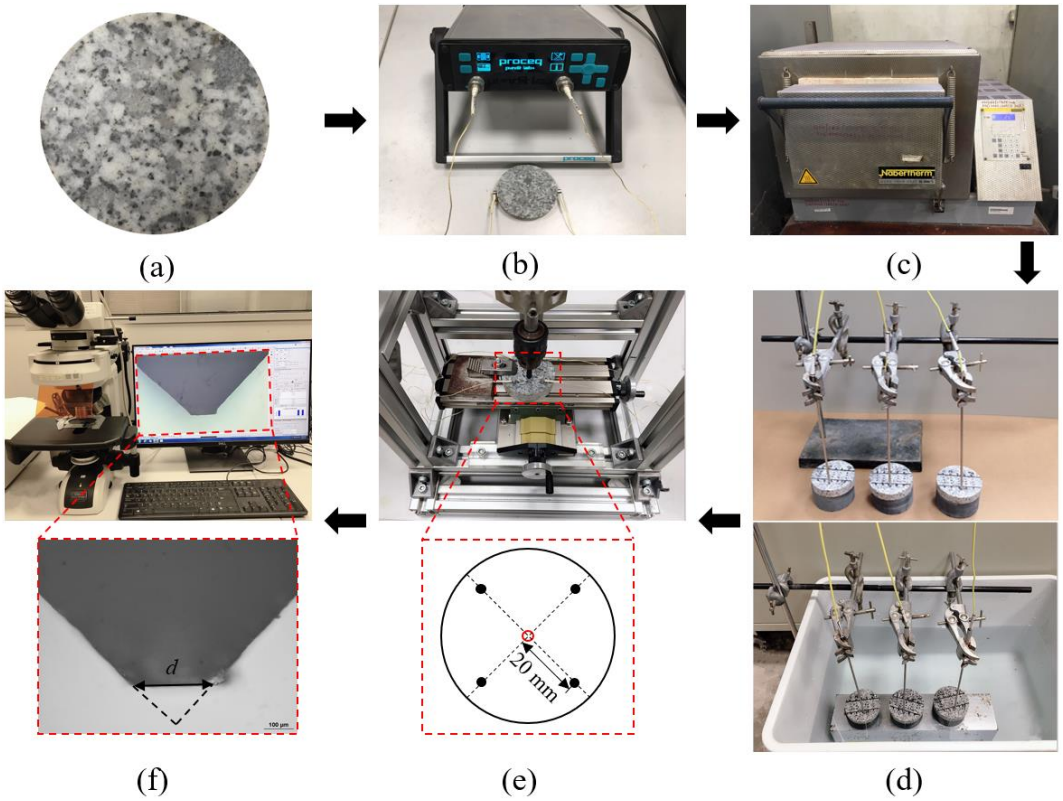

Figure 6-1 Schematic view of experimental procedure, (a) granite specimen, (b) measurement of P-wave velocity, (c) heating treatment, (d) slow (upper) and rapid (lower) cooling treatment, (e) CAI test setup and arrangement of AE sensors (black dots), and (f) measurement of wear flat.

The CAI test setup mainly consists of a steel stylus, a sample stand, a stylus chuck, and a lever arm (Figure 6-1e) (Ji et al., 2021). The steel stylus has a HRC of 54 and a conical angle of 90°. The specimen was clamped on the sample stand. The stylus fixed on the stylus chuck was perpendicular to the specimen and then lowered down onto the specimen surface. A normal load of 70 N was applied on the stylus through the lever arm. During the CAI tests, the scratching speed was controlled at 1-1.5 mm/s, and the scratching distance was 20 mm. The wear flat on the stylus tip was measured after every 5 mm scratching distance, and the mean wear flat (d) was obtained based on four side views of wear flat at 90º rotation. The CAI value was thus calculated as $10 \times d$. The

SAMOS AE system was used with four piezoelectric sensors glued on the specimen, 20 mm distance from the center of the specimen, to monitor the granite damage. Both the preamplifier gain, and the amplitude threshold were 40 dB, and the sampling rate was 1 MHz.

Eighteen specimens were equally divided into three groups, each with six specimens, and heated to 200, 400, and 600 °C. After that, half of the specimens in each group were immediately moved into a 20 L water bath at 17 °C to simulate rapid cooling (Figure 6-1d), and the other half were naturally cooled down in air outside the furnace at ambient temperature (25 °C). The cooling process was monitored by a thermal couple, which was installed at a central hole with 3 mm diameter and 5 mm deep on the specimen surface. The CAI tests were carried out at room temperature.

6.3 Experimental results

The slow and rapid cooling can be characterized by the cooling rate, which is correlated to the intensity of thermal cracking (Shao et al., 2014; Zhang et al., 2018) and used to explain the CAI test results. The cooling rate is determined as the slope of the linear temperature profile (Figure 6-2). A larger cooling rate can be achieved when the specimen is immersed in water after the treatment with a higher heating temperature, while the cooling rate is smaller when the specimen cools in air and decreases with a lower heating temperature. The duration of rapid cooling is much shorter than that of the slow cooling. The rate of rapid cooling is about two orders of magnitude larger than the rate of slow cooling, and both the rates exhibit similar reduction trends with increasing heating temperature (Figure 6-3).

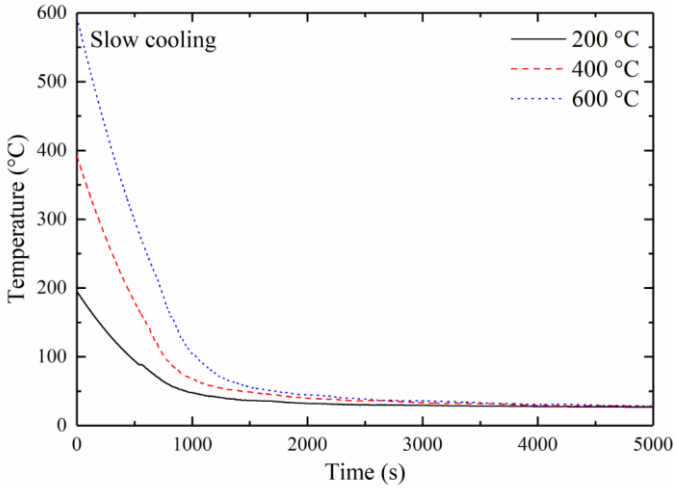

(a)

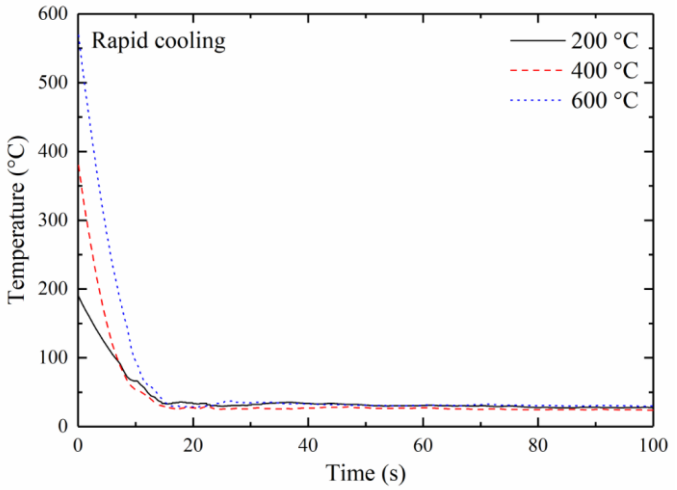

(b)

Figure 6-2 Variation in specimen temperature during (a) slow and (b) rapid cooling.

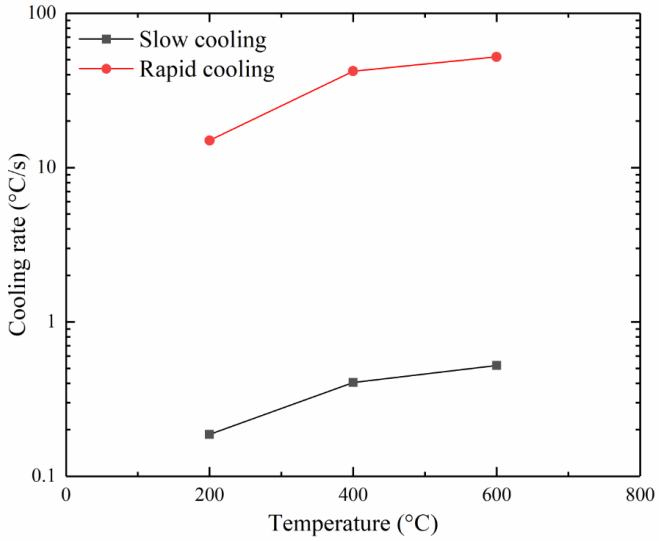

Figure 6-3 Variation in cooling rate during slow and rapid cooling.

The results of each CAI test are shown with four CAI values at 5, 10, 15, and 20 mm scratching distance (Figure 6-4). The CAI value generally increases with a larger scratching distance and drastically jumps in the first 5 mm scratching distance. The abrasive wear of the stylus tip mainly occurs when the unscratched tip interacts with the intact granite, while the worn tip encounters less damage in the cracked granite. The stylus wear mainly occurring within the first few scratching distance is also reported by Rossi et al. (2020). For a given scratching distance, the CAI value after the slow cooling is larger than that after the rapid cooling, because thermal cracking can be promoted by the rapid cooling (Li et al., 2020). The interaction between the stylus tip and cracked granite thus leads to a larger CAI value (Ji et al., 2021). For rapid cooling, thermal cracking plays an essential role and causes an increase in CAI value after the treatment with a higher heating temperature. However, both thermal cracking and thermal hardening compete during the slow cooling, and the long-term cooling process may enhance the material cohesion (Zhang et al., 2018). This explains why the CAI value after the treatment with 200 ºC heating temperature is larger than that after the treatment with 400 ºC heating temperature (Figure 6-4a). The CAI value may vary depending on

the degree of indentation at lower temperatures (i.e., 200 and 400 ºC). For instance, the scratched-off biotite residuals may compensate the wear of stylus tip when scratches on the surface of hard minerals (e.g., quartz and feldspar), resulting in a reduction in CAI value (Ji et al., 2021).

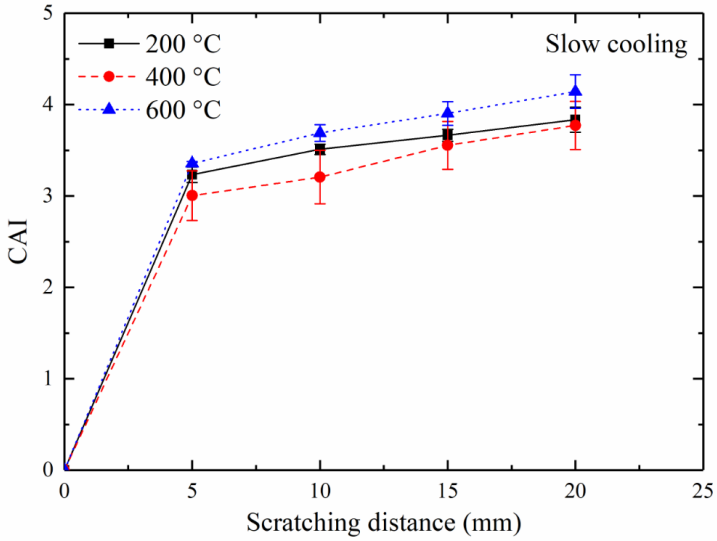

(a)

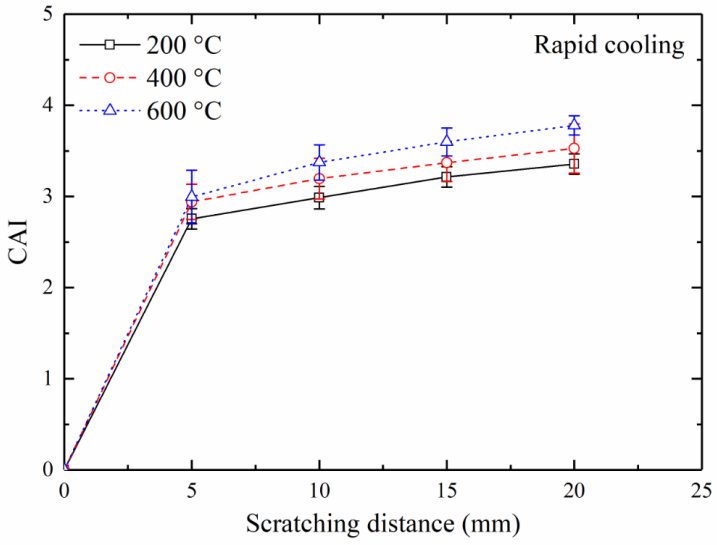

(b)

Figure 6-4 CAI as a function of scratching distance during (a) slow and (b) rapid cooling after granite specimen is treated at 200, 400, and 600 ºC.

The results of CAI tests can be understood based on the measurement of P-wave velocity, which reflects the amount of thermally induced cracks in the granite (Figure 6-5). The P-wave velocities obtained after the thermal treatment with different heating and cooling processes and the CAI values measured after 20 mm scratching distance are normalized by the P-wave velocity and the CAI value at ambient temperature, respectively. The normalized P-wave velocity decreases after the treatment with a higher heating temperature. This observation is consistent with the SEM images on the treated granite, in which the amount of thermally induced cracks increases with a higher heating temperature (Wu et al., 2019; Zhang et al., 2018). For the slow cooling, the normalized CAI value after the treatment with 200 ºC heating temperature is nearly the same as that at ambient temperature, owing to a negligible amount of thermally induced cracks as indicated by a minor variation in normalized P-wave velocity. The normalized CAI value after the treatment with 400 ºC heating temperature becomes smaller because a marked reduction in normalized P-wave velocity indicates the notable formation of thermally induced cracks. After the treatment with 600 ºC heating temperature, the normalized CAI value increases and even exceeds the initial value, which is attributed to the indentation of the stylus and the amplified interaction between the worn stylus and the cracked granite (Ji et al., 2021). Additionally, the rapid cooling promotes the formation of thermally induced cracks. Both the normalized P-wave velocity and the normalized CAI value thus reduce after the treatment with 200 ºC heating temperature. Subsequently, the normalized P-wave velocity continuously decreases as the treatment with a higher heating temperature further promotes the formation of thermally induced cracks. However, the normalized CAI value after the treatment with 400 ºC heating temperature increases due to the early occurrence of stylus indentation in the cracked granite, followed by a further increase in the normalized CAI value after the treatment with 600 ºC heating temperature.

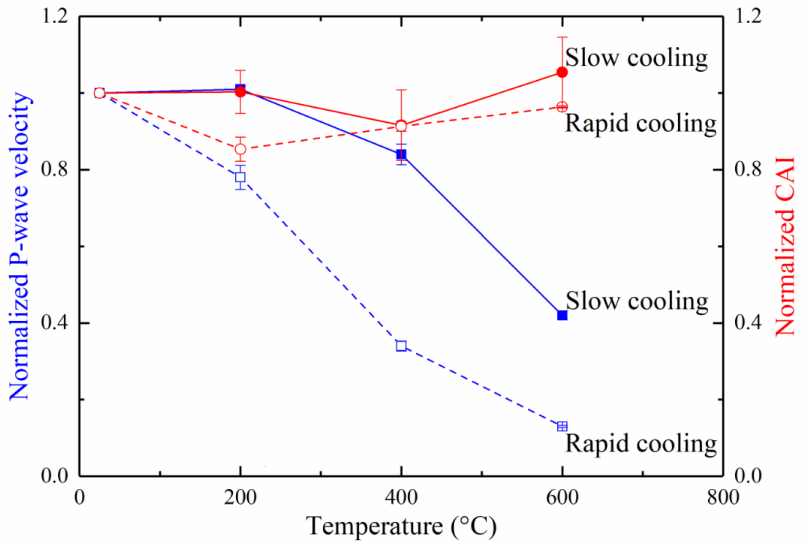

Figure 6-5 Normalized P-wave velocity and normalized CAI after granite specimen is treated at 200, 400, and 600 ºC in comparison to those at ambient temperature (25 ºC).

The AE monitoring results demonstrate the stylus and granite interaction and provide the evidence to support the explanation of stylus indentation. The P-wave velocity of the specimen after the rapid cooling lower than that after the slow cooling indicates more cracks induced by the rapid cooling. Hence, the cumulative AE count from the specimen after the rapid cooling is larger than that from the specimen after the slow cooling due to the enhanced interaction between the indented stylus and the cracked granite (Figure 6-6). The jump of cumulative AE count is accompanied by the occurrence of AE energy release. Both the amplitude and the frequency of AE energy release increase after the treatment with a higher heating temperature. Hence, the stylus and granite interaction becomes more violent due to the treatment with a higher heating temperature and rapid cooling. After the treatment with a lower heating temperature and slow cooling, the specimen remains intact as indicated by the normalized P-wave velocity. The soft minerals (e.g., biotite) is scratched off, and the hard minerals (e.g., quartz and feldspar) experience negligible damage during the CAI tests (Ji et al., 2021). However, the

indentation depth of the stylus can be increased in the cracked granite after the treatment with a higher heating temperature and rapid cooling. The stylus can more frequently interact with the hard minerals below the specimen surface, which are confined by neighboring minerals and possibly release high AE energy (Perez et al., 2015).

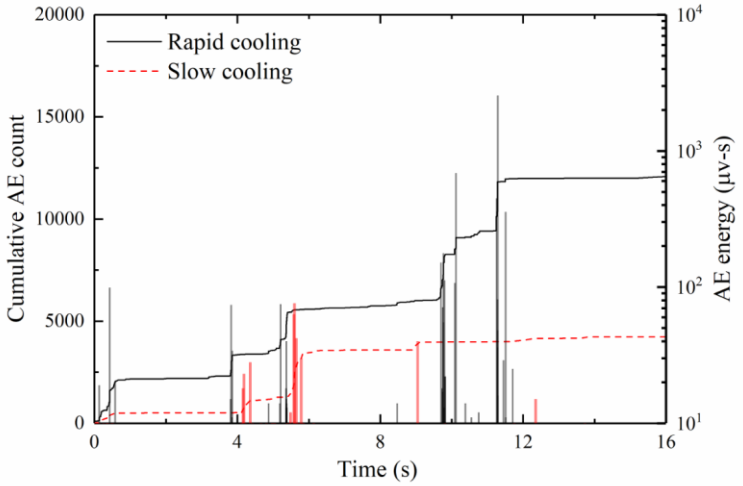

(a)

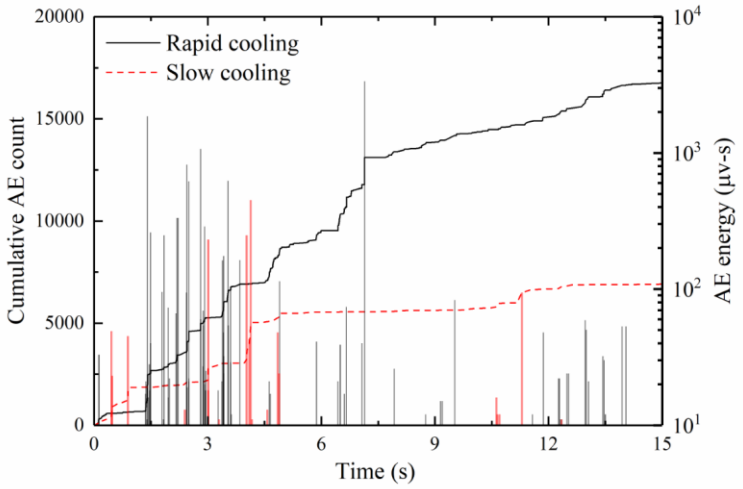

(b)

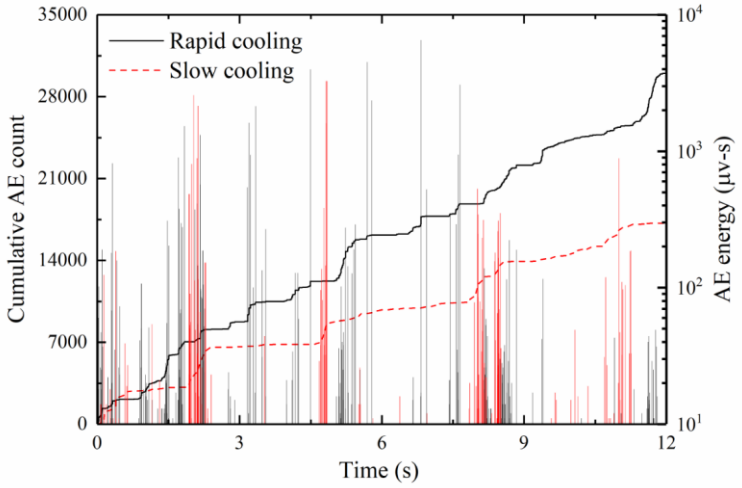

(c)

Figure 6-6 Evolution of cumulative AE count and AE energy during CAI tests on granite specimen after the treatment with (a) 200, (b) 400, and (c) 600 °C heating temperature.

6.4 Discussion

The results highlight the important of understanding the interaction between the indented stylus and the cracked rock to reveal the influences of thermal treatment on the abrasivity measurement of Bukit Timah granite. Figure 6-5 exhibits the impact of thermal treatment on the P-wave velocity and the effect of cooling rate on the CAI value but does not directly reflect the stylus and rock interaction. The Cerchar abrasion ratio (CAR), defined as the ratio of the rock removal volume (V_r) to the stylus wear volume (V_s), reveals the stylus and rock interaction, in terms of volume variation (Zhang and Konietzky, 2020):

$$CAR = \log_{10}\left(\frac{V_r}{V_s}\right) \tag{6-1}$$

where V_s can be estimated based on the wear flat (d):

$$V_s = \frac{1}{3}\pi\left(\frac{d}{2}\right)^2 h \tag{6-2}$$

where h is the height reduction on the stylus tip and $h = d/2$ for 90° tip angle.

The rock removal volume can be assessed based on the penetration depth of the stylus (Rossi et al., 2020a). However, the penetration depth may not be accurately estimated in this case, because rock fragments may exist before the scratch and fill in the trench after the scratch. According to the empirical relation between the CAR and CAI values for a smooth surface (Zhang and Konietzky, 2020), CAR = –0.628 CAI + 4.463, the CAR value is also related to the wear flat, as the CAI value is determined as $10 \times d$. Therefore, the wear flat is a key parameter to evaluate the stylus and rock interaction.

In the CAI tests, the wear flat is measured at the stylus tip, and the sides of stylus cone should be intact. For a non-standard worn profile (e.g., the side wear is non-symmetrical), the measurement is invalid (Alber et al., 2014). For the CAI tests on the thermally treated rock, especially after the rapid cooling, the occurrence of stylus indentation in the highly cracked rock is likely unavoidable, and the side wear may unexpectedly change the geometry of wear flat. In this case, the measurement of wear flat should not rely solely on the stylus tip. As shown in Figure 6-7a, the stylus tip is obtained after the scratch across the specimen after the treatment with 600 ºC heating temperature. The stylus indentation not only promotes the side wear but also causes the steel stretching beyond the wear flat. To reasonably measured the wear flat, one suggestion is to draw two straight lines from the unworn sides. The two lines can reproduce the profile of intact stylus and assist the determination of the lateral extent of wear flat by excluding the influences of side wear and steel stretching.

The ISRM test standard suggests that the stylus should be moved across the specimen for 10 mm scratching distance to evaluate the CAI value (Alber et al., 2014). For the CAI tests on the thermally treated rock, the applicability of 10 mm scratching distance is further examined, considering the influences of side wear and steel stretching on the CAI

measurement. Figure 6-7 illustrates the evolution of stylus tip after the scratch for different scratching distances. When the scratching distance approaches 10 mm, the influences of side wear and steel stretching on the measurement of wear flat become notable (Figure 6-7b). When the scratching distance exceeds 10 mm, the wear flat cannot be observed, and the results are considered as invalid (Figures 6-7c and 6-7d). The CAI measurement error is additionally calculated (e_{CAI}):

$$e_{CAI} = \frac{CAI_x - CAI_5}{CAI_5} \tag{6-3}$$

where CAI_x is the CAI value measured after x mm scratching distance, and CAI_5 is the CAI value measured after 5 mm scratching distance

The CAI measurement errors are calculated based on the CAI values in Figure 6-4 and indicate that the CAI measurement error after slow cooling is slightly lower than that after rapid cooling (Figure 6-8). More importantly, the CAI measurement errors for 10 mm scratching distance on the specimens after the treatment with different heating temperatures and slow cooling are below 10%. Similar measurement errors can be found from the specimens after the treatment with 200 and 400 ºC heating temperatures and rapid cooling, and that from the specimen after the treatment with 600 ºC heating temperature and rapid cooling is slightly higher but remains close to 10%. Therefore, based on the observation of worn stylus and the calculation of CAI measurement error, 10 mm scratching distance suggested by the ISRM test standard is still applicable for thermally treated rock.

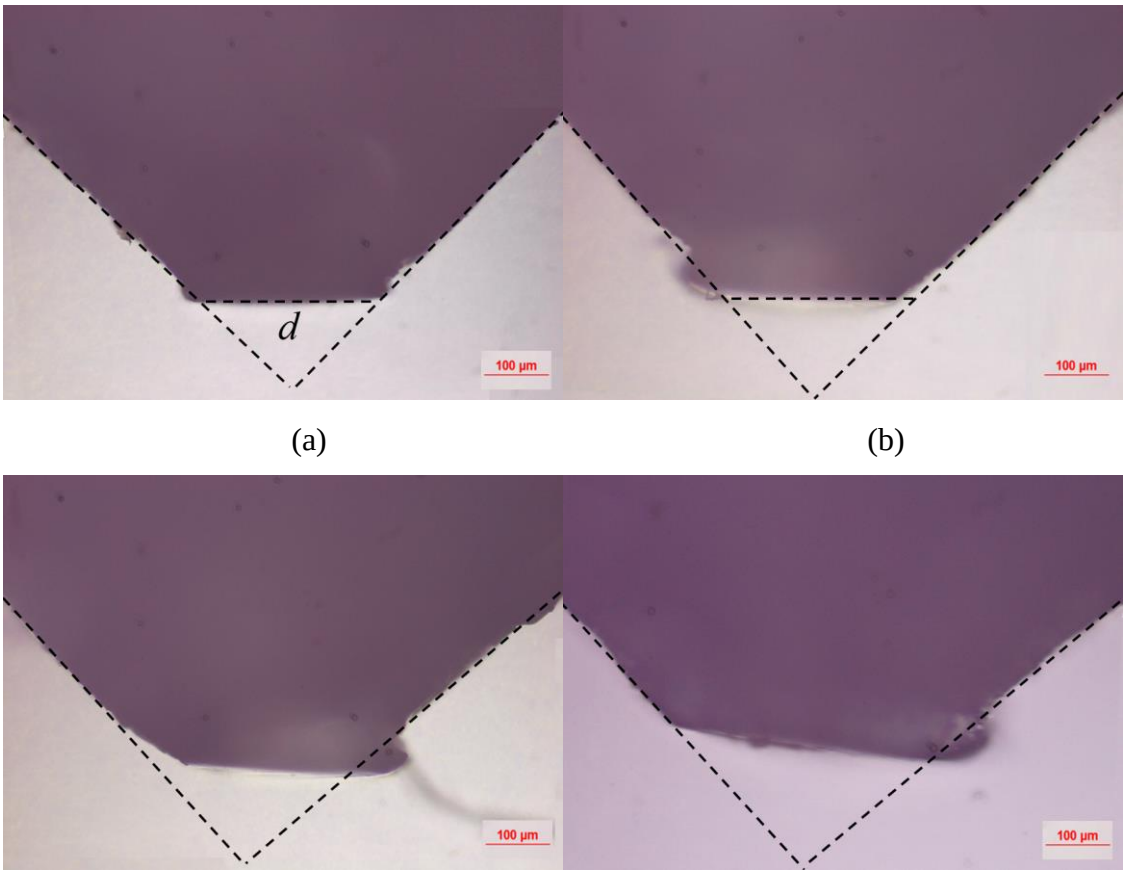

(a) (b)

(c) (d)

Figure 6-7 Evolution of stylus tip after the scratch for (a) 5, (b) 10, (c) 15, and (d) 20 mm distances across granite specimen treated with 600 ºC heating temperature.

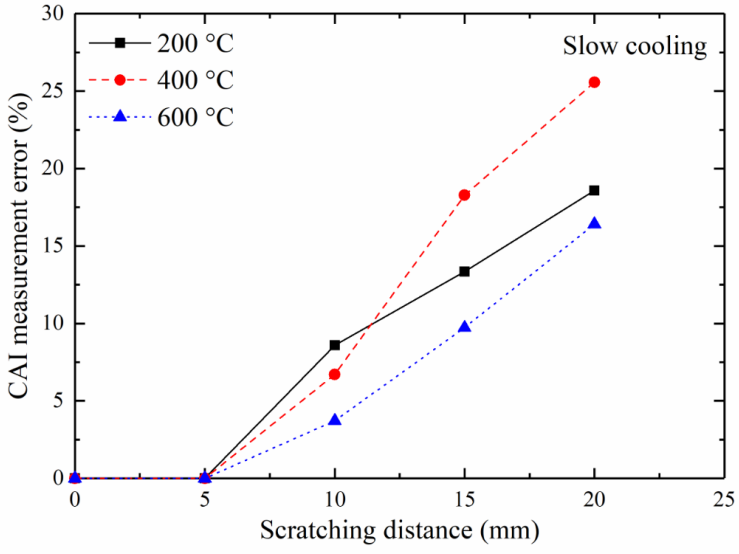

(a)

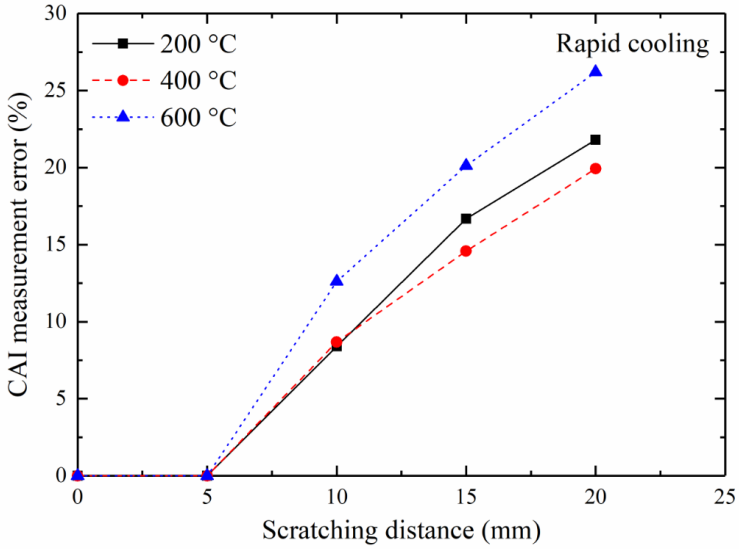

(b)

Figure 6-8 CAI measurement error as a function of scratching distance after (a) slow cooling and (b) rapid cooling.

Thermal treatment fundamentally modifies rock brittleness and subsequently influences the stylus indentation. Rock brittleness can be affected by various thermal and mechanical effects (Li et al., 2018). The indentation stress and the brittleness index are

then examined to further understand the stylus and rock interaction. The Rockwell C hardness is determined using the Rockwell hardness testes on the intact and thermally treated rocks, and each stylus was examined 20 times in a Rockwell C hardness test. Then the indentation stress is obtained based on the correlation between the Rockwell C hardness and the Vickers hardness number (ASTM, 2007). The results show that the Rockwell C hardness decreases with a higher heating temperature, and the Rockwell C hardness after the slow cooling is larger than that after the rapid cooling (Figure 6-9a). The rock brittleness is also assessed according to B_4 brittleness index. The brittleness index has a reliable relationship with the CAI value among different definitions of brittleness (Ündül and Er, 2017). The Brazilian tensile strength of Bukit Timah granite after slow cooling as a function of temperature is obtained from Li et al. (2017), and the uniaxial compressive strengths after slow cooling are determined following the ISRM test standard for uniaxial compression tests (ISRM, 1979) (Figure 6-9b). A slight increase in uniaxial compressive strength at 200 ºC heating temperature is due to the thermal expansion of mineral grains (Yang et al., 2017). Figure 6-9c demonstrates that the correlation between the indentation stress and the brittleness index for slow cooling. A larger brittleness index corresponds roughly to less cracked rock after the treatment with a lower heating temperature. Hence, the indentation stress increases when the stylus is moved on more brittle, less cracked rock. After slow cooling, less cracked rock becomes more brittle, and the stylus less readily stretches into the cracked rock with a higher indentation stress.

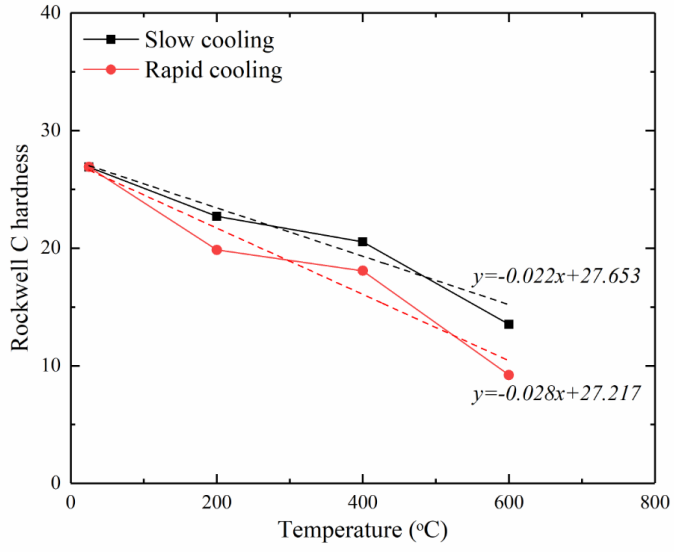
Slow cooling
Rapid cooling
Rockwell C hardness
Temperature (°C)
y=-0.022x+27.653
y=-0.028x+27.217
0
10
20
30
40
0
200
400
600
800

(a)

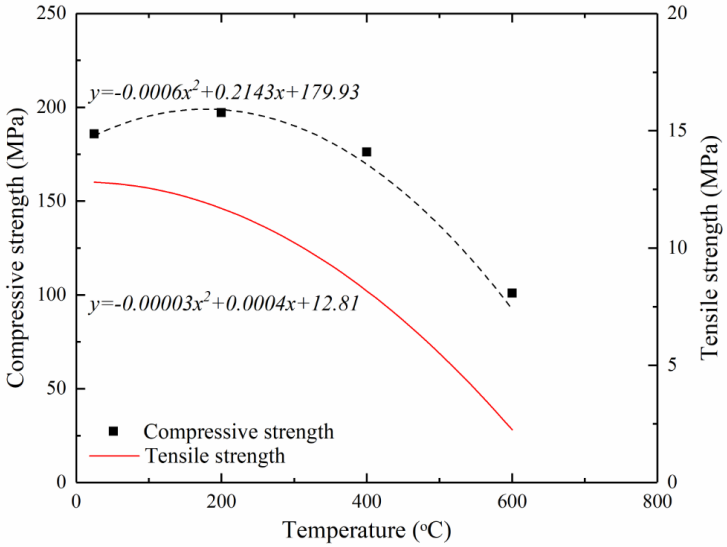
y=-0.0006x²+0.2143x+179.93
y=-0.00003x²+0.0004x+12.81
Compressive strength
Tensile strength
Compressive strength (MPa)
Tensile strength (MPa)
Temperature (°C)
0
50
100
150
200
250
0
5
10
15
20
0
200
400
600
800

(b)

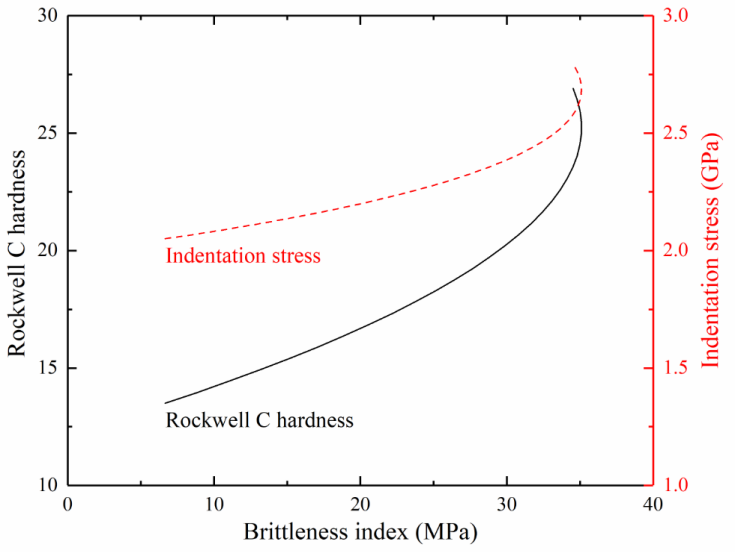

(c)

Figure 6-9 (a) Rockwell C hardness of granite specimen as a function of heating temperature, (b) temperature-dependent compressive and tensile strengths of Bukit Timah granite after slow cooling, and (c) Rockwell C hardness and indentation stress as a function of brittleness index after slow cooling.

6.5 Summary

This study carries out a series of CAI tests on intact and thermally treated granite specimens to examine the influence of stylus indentation on the measurement of CAI value. The CAI test results exhibit that the CAI value markedly increases and the wear flat can be obtained during the first few millimeters scratching distance. However, the stylus tip is affected by side wear and steel stretching during the subsequent scratching distance. The irregular shape of the worn stylus is associated with the interaction between the indented stylus and the cracked granite and may not be reasonable to directly evaluate the CAI value. It is thus suggested evaluating the wear flat by reconstructing the intact stylus profile. The suitable scratching distance may be different for various types of rocks, depending on the evolution of rock brittleness after thermal treatment. The CAI measurement with 10 mm scratching distance is also evaluated as suggested by the ISRM

test standard and the maximum error is found to be about 10% for highly cracked rock, indicating that the suggested scratching distance is still appliable. Accurate measurement of rock abrasivity can improve the estimation of cutting tool wear and the efficiency of rock mass breakage during underground excavation and geo-energy extraction.

CHAPTER 7 CONCLUSIONS AND FUTURE WORK

7.1 Conclusions

This thesis mainly explores the changes in rock brittleness induced from different mechanical and thermal effects on rocks and inclusion-bearing rocks behaviors in underground rock engineering and geo-energy exploitation. The experimental and numerical results both reveal that the rock brittleness can highly influence the mechanical properties and failure characteristics of different rocks. Chapter 4 reports that the rock breaking can be modified by applying an initial pressure (e.g., hydration of expansive mortar) on rock openings. The results suggest an extra procedure for the evolution of expansive pressure prior to drilling and blasting. However, the test condition is limited without considering the factors such as rock type, the size, number, and shape of a borehole, and geo-stress, etc. Chapter 5 establishes a DEM model to investigate the tensile behavior of inclusion-bearing specimens with different inclusion properties and external conditions (e.g., temperature and loading rate). It aims to provide a reference for applications such as concrete-encased coal pillar system and grouted coal mass in resisting the dynamic stress disturbance. The study of inclusion-bearing rock behavior is nevertheless a comprehensive topic with the variables of interest in terms of material properties, rock configuration, and surrounding circumstances. Chapter 6 assesses the rock abrasivity of granite under the thermal and cooling treatments. It emphasizes the roles of rock degradation and stylus-rock interaction in controlling the CAI value with elevated temperature and different cooling rates. The quantitative analyses of tip penetration depth, cutting force, and removed rocks during the CAI test can contribute to a more accurate rock abrasivity estimation.

The dynamic failure response of expansive mortar-filled rocks is investigated experimentally and numerically in Chapter 4 to gain insight into the dynamic rock failure control. The filled specimen is more ductile than that of the intact rock, which promotes

fracture generation and rock deformability. The rocks containing expansive mortar fail with a more complex fracture network, comprising of a circular tangential fracture with several evenly distributed radial fractures. It demonstrates that the utilization of expansive mortar in an underground excavation can benefit rock fragmentation and blast wave attenuation. However, the application of expansive mortar to modify rock damage should be further investigated in field trials.

The simulation results based on the DEM model in Chapter 5 suggest that both the effects of external conditions (e.g., temperature and loading rate) and inherent inclusion properties (e.g., strength and size) can significantly affect the mechanical properties and failure characteristics of inclusion-bearing specimens. The strength ratio and loading rate/temperature concurrently change the nominal tensile strength to different degrees, depending on the magnitude of strength ratio. The failure patterns are generalized into three categories as the inclusion strength increases from low (e.g., 0.2), moderate (e.g., 0.8 and 1.2) to high (e.g., 2.4). The induced crack numbers in inclusion and rock parts can quantify the specimen failure mode and are closely related to the evolution of nominal tensile strength.

To investigate the effect of rock brittleness on rock cutting efficiency, the CAI value of granite at extreme temperatures followed by cooling treatments is evaluated in Chapter 6. The CAI value rises dramatically in the first 5 mm scratching distance, and the remaining 15 mm scratching contributes less than 20% of the total CAI. For a given scratching distance, rocks cooled naturally in the air have a higher CAI value than those of specimens cooled in water, because rapid cooling can aggravate the rock degradation. The normalized P-wave velocity is negatively proportional to a higher heating temperature, indicating the increased thermal cracks. The analysis of AE features reflects the stylus and rock interaction and is qualitatively represented by the microscopic stylus tip observation at different scratching distances.

Overall, the mechanical and thermal effects can fundamentally modify the rock brittleness for both rocks and inclusion-bearing rocks. A further understanding of rock brittleness may contribute to the achievement of a higher underground excavation efficiency and safer construction environment. The introduction of expansive mortar significantly reduces the brittleness of surrounding rocks, implying a controllable energy release path and decreased energy consumption when applied jointly with blasting. As the temperature increases, a lower brittleness index corresponds to a higher CAI value and a reduced indentation stress. The strength of the inclusion in relative to that of the rock and loading rate can concurrently affect the specimen brittleness, while the temperature effect is less important. The strength ratio dominates the change of brittleness with a softer inclusion and becomes a subdominant factor when the inclusion is stronger than the rock.

7.2 Future work

The field test regarding the dynamic effect of expansive mortar on surrounding rocks is proposed in future work. Besides, the geo-stress can restrict the cracking efficiency for the application of expansive mortar (Duan et al., 2019c). Here the DEM simulation for the dynamic responses of hollow discs under a non-uniform distributed confining stress condition is established with different radial stress gradients. Figure 7-1 demonstrates the plane stress distribution for the section perpendicular to the loading direction. The internal and external stresses mimic the stress provided by the expansive mortar and geo-stress. This study may reveal the dynamic rock mechanical properties and failure features under radial non-uniform confining stress state.

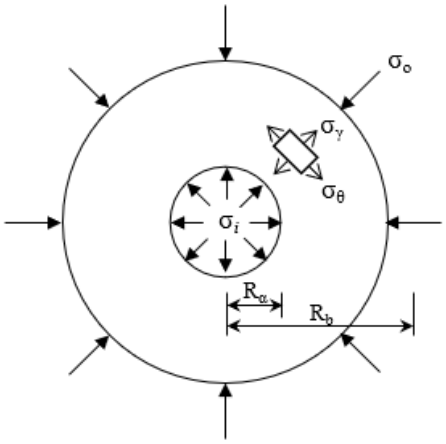

Figure 7-1 Plane stress distribution for the section perpendicular to the loading direction (σ_i and σ_o are the internal and external confining stresses, respectively; R_α and R_b are the internal and external radii, respectively; and σ_γ and σ_θ are the radial and tangential stresses, respectively).

Shotcrete is commonly used to reinforce the tunnel walls in underground projects, in which the rock-concrete interface is the fragile part (Figure 7-2a). Previous studies mainly focused on the influence of interfacial roughness and declination angle on the entire rock behaviors (Chang et al., 2018; Zhou et al., 2020; Wanniarachchi and Wu W, 2021), but few attempts have been made to reveal the related fracture mechanism and rock brittleness. Thus, it is proposed to investigate the fracture properties of rock-concrete interfaces with a single flaw under static and dynamic loading conditions. Figure 7-2b illustrates the specimen configuration for the bi-material fracture mechanism test. This study may reveal the dynamic fracture mechanism for rock-concrete bi-materials under Mode I, Mode II, and a mixed Mode I and II loading.

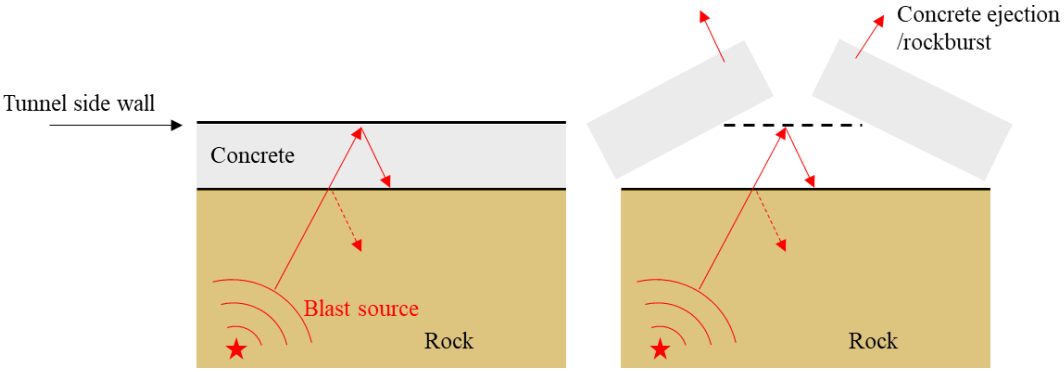

(a)

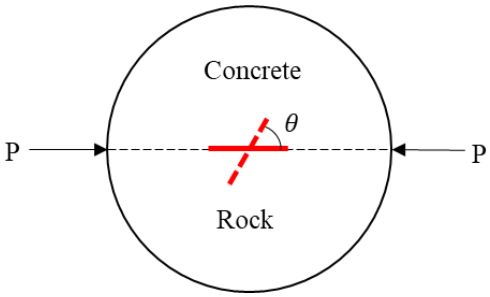

(b)

Figure 7-2 (a) Sketch of failed tunnel wall under dynamic disturbance, and (b) specimen configuration for rock-concrete disc with a preset flaw (P is the applied load along with the rock-concrete interface, and θ is the inclination angle of the flaw with respect to the loading direction).

References

Abaqus (2014) Version 6.14 Documentation. Dassault Systemes Simulia Corporation.

Ahrens, T. J. (1995). Mineral physics & crystallography: a handbook of physical constants (Vol. 2). American Geophysical Union.

Alber, M. (2008). Stress dependency of the Cerchar abrasivity index (CAI) and its effects on wear of selected rock cutting tools. Tunnelling and Underground Space Technology, 23(4), 351-359.

Alber, M., Yaralı, O., Dahl, F., Bruland, A., Käsling, H., Michalakopoulos, T. N., and Özarslan, A. (2014). ISRM suggested method for determining the abrasivity of rock by the CERCHAR abrasivity test. Rock Mechanics and Rock Engineering, 47, 261-266.

Altindag, R. (2002). The evaluation of rock brittleness concept on rotary blast holds drills. Journal of the Southern African Institute of Mining and Metallurgy, 102(1), 61-66.

Amitrano, D. (2003). Brittle-ductile transition and associated seismicity: Experimental and numerical studies and relationship with the b value. Journal of Geophysical Research: Solid Earth, 108(B1).

Arshadnejad, S., and Niu, J. (2014). Birth of the first crack and its growth under incremental static loading between two holes in brittle rocks. Journal of Earth Engineering, 1(1), 1-15.

Arshadnejad, S., Goshtasbi, K., and Aghazadeh, J. (2011). A model to determine hole spacing in the rock fracture process by non-explosive expansion material. International Journal of Minerals, Metallurgy, and Materials, 18(5), 509-514.

ASTM (2007). Standard hardness conversion tables for metals relationship among Brinell hardness, Vickers hardness, Rockwell hardness, Superficial hardness, Knoop hardness, and Scleroscope hardness. ASTM International, West Conshohocken, United States.

ASTM (2008a). D2936-08 Standard test method for direct tensile strength of intact rock core specimens. Annual book of ASTM standards. ASTM International, West Conshohocken.

ASTM (2008b). D3967-08 Standard test method for splitting tensile strength of intact rock core specimens. Annual book of ASTM standards. ASTM International, West Conshohocken.

Bahaaddini, M., Sharrock, G., and Hebblewhite, B. K. (2013). Numerical investigation of the effect of joint geometrical parameters on the mechanical properties of a non-persistent jointed rock mass under uniaxial compression. Computers and Geotechnics, 49, 206-225.

Bai, Q. S., Tu, S. H., and Zhang, C. (2016). DEM investigation of the fracture mechanism of rock disc containing hole (s) and its influence on tensile strength. Theoretical and Applied Fracture Mechanics, 86, 197-216.

Bauer, S. J., Song, B., and Sanborn, B. (2019). Dynamic compressive strength of rock salts. International Journal of Rock Mechanics and Mining Sciences, 113, 112-120.

Bennett, K. C., Berla, L. A., Nix, W. D., and Borja, R. I. (2015). Instrumented nanoindentation and 3D mechanistic modeling of a shale at multiple scales. Acta Geotechnica, 10(1), 1-14.

Bieniawski, Z. T., and Hawkes, I. (1978). Suggested methods for determining tensile strength of rock materials. International Journal of Rock Mechanics and Mining Sciences and Geomechanics Abstracts, 15(3), 99-103.

Bowers, D., and Hudson, J. A. (1999). Defining the scalar moment of a seismic source with a general moment tensor. Bulletin of the Seismological Society of America, 89(5), 1390-1394.

Cerchar—Centre d'E´ tudes et des Recherches des Charbonnages de France (1986) The Cerchar abrasivity index. Verneuil.

Chang, S. H., and Lee, C. I. (2004). Estimation of cracking and damage mechanisms in rock under triaxial compression by moment tensor analysis of acoustic emission. International Journal of Rock Mechanics and Mining Sciences, 41(7), 1069-1086.

Chang, X., Lu, J., Wang, S., and Wang, S. (2018). Mechanical performances of rock-concrete bi-material disks under diametrical compression. International Journal of Rock Mechanics and Mining Sciences, 104, 71-77.

Chen, J., Zhang, G., Chen, H., and Yin, X. (2014). The construction of shale rock physics effective model and prediction of rock brittleness. In 2014 SEG Annual Meeting. OnePetro.

Chen, L., Fang, Q., Jiang, X., Ruan, Z., and Hong, J. (2015). Combined effects of high temperature and high strain rate on normal weight concrete. International Journal of Impact Engineering, 86, 40-56.

Chen, W., Zhang, B., and Forrestal, M. J. (1999). A split Hopkinson bar technique for low-impedance materials. Experimental Mechanics, 39(2), 81-85.

Chen, Z., Bao, H., Dai, Y., and Liu, Y. (2022). Numerical prediction based on XFEM for mixed-mode crack growth path and fatigue life under cyclic overload. International Journal of Fatigue, 162, 106943.

Cho, H., Nam, Y., Kim, K., Lee, J., and Sohn, D. (2018). Numerical simulations of crack path control using soundless chemical demolition agents and estimation of required pressure for plain concrete demolition. Materials and Structures, 51(6), 169.

Cho, N., Martin, C. D., and Sego, D. C. (2008). Development of a shear zone in brittle rock subjected to direct shear. International Journal of Rock Mechanics and Mining Sciences, 45(8), 1335-1346.

Christensen, R. J., Swanson, S. R., and Brown, W. S. (1972). Split-hopkinson-bar tests on rock under confining pressure. Experimental Mechanics, 12(11), 508-513.

Clark, V. A., Spencer, T. W., and Tittmann, B. R. (1981). The effect of thermal cycling on the seismic quality factor Q of some sedimentary rocks. Journal of Geophysical Research: Solid Earth, 86(B8), 7087-7094.

Cook, B. K., Lee, M. Y., DiGiovanni, A. A., Bronowski, D. R., Perkins, E. D., and Williams, J. R. (2004). Discrete element modeling applied to laboratory simulation of near-wellbore mechanics. International Journal of Geomechanics, 4(1), 19-27.

Coviello, A., Lagioia, R., and Nova, R. (2005). On the measurement of the tensile strength of soft rocks. Rock Mechanics and Rock Engineering, 38(4), 251-273.

Cruz, F., Roehl, D., and do Amaral Vargas Jr, E. (2019). An XFEM implementation in Abaqus to model intersections between fractures in porous rocks. Computers and Geotechnics, 112, 135-146.

Cundall, P. A. (1971). A computer model for simulating progressive, large-scale movement in blocky rock system. In Proceedings of the International Symposium on Rock Mechanics.

Cundall, P. A. (2001). A discontinuous future for numerical modelling in geomechanics? Proceedings of the institution of civil engineers-geotechnical engineering, 149(1), 41-47.

Cundall, P. A., and Strack, O. D. (1979). A discrete numerical model for granular assemblies. Geotechnique, 29(1), 47-65.

Dai, F., Huang, S., Xia, K., and Tan, Z. (2010). Some fundamental issues in dynamic compression and tension tests of rocks using split Hopkinson pressure bar. Rock Mechanics and Rock Engineering, 43(6), 657-666.

Dai, F., Xu, Y., Zhao, T., Xu, N. W., and Liu, Y. (2016). Loading-rate-dependent progressive fracturing of cracked chevron-notched Brazilian disc specimens in split Hopkinson pressure bar tests. International Journal of Rock Mechanics and Mining Sciences, 88, 49-60.

Dang, W. G., Wu, W., Konietzky, H., and Qian, J. Y. (2019) Effect of shear-induced aperture evolution on fluid flow in rock fractures. Computers and Geotechnics, 114, 103152.

Daux, C., Moës, N., Dolbow, J., Sukumar, N., and Belytschko, T. (2000). Arbitrary branched and intersecting cracks with the extended finite element method. International Journal for Numerical Methods in Engineering, 48(12), 1741-1760.

Davi, R., Vavryčuk, V., Charalampidou, E. M., and Kwiatek, G. (2013). Network sensor calibration for retrieving accurate moment tensors of acoustic emissions. International Journal of Rock Mechanics and Mining Sciences, 62, 59-67.

Davies, R. M. (1948). A critical study of the Hopkinson pressure bar. Philosophical Transactions of the Royal Society of London. Series A, Mathematical and Physical Sciences, 240(821), 375-457.

De Silva, R. V., Pathegama Gamage, R., Perera, A., and Samintha, M. (2016). An alternative to conventional rock fragmentation methods using SCDA: a review. Energies, 9(11), 958.

De Silva, V. R. S., and Ranjith, P. G. (2019). Intermittent and multi-stage fracture stimulation to optimise fracture propagation around a single injection well for enhanced in-situ leaching applications. Engineering Fracture Mechanics, 220, 106662.

De Silva, V. R. S., Ranjith, P. G., Perera, M. S. A., Wu, B., and Rathnaweera, T. D. (2017). Investigation of the mechanical, microstructural and mineralogical morphology of soundless cracking demolition agents during the hydration process. Materials Characterization, 130, 9-24.

De Silva, V. R. S., Ranjith, P. G., Perera, M. S. A., Wu, B., and Rathnaweera, T. D. (2018a). A modified, hydrophobic soundless cracking demolition agent for non-explosive demolition and fracturing applications. Process Safety and Environmental Protection, 119, 1-13.

De Silva, V. R. S., Ranjith, P. G., Perera, M. S. A., Wu, B., and Wanniarachchi, W. A. M. (2018b). A low energy rock fragmentation technique for in-situ leaching. Journal of Cleaner Production, 204, 586-606.

Deliormanlı, A. H. (2012). Cerchar abrasivity index (CAI) and its relation to strength and abrasion test methods for marble stones. Construction and Building Materials, 30, 16-21.

Du, H. B., Dai, F., Xu, Y., Yan, Z., and Wei, M. D. (2020). Mechanical responses and failure mechanism of hydrostatically pressurized rocks under combined compression-shear impacting. International Journal of Mechanical Sciences, 165, 105219.

Du, H., Dai, F., Wei, M., Li, A., and Yan, Z. (2021). Dynamic compression–shear response and failure criterion of rocks with hydrostatic confining pressure: an experimental investigation. Rock Mechanics and Rock Engineering, 54(2), 955-971.

Du, H., Dai, F., Xia, K., Xu, N., and Xu, Y. (2017). Numerical investigation on the dynamic progressive fracture mechanism of cracked chevron notched semi-circular bend specimens in split Hopkinson pressure bar tests. Engineering Fracture Mechanics, 184, 202-217.

Duan, K., and Kwok, C. Y. (2015). Discrete element modeling of anisotropic rock under Brazilian test conditions. International Journal of Rock Mechanics and Mining Sciences, 78, 46-56.

Duan, K., Ji, Y., Xu, N., Wan, Z., and Wu, W. (2019a). Excavation-induced fault instability: possible causes and implications for seismicity. Tunnelling and Underground Space Technology, 92, 103041.

Duan, K., Li, Y., Wang, L., Zhao, G., and Wu, W. (2019b). Dynamic responses and failure modes of stratified sedimentary rocks. International Journal of Rock Mechanics and Mining Sciences, 122, 104060.

Duan, K., Ji, Y., Wu, W., and Kwok, C. Y. (2019c). Unloading-induced failure of brittle rock and implications for excavation-induced strain burst. Tunnelling and Underground Space Technology, 84, 495-506.

Duffy, J., Campbell, J. D., and Hawley, R. H. (1971). On the use of a torsional split Hopkinson bar to study rate effects in 1100-0 aluminum. 83-91.

Dutta, P. K., and Kim, K. (1993). High-strain-rate tensile behavior of sedimentary and igneous rocks at low temperatures. U.S. Army Corps of Engineers, Cold Regions Research and Engineering Laboratory.

Er, S., and Tuğrul, A. (2016). Correlation of physico-mechanical properties of granitic rocks with Cerchar Abrasivity Index in Turkey. Measurement, 91, 114-123.

Fairhurst, C. (1964). On the validity of the 'Brazilian' test for brittle materials. In International Journal of Rock Mechanics and Mining Sciences and Geomechanics Abstracts (Vol. 1, No. 4, pp. 535-546). Pergamon.

Feignier, B., and Young, R. P. (1992). Moment tensor inversion of induced microseisnmic events: Evidence of non-shear failures in the− 4< M<− 2 moment magnitude range. Geophysical Research Letters, 19(14), 1503-1506.

Forrestal, M. J., Wright, T. W., and Chen, W. (2007). The effect of radial inertia on brittle samples during the split Hopkinson pressure bar test. International Journal of Impact Engineering, 34(3), 405-411.

Frew, D. J., Forrestal, M. J., and Chen, W. (2001). A split Hopkinson pressure bar technique to determine compressive stress-strain data for rock materials. Experimental Mechanics, 41(1), 40-46.

Frew, D. J., Forrestal, M. J., and Chen, W. (2002). Pulse shaping techniques for testing brittle materials with a split Hopkinson pressure bar. Experimental Mechanics, 42(1), 93-106.

Gambatese, J. A. (2003). Controlled concrete demolition using expansive cracking agents. Journal of Construction Engineering and Management, 129(1), 98-104.

Gholinejad, M., and Arshadnejad, S. (2012). An experimental approach to determine the hole-pressure under expansion load. Journal of the Southern African Institute of Mining and Metallurgy, 112(7), 631-635.

Glover, P. W. J., Baud, P., Darot, M., Meredith, P., Boon, S. A., LeRavalec, M., and Reuschlé, T. (1995). α/β phase transition in quartz monitored using acoustic emissions. Geophysical Journal International, 120(3), 775-782.

Gomez, J. T., Shukla, A., and Sharma, A. (2001). Static and dynamic behavior of concrete and granite in tension with damage. Theoretical and Applied Fracture Mechanics, 36(1), 37-49.

Gomez-del Rio, T., Barbero, E., Zaera, R., and Navarro, C. (2005). Dynamic tensile behaviour at low temperature of CFRP using a split Hopkinson pressure bar. Composites Science and Technology, 65(1), 61-71.

Gong, Q.M, and Zhao, J. (2007). Influence of rock brittleness on TBM penetration rate in Singapore granite. Tunnelling and Underground Space Technology, 22(3), 317-324.

Grgic, D., Giot, R., Homand, F., and Giraud, A. (2005). Effect of suction on the mechanical behaviour of iron ore rock. International Journal for Numerical and Analytical Methods in Geomechanics, 29(8), 789-827.

Griffith, A. (1924). The theory of rupture. Journal of Applied Mechanics 55-63.

Guha Roy, D., and Singh, T. N. (2016). Effect of heat treatment and layer orientation on the tensile strength of a crystalline rock under Brazilian test condition. Rock Mechanics and Rock Engineering, 49(5), 1663-1677.

Guo, J., Zhao, Z., He, S., Liang, H., and Liu, Y. (2015). A new method for shale brittleness evaluation. Environmental Earth Sciences, 73(10), 5855-5865.

Guo, T., Zhang, S., Ge, H., and Qu, Z. (2015a). A novel" soundless cracking agent fracturing" for shale gas reservoir stimulation. International Journal of Environmental Science and Development, 6(9), 681.

Guo, T., Zhang, S., Ge, H., Wang, X., Lei, X., and Xiao, B. (2015b). A new method for evaluation of fracture network formation capacity of rock. Fuel, 140, 778-787.

Gutenberg, B., and Richter, C. F. (1944). Frequency of earthquakes in California. Bulletin of the Seismological society of America, 34(4), 185-188.

Hajiabdolmajid, V., and Kaiser, P. (2003). Brittleness of rock and stability assessment in hard rock tunneling. Tunnelling and Underground Space Technology, 18(1), 35-48.

Han, G., Jing, H., Su, H., Liu, R., Yin, Q., and Wu, J. (2019). Effects of thermal shock due to rapid cooling on the mechanical properties of sandstone. Environmental Earth Sciences, 78(5), 1-9.

Hanif, M., Mohammed, N. O. O. R., and AL-MAGHRABI, N. H. (2007). Effective use of expansive cement for the deformation and fracturing of granite. Gazi University Journal of Science, 20(1), 1-5.

Harada, T., Idemitsu, T., Watanabe, A., and Takayama, S. I. (1989). The design method for the demolition of concrete with expansive demolition agents. In Fracture of Concrete and Rock (pp. 47-57). Springer, New York, NY.

Harada, T., Soeda, K., Idemitsu, T., and Watanabe, A. (1993). Characteristics of expansive pressure of an expansive demolition agent and the development of new pressure transducers. Doboku Gakkai Ronbunshu, 478, 91-100.

Harding, J. (1965). Tensile impact testing by a magnetic loading technique. Journal of Mechanical Engineering Science, 7(2), 163-176.

Hauser, F. E., Simmons, J. A., and Dorn, J. E. (1961). Response of metals to high velocity deformation. PG Shewmon and VF Zackay Interscience Pub., NY, 93-103.

Hazzard, J. F., and Damjanac, B. (2013). Further investigations of microseismicity in bonded particle models. In 3rd International FLAC/DEM Symposium (pp. 1-11).

Hazzard, J. F., and Young, R. P. (2000). Simulating acoustic emissions in bonded-particle models of rock. International Journal of Rock Mechanics and Mining Sciences, 37(5), 867-872.

Hazzard, J. F., and Young, R. P. (2002). Moment tensors and micromechanical models. Tectonophysics, 356(1-3), 181-197.

Hazzard, J. F., Young, R. P., and Maxwell, S. C. (2000). Micromechanical modeling of cracking and failure in brittle rocks. Journal of Geophysical Research: Solid Earth, 105(B7), 16683-16697.

Helinski, M., Fahey, M., and Fourie, A. (2007). Numerical modeling of cemented mine backfill deposition. Journal of Geotechnical and Geoenvironmental Engineering, 133(10), 1308-1319.

Hinze, J., and Brown, J. (1994). Properties of soundless chemical demolition agents. Journal of Construction Engineering and Management, 120(4), 816-827.

Hinze, J., and Nelson, A. (1996). Enhancing performance of soundless chemical demolition agents. Journal of Construction Engineering and Management, 122(2), 193-195.

Hirata, A., Kameoka, Y., and Hirano, T. (2007). Safety management based on detection of possible rock bursts by AE monitoring during tunnel excavation. Rock Mechanics and Rock Engineering, 40(6), 563-576.

Hökmark, H., and Claesson, J. (2005). Use of an analytical solution for calculating temperatures in repository host rock. Engineering geology, 81(3), 353-364.

Hondros, G. (1959). The evaluation of Poisson's ratio and the modulus of materials of low tensile resistance by the Brazilian (indirect tensile) test with particular reference to concrete. Australian Journal of Applied Mechanics, 10(3), 243-268.

Hornby, B. E., Schwartz, L. M., and Hudson, J. A. (1994). Anisotropic effective-medium modeling of the elastic properties of shales. Geophysics, 59(10), 1570-1583.

Hu, J., Sun, Q., and Pan, X. (2018). Variation of mechanical properties of granite after high-temperature treatment. Arabian Journal of Geosciences, 11(2), 1-8.

Huang, S., Xia, K., Yan, F., and Feng, X. (2010). An experimental study of the rate dependence of tensile strength softening of Longyou sandstone. Rock Mechanics and Rock Engineering, 43(6), 677-683.

Huang, Z., Zhang, Y., Wu, W. (2016). Analysis of mechanical and wave properties of heat-treated marble by water cooling. Rock Soil Mech, 37(2):367–375.

Hucka, V., and Das, B. (1974). Brittleness determination of rocks by different methods. In International Journal of Rock Mechanics and Mining Sciences & Geomechanics Abstracts (Vol. 11, No. 10, pp. 389-392). Pergamon.

Huynh, M. P., and Laefer, D. F. (2009). Expansive cements and soundless chemical demolition agents: state of technology review. In Presented at the 11th Conference on Science and Technology, Ho Chi Minh City Vietnam, October 21-23, 2009.

Ilyashenko, A. V., and Kuznetsov, S. V. (2018). Pochhammer–Chree waves: polarization of the axially symmetric modes. Archive of Applied Mechanics, 88(8), 1385-1394.

Imani, M., Nejati, H. R., and Goshtasbi, K. (2017). Dynamic response and failure mechanism of Brazilian disk specimens at high strain rate. Soil Dynamics and Earthquake Engineering, 100, 261-269.

Ish-Shalom, M., and Bentur, A. (1975). Properties of type K expansive cement of pure components III. Hydration of pure expansive component under varying restraining conditions. Cement and Concrete Research, 5(2), 139-152.

ISRM (1978) Suggested Methods for Determining Tensile Strength of Rock Materials Part 2: Suggested Method for determining indirect tensile strength by the Brazil Test. International Journal of Rock Mechanics and Mining Sciences, 15, 99-103.

ISRM (2007a). Suggested method for determining the tensile strength of rock materials, in: the complete ISRM suggested methods for rock characterization, testing and monitoring: 1974-2006, 101-103.

ISRM (2007b). Suggested method for determining the uniaxial compressive strength and deformation of rock materials, in: the complete ISRM suggested methods for rock characterization, testing and monitoring: 1974-2006, 137-140.

ISTM (1979). Suggested methods for determining the uniaxial compressive strength and deformability of rock materials. International Journal of Rock Mechanics and Mining Sciences, 16, 135-140.

Itasca (2010) PFC2D: particle flow code in 2 dimensions.4.0ed. Minneapolis: Itasca.

Jahandideh, A., and Jafarpour, B. (2016). Optimization of hydraulic fracturing design under spatially variable shale fracability. Journal of Petroleum Science and Engineering, 138, 174-188.

Janeiro, R. P., and Einstein, H. H. (2010). Experimental study of the cracking behavior of specimens containing inclusions (under uniaxial compression). International Journal of Fracture, 164(1), 83-102.

Jarvie, D. M., Hill, R. J., Ruble, T. E., and Pollastro, R. M. (2007). Unconventional shale-gas systems: the Mississippian Barnett Shale of north-central Texas as one model for thermogenic shale-gas assessment. American Association of Petroleum Geologists Bulletin, 91(4), 475-499.

Ji, Y., Wang, L., Zheng, Y., and Wu, W. (2021). Temperature-dependent abrasivity of Bukit Timah granite and implications for drill bit wear in thermo-mechanical drilling. Acta Geotechnica, 16(3), 885-893.

Ji, Y. L., and Wu, W. (2020) Injection-driven fracture activation in granite: mechanism and implications. Tectonophysics, 791, 228572.

Jia, Y. Z., Wu, W., Kong, X. Z. (2020) Injection-induced slip heterogeneity on faults in shale reservoirs. International Journal of Rock Mechanics and Mining Sciences, 131, 104363.

Jiao, Y. Y., Zhang, X. L., and Zhao, J. (2012). Two-dimensional DDA contact constitutive model for simulating rock fragmentation. Journal of Engineering Mechanics, 138(2), 199-209.

Kahraman, S. A. İ. R. (2002). Correlation of TBM and drilling machine performances with rock brittleness. Engineering Geology, 65(4), 269-283.

Kant, M. A., Ammann, J., Rossi, E., Madonna, C., Höser, D., and Rudolf von Rohr, P. (2017). Thermal properties of Central Aare granite for temperatures up to 500 C: irreversible changes due to thermal crack formation. Geophysical Research Letters, 44(2), 771-776.

Kempka, T., Fernández-Steeger, T., Li, D. Y., Schulten, M., Schlüter, R., and Krooss, B. M. (2011). Carbon dioxide sorption capacities of coal gasification residues. Environmental Science & Technology, 45(4), 1719-1723.

Khan, A. J., Iqbal, N., Saeed, H. A., and Tarar, W. A. (2016). Development of material model for assessment of brittle cracking behavior of plexiglas. In IOP Conference Series: Materials Science and Engineering (Vol. 146, No. 1, p. 012008).

Kılıç, A. L., Yasar, E., and Celik, A. G. (2002). Effect of grout properties on the pull-out load capacity of fully grouted rock bolt. Tunnelling and Underground Space Technology, 17(4), 355-362.

Kim, K. Y., Zhuang, L., Yang, H., Kim, H., and Min, K. B. (2016). Strength anisotropy of Berea sandstone: results of X-ray computed tomography, compression tests, and discrete modeling. Rock Mechanics and Rock Engineering, 49(4), 1201-1210.

Kolsky, H. (1963) Stress waves in solids. Courier Corporation.

Kolsky, H. (1949). An investigation of the mechanical properties of materials at very high rates of loading. Proceedings of the physical society. Section B, 62(11), 676.

Kumari, W. G. P., Beaumont, D. M., Ranjith, P. G., Perera, M. S. A., Avanthi Isaka, B. L., and Khandelwal, M. (2019). An experimental study on tensile characteristics of granite rocks exposed to different high-temperature treatments. Geomechanics and Geophysics for Geo-Energy and Geo-Resources, 5(1), 47-64.

Kranz, R. L. (1983). Microcracks in rocks: a review. Tectonophysics, 100(1-3), 449-480.

Laefer, D. F., Ambrozevitch-Cooper, N., Huynh, M. P., Midgette, J., Ceribasi, S., and Wortman, J. (2010). Expansive fracture agent behaviour for concrete cracking. Magazine of Concrete Research, 62(6), 443-452.

Lei, X. (2012). Dragon-Kings in rock fracturing: Insights gained from rock fracture tests in the laboratory. The European Physical Journal Special Topics, 205(1), 217-230.

Leucci, G., and De Giorgi, L. (2006). Experimental studies on the effects of fracture on the P and S wave velocity propagation in sedimentary rock ("Calcarenite del Salento"). Engineering Geology, 84(3-4), 130-142.

Li, D., and Wong, L. N. Y. (2013). The Brazilian disc test for rock mechanics applications: review and new insights. Rock Mechanics and Rock Engineering, 46(2), 269-287.

Li, J. C., Li, H. B., Jiao, Y. Y., Liu, Y. Q., Xia, X., and Yu, C. (2014). Analysis for oblique wave propagation across filled joints based on thin-layer interface model. Journal of Applied Geophysics, 102, 39-46.

Li, M., Mao, X., Pu, H., Chen, Y., Wu, Y., and Zhang, L. (2017). Effects of heating rate on the dynamic tensile mechanical properties of coal sandstone during thermal treatment. Shock and Vibration, 2017.

Li, Q. M., and Meng, H. (2003). About the dynamic strength enhancement of concrete-like materials in a split Hopkinson pressure bar test. International Journal of Solids and Structures, 40(2), 343-360.

Li, Q., Yin, T., Li, X., and Zhang, S. (2020). Effects of rapid cooling treatment on heated sandstone: a comparison between water and liquid nitrogen cooling. Bulletin of Engineering Geology and the Environment, 79(1), 313-327.

Li, W., Han, Y., Wang, T., and Ma, J. (2017). DEM micromechanical modeling and laboratory experiment on creep behavior of salt rock. Journal of Natural Gas Science and Engineering, 46, 38-46.

Li, W., Zhu, C., Yang, C., Duan, K., and Hu, W. (2018). Experimental and DEM investigations of temperature effect on pure and interbedded rock salt. Journal of Natural Gas Science and Engineering, 56, 29-41.

Li, X. B., Lok, T. S., Zhao, J., and Zhao, P. J. (2000). Oscillation elimination in the Hopkinson bar apparatus and resultant complete dynamic stress–strain curves for rocks. International Journal of Rock Mechanics and Mining Sciences, 37(7), 1055-1060.

Li, X., Feng, F., and Li, D. (2018). Numerical simulation of rock failure under static and dynamic loading by splitting test of circular ring. Engineering Fracture Mechanics, 188, 184-201.

Li, X., Pan, C., Li, X., Shao, C., and Li, H. (2022). Application of a synthetic rock mass approach to the simulation of blasting-induced crack propagation and coalescence in deep fractured rock. Geomechanics and Geophysics for Geo-Energy and Geo-Resources, 8(2), 1-17.

Li, X., Wu, Q., Tao, M., Weng, L., Dong, L., and Zou, Y. (2016). Dynamic Brazilian splitting test of ring-shaped specimens with different hole diameters. Rock Mechanics and Rock Engineering, 49(10), 4143-4151.

Li, X., Zhou, Z., Lok, T. S., Hong, L., and Yin, T. (2008). Innovative testing technique of rock subjected to coupled static and dynamic loads. International Journal of Rock Mechanics and Mining Sciences, 45(5), 739-748.

Li, X., Zou, Y., and Zhou, Z. (2013). Numerical simulation of the rock SHPB test with a special shape striker based on the Discrete Element Method. Rock Mechanics and Rock Engineering, 47(5), 1693-1709.

Li, X.F., Wang, S.B., Ge, S.R., Reza, M., Li, Z.X. (2018). Investigation on the influence mechanism of rock brittleness on rock fragmentation and cutting performance by discrete element method, Measurement 113, 120-130.

Li, Y., Dai, F., Wei, M., and Du, H. (2020). Numerical investigation on dynamic fracture behavior of cracked rocks under mixed mode I/II loading. Engineering Fracture Mechanics, 235, 107176.

Li, Z., Wong, L. N. Y., and Teh, C. I. (2017). Low cost colorimetry for assessment of fire damage in rock. Engineering Geology, 228, 50-60.

Li, Z., Wong, L. N. Y., and Teh, C. I. (2020). Influence of thermal and mechanical loading on development of microcracks in granite. Rock Mechanics and Rock Engineering, 53(5), 2035-2051.

Li, Z., Xu, J., and Bai, E. (2012). Static and dynamic mechanical properties of concrete after high temperature exposure. Materials Science and Engineering: A, 544, 27-32.

Liu, Q., Xiao, F., and Zhao, Z. (2020). Grouting knowledge discovery based on data mining. Tunnelling and Underground Space Technology, 95, 103093.

Liu, S., and Xu, J. (2013). Study on dynamic characteristics of marble under impact loading and high temperature. International Journal of Rock Mechanics and Mining Sciences, 62, 51-58.

Liu, Y., Dai, F., Xu, N., and Zhao, T. (2017). Cyclic flattened Brazilian disc tests for measuring the tensile fatigue properties of brittle rocks. Review of Scientific Instruments, 88(8), 083902.

Liu, Y., Dai, F., Xu, N., Zhao, T., and Feng, P. (2018). Experimental and numerical investigation on the tensile fatigue properties of rocks using the cyclic flattened Brazilian disc method. Soil Dynamics and Earthquake Engineering, 105, 68-82

Liu, Y., He, D., Gao, C., Foley, S., Gao, S., Hu, Z., and Chen, H. (2015). First direct evidence of sedimentary carbonate recycling in subduction-related xenoliths. Scientific Reports, 5(1), 1-11.

Lockner, D. (1993). The role of acoustic emission in the study of rock fracture. In International Journal of Rock Mechanics and Mining Sciences and Geomechanics Abstracts (Vol. 30, No. 7, pp. 883-899). Pergamon.

Lockner, D., Byerlee, J. D., Kuksenko, V., Ponomarev, A., and Sidorin, A. (1991). Quasi-static fault growth and shear fracture energy in granite. Nature, 350(6313), 39-42.

Ma, D., Ma, Q., and Yuan, P. (2017). SHPB tests and dynamic constitutive model of artificial frozen sandy clay under confining pressure and temperature state. Cold Regions Science and Technology, 136, 37-43.

Ma, J., Wu, S., Zhang, X. P., and Gan, Y. (2020). Modeling acoustic emission in the Brazilian test using moment tensor inversion. Computers and Geotechnics, 123, 103567.

Manthei, G. (2005). Characterization of acoustic emission sources in a rock salt specimen under triaxial compression. Bulletin of the Seismological Society of America, 95(5), 1674-1700.

Mellor, M., and Hawkes, I. (1971). Measurement of tensile strength by diametral compression of discs and annuli. Engineering Geology, 5(3), 173-225.

Meng, F., Wong, L. N. Y., and Zhou, H. (2021). Rock brittleness indices and their applications to different fields of rock engineering: a review. Journal of Rock Mechanics and Geotechnical Engineering, 13(1), 221-247.

Meng, F., Zhou, H., Zhang, C., Xu, R., Lu, J. (2015). Evaluation methodology of brittleness of rock based on post-peak stress–strain curves. Rock Mechanics and Rock Engineering, 48(5), 1787-1805.

Meng, W. Z., and Wu, W. (2023) Machine learning aided prediction of the mechanical properties of frozen fractured rocks. Rock Mechanics and Rock Engineering, 56(1).

Mohammadi, S.D., Torabi-Kaveh, M., and Bayati, M. (2015). Prediction of TBM penetration rate using intact and mass rock properties (case study, Zagros long tunnel, Iran). Arabian Journal of Geosciences, 8 (6), 3893e3904.

Msekh, M. A., Sargado, J. M., Jamshidian, M., Areias, P. M., and Rabczuk, T. (2015). Abaqus implementation of phase-field model for brittle fracture. Computational Materials Science, 96, 472-484.

Musunuri, A., and Mitri, H. (2009). Laboratory investigation into rock fracturing with expansive cement. International Journal of Mining and Mineral Engineering, 1(4), 327-345.

Natanzi, A. S., and Laefer, D. F. (2014). Using chemicals as demolition agents near historic structures. In 9th International Conference on Structural Analysis of Historical Constructions, Mexico City, Mexico, 14-17.

Natanzi, A. S., Laefer, D. F., and Connolly, L. (2016). Cold and moderate ambient temperatures effects on expansive pressure development in soundless chemical demolition agents. Construction and Building Materials, 110, 117-127.

Ng, T. T. (2006). Input parameters of discrete element methods. Journal of Engineering Mechanics, 132(7), 723-729.

Nojima, T., and Ogawa, K. (1989). Impact strength of ceramics at high temperatures. Mechanical Properties of Materials at High Rates of Strain, 371-378.

Park, D., Jeon, B., and Jeon, S. (2009). A numerical study on the screening of blast-induced waves for reducing ground vibration. Rock Mechanics and Rock Engineering, 42(3), 449-473.

Patel, S., and Martin, C. D. (2020). Impact of the initial crack volume on the intact behavior of a bonded particle model. Computers and Geotechnics, 127, 103764.

Pei, P., Dai, F., Liu, Y., and Wei, M. (2020). Dynamic tensile behavior of rocks under static pre-tension using the flattened Brazilian disc method. International Journal of Rock Mechanics and Mining Sciences, 126, 104208.

Peng, J., Rong, G., Cai, M., Yao, M. D., and Zhou, C. B. (2016a). Physical and mechanical behaviors of a thermal-damaged coarse marble under uniaxial compression. Engineering Geology, 200, 88-93.

Peng, J., Rong, G., Cai, M., Yao, M., and Zhou, C. (2016b). Comparison of mechanical properties of undamaged and thermal-damaged coarse marbles under triaxial

compression. International Journal of Rock Mechanics and Mining Sciences, 100(83), 135-139.

Perez, S., Karakus, M., and Sepulveda, E. (2015). A preliminary study on the role of acoustic emission on inferring Cerchar abrasivity index of rocks using artificial neural network. Wear, 344, 1-8.

Plinninger, R., Käsling, H., Thuro, K., and Spaun, G. (2003). Testing conditions and geomechanical properties influencing the CERCHAR abrasiveness index (CAI) value. International Journal of Rock Mechanics and Mining Sciences, 40(2), 259-263.

Potyondy, D. O., and Cundall, P. A. (2004). A bonded-particle model for rock. International Journal of Rock Mechanics and Mining Sciences, 41(8), 1329-1364.

Qiu, H., Zhu, Z., Wang, M., Wang, F., Ma, Y., Lang, L., and Ying, P. (2020). Study on crack dynamic propagation behavior and fracture toughness in rock-mortar interface of concrete. Engineering Fracture Mechanics, 228, 106798.

Ramírez, H., and Rubio-Gonzalez, C. (2006). Finite-element simulation of wave propagation and dispersion in Hopkinson bar test. Materials & Design, 27(1), 36-44.

Rathnaweera, T. D., Ranjith, P. G., Gu, X., Perera, M. S. A., Kumari, W. G. P., Wanniarachchi, W. A. M., and Li, J. C. (2018). Experimental investigation of thermomechanical behaviour of clay-rich sandstone at extreme temperatures followed by cooling treatments. International Journal of Rock Mechanics and Mining Sciences, 107, 208-223.

Rickman, R., Mullen, M. J., Petre, J. E., Grieser, W. V., and Kundert, D. (2008). A practical use of shale petrophysics for stimulation design optimization: All shale plays are not clones of the Barnett Shale. In SPE annual technical conference and exhibition. OnePetro.

Ross, C. A., and Tedesco, J. W. (1989). Split-Hopkinson pressure-bar tests on concrete and mortar in tension and compression. Materials Journal, 86(5), 475-481.

Rossi, E., Kant, M. A., Madonna, C., Saar, M. O., and Rudolf von Rohr, P. (2018). The effects of high heating rate and high temperature on the rock strength: feasibility study of a thermally assisted drilling method. Rock Mechanics and Rock Engineering, 51(9), 2957-2964.

Rossi, E., Jamali, S., Wittig, V., Saar, M. O., and von Rohr, P. R. (2020a). A combined thermo-mechanical drilling technology for deep geothermal and hard rock reservoirs. Geothermics, 85, 101771.

Rossi, E., Saar, M. O., and Rudolf von Rohr, P. (2020b). The influence of thermal treatment on rock–bit interaction: a study of a combined thermo–mechanical drilling (CTMD) concept. Geothermal Energy, 8(1), 1-22.

Rostami, J., Ghasemi, A., Alavi Gharahbagh, E., Dogruoz, C., and Dahl, F. (2014). Study of dominant factors affecting Cerchar abrasivity index. Rock Mechanics and Rock Engineering, 47(5), 1905-1919.

Roylance, D. (2001). Introduction to Fracture Mechanics. Saylor org, Washington, D.C.

Rubino, V., Rosakis, A. J., and Lapusta, N. (2019). Full-field ultrahigh-speed quantification of dynamic shear ruptures using digital image correlation. Experimental Mechanics, 59(5), 551-582.

Sahinoglu, U.K., and Ozer, U. (2020). The prediction of cutter wear from temperature measurements on TBM discs and cutting face. Arabian Journal of Geosciences, 13(5), 1-11.

Saksala, T., and Ibrahimbegovic, A. (2020). Thermal shock weakening of granite rock under dynamic loading: 3D numerical modeling based on embedded discontinuity finite elements. International Journal for Numerical and Analytical Methods in Geomechanics, 44(13), 1788-1811.

Salimian, M. H., Baghbanan, A., Hashemolhosseini, H., Dehghanipoodeh, M., and Norouzi, S. (2017). Effect of grouting on shear behavior of rock joint. International Journal of Rock Mechanics and Mining Sciences, 98, 159-166.

Scholtès, L., and Donzé, F. V. (2013). A DEM model for soft and hard rocks: role of grain interlocking on strength. Journal of the Mechanics and Physics of Solids, 61(2), 352-369.

Schöpfer, M. P., Abe, S., Childs, C., and Walsh, J. J. (2009). The impact of porosity and crack density on the elasticity, strength and friction of cohesive granular materials: insights from DEM modelling. International Journal of Rock Mechanics and Mining Sciences, 46(2), 250-261.

Schöpfer, M. P., and Childs, C. (2013). The orientation and dilatancy of shear bands in a bonded particle model for rock. International Journal of Rock Mechanics and Mining Sciences, 57, 75-88.

Sha, S., Rong, G., Peng, J., Li, B., and Wu, Z. (2019). Effect of open-fire-induced damage on Brazilian tensile strength and microstructure of granite. Rock Mechanics and Rock Engineering, 52(11), 4189-4202.

Sha, S., Rong, G., Tan, J., He, R., and Li, B. (2020). Tensile strength and brittleness of sandstone and granite after high-temperature treatment: a review. Arabian Journal of Geosciences, 13(14).

Shao, S., Wasantha, P. L., Ranjith, P. G., and Chen, B. K. (2014). Effect of cooling rate on the mechanical behavior of heated Strathbogie granite with different grain sizes. International Journal of Rock Mechanics and Mining Sciences, 70, 381-387.

Shi, X., Wang, M., Wang, Z., Wang, Y., Lu, S., and Tian, W. (2021). A brittleness index evaluation method for weak-brittle rock by acoustic emission technique. Journal of Natural Gas Science and Engineering, 95, 104160.

Singh, S. P. (1986). Brittleness and the mechanical winning of coal. Mining Science and Technology, 3(3), 173-180.

Singh, S. P., and Xavier, P. (2005). Causes, impact and control of overbreak in underground excavations. Tunnelling and Underground Space Technology, 20(1), 63-71.

Stierle, E., Vavryčuk, V., Kwiatek, G., Charalampidou, E. M., and Bohnhoff, M. (2016). Seismic moment tensors of acoustic emissions recorded during laboratory rock deformation experiments: sensitivity to attenuation and anisotropy. Geophysical Supplements to the Monthly Notices of the Royal Astronomical Society, 205(1), 38-50.

Su, H., Jing, H., Du, M., and Wang, C. (2016). Experimental investigation on tensile strength and its loading rate effect of sandstone after high temperature treatment. Arabian Journal of Geosciences, 9(13), 1-11).

Sui, W., Liu, J., Hu, W., Qi, J., and Zhan, K. (2015). Experimental investigation on sealing efficiency of chemical grouting in rock fracture with flowing water. Tunnelling and Underground Space Technology, 50, 239-249.

Swanson, D. E., and Labuz, J. F. (1999). Behavior of a calcium oxide-based expansive cement. Concrete Science and Engineering, 1(3), 166-172.

Tang, C. (1997). Numerical simulation of progressive rock failure and associated seismicity. International Journal of Rock Mechanics and Mining Sciences, 34(2), 249-261.

Tang, S. B., Huang, R. Q., Wang, S. Y., Bao, C. Y., and Tang, C. A. (2017). Study of the fracture process in heterogeneous materials around boreholes filled with expansion cement. International Journal of Solids and Structures, 112, 1-15.

Tarasov, B. G, and Stacey, T. R. (2017). Features of the energy balance and fragmentation mechanisms at spontaneous failure of class I and class II rocks. Rock Mechanics and Rock Engineering, 50(10), 2563-2584

Tarasov, B., and Potvin, Y. (2013). Universal criteria for rock brittleness estimation under triaxial compression. International Journal of Rock Mechanics and Mining Sciences, 59, 57-69.

Tarasov, B., Potvin, Y. (2012). Absolute, relative and intrinsic rock brittleness at compression. Mining Technology, 121(4), 218-225.

Tekkaya, A.E., and Soyarslan, C. (2014). Finite Element Method. In: Laperrière, L., Reinhart, G. (eds) CIRP Encyclopedia of Production Engineering. Springer, Berlin, Heidelberg.

Thompson, B. D., Young, R. P., and Lockner, D. A. (2009). Premonitory acoustic emissions and stick-slip in natural and smooth-faulted Westerly granite. Journal of Geophysical Research: Solid Earth, 114(B2).

Tripathy, A., Singh, T. N., and Kundu, J. (2015). Prediction of abrasiveness index of some Indian rocks using soft computing methods. Measurement, 68, 302-309.

Ündül, Ö., and Er, S. (2017). Investigating the effects of micro-texture and geo-mechanical properties on the abrasiveness of volcanic rocks. Engineering Geology, 229, 85-94.

Uysal, O., Erarslan, K., Cebi, M. A., and Akcakoca, H. (2008). Effect of barrier holes on blast induced vibration. International Journal of Rock Mechanics and Mining Sciences, 45(5), 712-719.

Verleysen, P., Degrieck, J., Verstraete, T., and Van Slycken, J. (2008). Influence of specimen geometry on split Hopkinson tensile bar tests on sheet materials. Experimental Mechanics, 48(5), 587.

Walker, K. K., Schexnayder, C., Mayo, R. E., and Walsh, K. D. (1996). Methods and procedural considerations in demolishing tall concrete chimneys. Journal of Construction Engineering and Management, 122(3), 223-230.

Walton, G. (2021). A new perspective on the brittle–ductile transition of rocks. Rock Mechanics and Rock Engineering, 54(12), 5993-6006.

Wang, B., Chen, Y., and Wong, T. F. (2008). A discrete element model for the development of compaction localization in granular rock. Journal of Geophysical Research: Solid Earth, 113(B3).

Wang, C., Jiang, L., Bobet, A., and Pyrak-Nolte, L. J. (2020). Numerical simulation of rock fracture roughness due to mineral layering and texture. In AGU Fall Meeting

Abstracts (Vol. 2020, pp. NG010-03).

Wang, C., Jiang, L., Bobet, A., and Pyrak-Nolte, L. J. (2021). Modeling tensile fracture in layered rocks with oriented mineral texture. In 55th US Rock Mechanics/Geomechanics Symposium. OnePetro.

Wang, J., Fu, J., Song, W., and Zhang, Y. (2021). Mechanical properties, damage evolution, and constitutive model of rock-encased backfill under uniaxial compression. Construction and Building Materials, 285, 122898.

Wang, J. A., and Park, H. D. (2001). Comprehensive prediction of rockburst based on analysis of strain energy in rocks. Tunnelling and Underground Space Technology, 16(1), 49-57.

Wang, L., Wei, M., and Wu, W. (2022). Control of dynamic failure of brittle rock using expansive mortar. Acta Geotechnica, 1-11.

Wang, L., Wu, W. (2022) Modelling of dynamic tensile failure of inclusion-bearing rocks. Geomechanics and Geophysics for Geo-energy and Geo-resources, 8(5), 168.

Wang, Q. Z., and Xing, L. (1999). Determination of fracture toughness KIC by using the flattened Brazilian disk specimen for rocks. Engineering Fracture Mechanics, 64(2), 193-201.

Wang, Q. Z., Feng, F., Ni, M., and Gou, X. P. (2011). Measurement of mode I and mode II rock dynamic fracture toughness with cracked straight through flattened Brazilian disc impacted by split Hopkinson pressure bar. Engineering Fracture Mechanics, 78(12), 2455-2469.

Wang, Q. Z., Li, W., and Song, X. L. (2006). A method for testing dynamic tensile strength and elastic modulus of rock materials using SHPB. Pure and Applied Geophysics, 163(5), 1091-1100.

Wang, Q. Z., Li, W., and Xie, H. P. (2009). Dynamic split tensile test of Flattened Brazilian Disc of rock with SHPB setup. Mechanics of Materials, 41(3), 252-260.

Wang, S., Liu, Y., Zhou, J., Wu, Q., Ma, S., Zhou, Z. (2018). Dynamic compressive characteristics of sandstone under confining pressure and radial gradient stress with the SHPB test. Advances in Civil Engineering,1387390.

Wang, W., Wang, Y., Chai, B., Du, J., Xing, L., and Xia, Z. (2022). An energy-based method to determine rock brittleness by considering rock damage. Rock Mechanics and Rock Engineering, 55(3), 1585-1597.

Wang, Y., and Jiang, Z. (2012). Dynamic compressive behavior of selected aluminum alloy at low temperature. Materials Science and Engineering: A, 553, 176-180.

Wang, Y., and Tonon, F. (2009). Modeling Lac du Bonnet granite using a discrete element model. International Journal of Rock Mechanics and Mining Sciences, 46(7), 1124-1135.

Wanniarachchi, W. A. M., and Wu, W. (2021) Permeability evolution of rock-concrete interfaces in underground lined storage systems. International Journal of Rock Mechanics and Mining Sciences, 143, 104792.

Wasantha, P. L. P., Guerrieri, M., and Xu, T. (2021). Effects of tunnel fires on the mechanical behaviour of rocks in the vicinity–a review. Tunnelling and Underground Space Technology, 108, 103667.

Wasantha, P. L., and Ranjith, P. G. (2014). Water-weakening behavior of Hawkesbury sandstone in brittle regime. Engineering Geology, 178, 91-101.

Wawersik, W. R., and Fairhurst, C. H. (1970). A study of brittle rock fracture in laboratory compression experiments. International Journal of Rock Mechanics and Mining Sciences (Vol. 7, No. 5, pp. 561-575). Pergamon.

Wei, M. D., Dai, F., Xu, N. W., and Zhao, T. (2016). Stress intensity factors and fracture process zones of ISRM-suggested chevron notched specimens for mode I fracture toughness testing of rocks. Engineering Fracture Mechanics, 168, 174-189.

West G (1989) Rock abrasiveness testing for tunnelling. International Journal of Rock Mechanics and Mining Sciences, 26:151–160.

Wong, L. N. Y., Li, Z., Kang, H. M., and Teh, C. I. (2017). Dynamic loading of Carrara marble in a heated state. Rock Mechanics and Rock Engineering, 50(6), 1487-1505.

Wu, C., Hao, H., and Zhou, Y. (2000). Statistical properties of the Bukit Timah granite in Singapore. Journal of Testing and Evaluation, 28(1), 36-43.

Wu, Q., Li, X., Weng, L., Li, Q., Zhu, Y., and Luo, R. (2019a). Experimental investigation of the dynamic response of prestressed rockbolt by using an SHPB-based rockbolt test system. Tunnelling and Underground Space Technology, 93, 103088.

Wu, Q., Weng, L., Zhao, Y., Guo, B., and Luo, T. (2019b). On the tensile mechanical characteristics of fine-grained granite after heating/cooling treatments with different cooling rates. Engineering Geology, 253, 94-110.

Wu, W. (2021) A review of unloading-induced fault instability. Underground Space, 6(5), 528-538.

Wu, W., and Zhao, J. (2015). Effect of water content on P-wave attenuation across a rock fracture filled with granular materials. Rock Mechanics and Rock Engineering, 48(2), 867-871.

Wu, W., Li, H., and Zhao, J. (2015). Dynamic responses of non-welded and welded rock fractures and implications for P-wave attenuation in a rock mass. International Journal of Rock Mechanics and Mining Sciences, 77, 174-181.

Wu, W., Li, J. C., and Zhao, J. (2013). Seismic response of adjacent filled parallel rock fractures with dissimilar properties. Journal of Applied Geophysics, 96, 33-37.

Wu, Z., Ji, X., Liu, Q., and Fan, L. (2020). Study of microstructure effect on the nonlinear mechanical behavior and failure process of rock using an image-based-FDEM model. Computers and Geotechnics, 121, 103480.

Wu, W., Zhao, Z. H., and Duan, K. (2017) Unloading-induced instability of granular fault gouges and implications for excavation-induced seismicity. Tunneling and Underground Space Technology, 63, 154-161.

Xia, K., and Yao, W. (2015). Dynamic rock tests using split Hopkinson (Kolsky) bar system–a review. Journal of Rock Mechanics and Geotechnical Engineering, 7(1), 27-59.

Xia, K., Nasseri, M. H. B., Mohanty, B., Lu, F., Chen, R., and Luo, S. N. (2008). Effects of microstructures on dynamic compression of Barre granite. International Journal of Rock Mechanics and Mining Sciences, 45(6), 879-887.

Xia, X., Li, H., Niu, J., Li, J., and Liu, Y. (2014). Experimental study on amplitude change of blast vibrations through steps and ditches. International Journal of Rock Mechanics and Mining Sciences, 71, 77-82.

Xie, H., Li, L., Peng, R., and Ju, Y. (2009). Energy analysis and criteria for structural failure of rocks. Journal of Rock Mechanics and Geotechnical Engineering, 1(1), 11-20.

Xu, J., Zhai, C., Qin, L., and Yu, G. (2017). Evaluation research of the fracturing capacity of non-explosive expansion material applied to coal-seam roof rock. International Journal of Rock Mechanics and Mining Sciences, 94, 103-111.

Xu, Y., and Cai, M. (2017). Numerical study on the influence of cross-sectional shape on strength and deformation behaviors of rocks under uniaxial compression. Computers and Geotechnics, 84, 129-137.

Xu, Y., and Dai, F. (2018). Dynamic response and failure mechanism of brittle rocks under combined compression-shear loading experiments. Rock Mechanics and Rock Engineering, 51(3), 747-764.

Yan, C., and Jiao, Y. Y. (2020). A 2D discrete heat transfer model considering the thermal resistance effect of fractures for simulating the thermal cracking of brittle materials. Acta Geotechnica, 15(5), 1303-1319.

Yan, Z., Dai, F., Liu, Y., and Du, H. (2020). Experimental investigations of the dynamic mechanical properties and fracturing behavior of cracked rocks under dynamic loading. Bulletin of Engineering Geology and the Environment, 79(10), 5535-5552.

Yang, H., Duan, H. F., and Zhu, J. B. (2019). Ultrasonic P-wave propagation through water-filled rock joint: an experimental investigation. Journal of Applied Geophysics, 169, 1-14.

Yang, S. Q., Ranjith, P. G., Jing, H. W., Tian, W. L., and Ju, Y. (2017). An experimental investigation on thermal damage and failure mechanical behavior of granite after exposure to different high temperature treatments. Geothermics, 65, 180-197.

Yao, W., Xu, Y., Wang, W., and Kanopolous, P. (2016). Dependence of dynamic tensile strength of longyou sandstone on heat-treatment temperature and loading rate. Rock Mechanics and Rock Engineering, 49(10), 3899-3915.

Yaralı, O., Yaşar, E., Bacak, G., and Ranjith, P. G. (2008). A study of rock abrasivity and tool wear in coal measures rocks. International Journal of Coal Geology, 74(1), 53-66.

Yin, T., Zhang, S., Li, X., and Bai, L. (2018). A numerical estimate method of dynamic fracture initiation toughness of rock under high temperature. Engineering Fracture Mechanics, 204, 87-102.

Young, R. P., Hazzard, J. F., and Pettitt, W. S. (2000). Seismic and micromechanical studies of rock fracture. Geophysical Research Letters, 27(12), 1767-1770.

Yu, Q., Zhu, W., Ranjith, P. G., and Shao, S. (2018). Numerical simulation and interpretation of the grain size effect on rock strength. Geomechanics and Geophysics for Geo-Energy and Geo-Resources, 4(2), 157-173.

Zhai, C., Xu, J., Liu, S., and Qin, L. (2018). Fracturing mechanism of coal-like rock specimens under the effect of non-explosive expansion. International Journal of Rock Mechanics and Mining Sciences, 103, 145-154.

Zhang, C., Jin, Z., Feng, G., Song, X., and Rui, G. (2020). Double peaked stress–strain behavior and progressive failure mechanism of encased coal pillars under uniaxial compression. Rock Mechanics and Rock Engineering, 53(7), 3253-3266.

Zhang, D., Ranjith, P. G., and Perera, M. S. A. (2016). The brittleness indices used in rock mechanics and their application in shale hydraulic fracturing: a review. Journal of Petroleum Science and Engineering, 143, 158-170.

Zhang, F., Zhao, J., Hu, D., Skoczylas, F., & Shao, J. (2018). Laboratory investigation on physical and mechanical properties of granite after heating and water-cooling treatment. Rock Mechanics and Rock Engineering, 51(3), 677-694.

Zhang, G., and Konietzky, H. (2020). Cerchar Abrasion Ratio (CAR) as a new indicator for assessing rock abrasivity, rock–stylus interaction and cutting efficiency. Rock Mechanics and Rock Engineering, 53(7), 3363-3371.

Zhang, G., Konietzky, H., and Frühwirt, T. (2020a). Investigation of scratching specific energy in the Cerchar abrasivity test and its application for evaluating rock-tool interaction and efficiency of rock cutting. Wear, 448, 203218.

Zhang, G., Konietzky, H., Song, Z., and Zhang, M. (2020b). Study of Cerchar abrasive parameters and their relations to intrinsic properties of rocks for construction. Construction and Building Materials, 244, 118327.

Zhang, Q. B., and Zhao, J. (2013). Determination of mechanical properties and full-field strain measurements of rock material under dynamic loads. International Journal of Rock Mechanics and Mining Sciences, 60, 423-439.

Zhang, Q. B., and Zhao, J. (2014). A review of dynamic experimental techniques and mechanical behaviour of rock materials. Rock mechanics and rock engineering, 47(4), 1411-1478.

Zhang, S., Wu, S., Zhang, G., Guo, P., and Chu, C. (2020). Three-dimensional evolution of damage in sandstone Brazilian discs by the concurrent use of active and passive ultrasonic techniques. Acta Geotechnica, 15(2), 393-408.

Zhang, W., Sun, Q., Hao, S., Geng, J., and Lv, C. (2016). Experimental study on the variation of physical and mechanical properties of rock after high temperature treatment. Applied Thermal Engineering, 98, 1297-1304.

Zhang, Z. X. (2002). An empirical relation between mode I fracture toughness and the tensile strength of rock. International Journal of Rock Mechanics and Mining Sciences, 39(3), 401-406.

Zhao, H., and Gary, G. (1996). On the use of SHPB techniques to determine the dynamic behavior of materials in the range of small strains. International Journal of Solids and structures, 33(23), 3363-3375.

Zhao, G. F., Yin, Q., Russell, A. R., Li, Y., Wu, W., and Li, Q. (2019). On the linear elastic responses of the 2D bonded discrete element model. International Journal for Numerical and Analytical Methods in Geomechanics, 43(1), 166-182.

Zhao, Z. (2015). Thermal influence on mechanical properties of granite: a microcracking perspective. Rock Mechanics and Rock Engineering, 49(3), 747-762.

Zhao. Z., Guo, T. C., Li, S. J., Wu, W., Yang, Q., Chen, S. C. (2020) Effects of joint surface roughness and orientational anisotropy on characteristics of excavation damage zone in jointed rocks. International Journal of Rock Mechanics and Mining Sciences, 128, 104265.

Zhao, Z., Liu, Z., Pu, H., and Li, X. (2018). Effect of thermal treatment on Brazilian tensile strength of granites with different grain size distributions. Rock Mechanics and Rock Engineering, 51(4), 1293-1303.

Zhao, Z. Y., Gong, Q.M., Zhang, Y., and Zhao, J. (2007). Prediction model of tunnel boring machine performance by ensemble neural networks. Geomechanics & Geoengineering, 2 (2), 123e128.

Zhou, S., Zhuang, X., Zhou, J., and Liu, F. (2021). Phase field characterization of rock fractures in Brazilian splitting test specimens containing voids and inclusions. International Journal of Geomechanics, 21(3), 04021006.

Zhou, Y. X., Xia, K. W., Li, X. B., Li, H. B., Ma, G. W., Zhao, J., and Dai, F. (2011). Suggested methods for determining the dynamic strength parameters and mode-I fracture toughness of rock materials. In The ISRM Suggested Methods for Rock Characterization, Testing and Monitoring: 2007-2014 (pp. 35-44). Springer.

Zhou, Z., Li, X., Zou, Y., Jiang, Y., and Li, G. (2014). Dynamic Brazilian tests of granite under coupled static and dynamic loads. Rock Mechanics and Rock Engineering, 47(2), 495-505.

Zhou, Z., Lu, J., and Cai, X. (2020). Static and dynamic tensile behavior of rock-concrete bi-material disc with different interface inclinations. Construction and Building Materials, 256, 119424.

Zhou, Z., Zhou, J., Zhao, Y., Chen, L., and Li, C. (2021). Microscopic failure mechanism analysis of rock under dynamic Brazilian test based on acoustic emission and moment tensor simulation. Frontiers in Physics, 8, 592483.

Zou, C., Cheng, Y., and Li, J. (2021). Strain rate and size effects on the brittleness indexes of Carrara marble. International Journal of Rock Mechanics and Mining Sciences, 146, 104860.

Zuo, J., Xie, H., Zhou, H., and Peng, S. (2010). SEM in situ investigation on thermal cracking behavior of Pingdingshan sandstone at elevated temperature. Geophysical Journal International, 181(2), 593-603.